A COMPUTATIONAL FLUID DYNAMICS MODIFIED FRICTION FACTOR AND LEAKAGE MODEL FOR AN IMPROVED BULK-FLOW ANALYSIS OF LABYRINTH GAS SEALS

A Dissertation

by

TINGCHENG WU

Submitted to the Office of Graduate and Professional Studies of
Texas A&M University
in partial fulfillment of the requirements for the degree of

DOCTOR OF PHILOSOPHY

Chair of Committee, Luis San Andrés
Committee Members, Adolfo Delgado
Stefan Hurlebaus
Michael B. Pate
Head of Department, Andreas A. Polycarpou

December 2019

Major Subject: Mechanical Engineering

ABSTRACT

Bulk-flow predictive models (BFM), though simple and fast, often fail to accurately predict the performance of gas labyrinth seals (LSs). In this work, a Computational Fluid Dynamics (CFD) analysis quantifies the effects of LS tip clearance (C_r) and operating conditions on the circumferential direction friction factors (f_r, f_s) at the rotor and stator surfaces, as well as on the kinetic energy carry-over coefficient (μ_{1i}) for mass flow prediction. A fourteen teeth on stator LS seal (L/D=0.29) with clearance C_r=1/733 D is selected for analysis.

The analysis models the seal with a fine mesh of a few million nodes and a commercial CFD code calculates the flow field for the nominal operating conditions, includes wide changes in clearance, 80% to 200% of the nominal C_r, shaft speed from 5 krpm to 15 krpm (58 m/s ~173 m/s), inlet pre-swirl velocity varying from 0% to 72% of rotor surface speed, a gas supply pressure ranging from 60 bar to 100 bar, and along with various discharge pressures producing a pressure ratio ($PR = P_{out}/P_{in}$) ranging from 0.40 to 0.85. The rotor surface friction factor $f_{r\theta}$ is independent of the changes in clearance (C_r) or the inlet circumferential velocity pre-swirl ratio; whereas an increase in rotor speed or in pressure ratio (PR) decreases $f_{r\theta}$. On the other hand, an increase in rotor speed, pressure ratio and inlet preswirl ratio decreases $f_{s\theta}$, the stator friction factor. Besides, $f_{s\theta}$ increases with an increase in radial clearance. Further, $f_{r\theta}$ and $f_{s\theta}$ are only sensitive to the pressure ratio, but not to the magnitude of either the supply pressure or discharge pressure.

The kinetic energy carry-over coefficient (μ_{1i}) increases with respect to the seal radial clearance (C_r); whereas μ_{1i} shows a parabolic correlation with the pressure ratio *PR*. μ_{1i} is only sensitive to *PR*, and not to the magnitude of either the supply pressure or the discharge pressure.

Furthermore, based on the CFD derived results, this work presents a modified friction factor model, $f = n\,\mathrm{Re}^m$ (where Re is the flow Reynolds number)[1], as well as a modified kinetic energy carry-over coefficient model, both quantifying the effect of seal geometry and operating conditions. An independent case analysis serves to validate the model; and the modified BFM does improve the prediction of the direct stiffness (maximum discrepancy decreases from 320% to 70%), direct damping (discrepancy decreases from 90% to 50%), and mass flow rate (discrepancy decreases from 14% to 2%).The above coefficients and flow agree well with both CFD and experimental results.

(**Note**: this dissertation is organized based on the author's previous publications and reports during his PhD study; and the format follows American Society of Mechanical Engineers (ASME) journal publications format)

[1] n = 0.079, m = -0.25 for the classical Blasius friction factor model, strictly valid for smooth surface pipelines.

DEDICATION

To my family and friends; without their support I will not be able to make it.

ACKNOWLEDGEMENTS

I would like to thank my committee chair, Dr. Luis San Andrés, for his guidance and support. He is not only my academic advisor but also my life mentor. From Dr. San Andrés, I learned the attitude of diligence and hard work towards one's professional career that I will carry throughout my career.

Thanks to my committee members, Dr. Adolfo Delgado, Dr. Stefan Hurlebaus, and Dr. Michael B. Pate, for their guidance and support throughout the course of this research.

Thanks also go to my friends and colleagues and the department faculty and staff for making my time at Texas A&M University a great experience. Particularly, my lab mates at the Turbomachinery Laboratory, Xueliang Lu, Jing Yang, Bonjing Koo, Yong Zheng, Wonbae Jung, Rasool Koosha, Scott Tran, Jonathan Toner, Rachel Bolen, Jose Barajas, and many more.

Special thanks to Turbomachinery Research Consortium (TRC) for their interest and financial support throughout the years.

Finally, thanks to my parents, my parents in law and my sisters for their encouragement and to my wife for her patience and love.

TABLE OF CONTENTS

Page

LIST OF FIGURES

Page

LIST OF TABLES

Page

I. INTRODUCTION [2]

Multistage centrifugal pumps and compressors are among the most widely used pieces of rotating machinery in the industry. A typical application requires the arrangement of several impellers mounted on a shaft that spins within a stationary case. Labyrinth seals (LS), commonly found in gas and steam turbines and compressors, control the leakage (secondary flow) from high-pressure regions to low-pressure regions. As in Figure 1, a typical LS comprises of cavities and teeth. A see-through LS has all teeth either on the rotor (TOR) or on the stator (TOS). Excessive leakage (secondary flow) represents a substantial loss in gas processing efficiency and also drag power consumption. An interlocking labyrinth seal (ILS), with teeth both on the rotor and the stator, substantially reduces leakage up to 30% when compared to conventional TOR or TOS labyrinth seals [1-3]. Seal leakage depends on a variety of geometrical parameters (i.e., tooth shape, number of cavities), temperature, shaft speed and pressure (inlet and outlet). Current BFM applies Neumann's leakage equation to estimate the mass flow rate of a labyrinth seal. However, this equation does not consider the effect of tooth thickness, which plays a significant role in reducing the leakage according to Gamal and Vance [4] test results.

During operation, labyrinth seals not just restrict a secondary flow but also produce a reaction force acting on the rotor which could induce a rotordynamic instability. The reaction force components F_{rad} and F_{tan} are expressed as $F_{rad}/e = -(K + c\omega)$ and $F_{tan}/e = (k - C\omega)$ where e is the rotor whirl orbit, and ω is the whirl frequency. K, C and k, c are the direct and cross-coupled stiffness and damping coefficients, respectively. The ability to accurately predict LS leakage and

[2] This part has been reproduced from "Gas Labyrinth Seals: on the Effect of Clearance and Operating Conditions on Wall Friction Factors – a CFD Investigation" by Wu, T., and San Andrés, L., 2019, Tribol. Int, 131, pp. 363-376.

rotordynamic force coefficients is crucial for the stable and efficient operation of turbomachinery.

Labyrinth gas seals have negligible added mass terms and are typically modeled by a linear reaction force vs. seal displacement model that is valid for small motions about a centered position [5]. To estimate the dynamic force coefficients, traditional analyses use the bulk-flow model (BFM), initially developed by Hirs [6]. BFMs are still in use in day-to-day rotordynamic stability analyses. The BFM uses film averaged fluid pressure and flow velocities, while the wall shear stresses are based on friction factors. The BFM utilizes empirical friction factors from Moody's friction factor model or Blasius friction model [7]. The Blasius friction factor model ($f = n\mathrm{Re}^m$) is a function of the flow Reynolds number ($R_e = 2(\rho/\mu)C_rU$) with two empirical coefficients. Yamada's (1962) [8] test data for flow in a smooth surface annulus with a rotating inner cylinder yields the two empirical coefficients $n = 0.079$, and $m = -0.25$. The Blasius friction model predicts a friction factor that shows moderate accuracy against the test results for smooth surface annular seals [5].

However, flat plate test results by Ha and Childs [9] and tests with a honeycomb annular gas seal by Al-Qutub et al. [10] show that the friction factor increases with an increase in seal clearance. Their findings are in opposition to Blasius's friction factor model. Note $f = nR_e^m$, decreases with an increase in clearance C_r, as the Reynolds number R_e is proportional to C_r, and $f \sim 1/Re^{0.25}$.

Thus, a better assessing of the friction factor model, as well as the leakage model in a LS, are of great significance to improve BFM predictions.

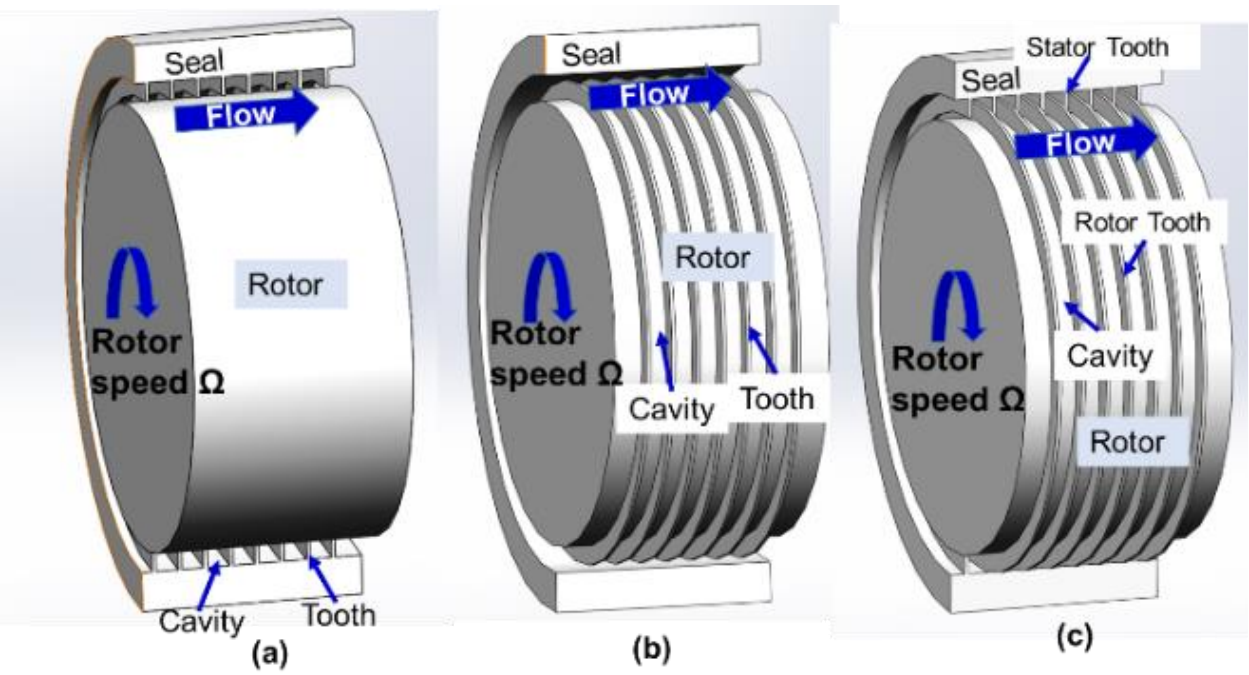

Figure 1. Schematic views of labyrinth seals: (a) tooth on the stator (TOS), (b) tooth on the rotor (TOR), and (c) interlocking labyrinth seal (ILS).

II. LITERATURE REVIEW[3]

This review first assesses experimental works on labyrinth seals and next discusses the various numerical analyses models for labyrinth seals.

2.1 Experimental Studies on Labyrinth Seals

In 1978, Benckert and Wachter [11] measure the stiffness of labyrinth seals (TOS, ILS, and stepped LS) and investigate the influence of rotor speed and circumferential pre-swirl velocity on seal reaction forces. Their results show that the reaction forces are sensitive to the inlet flow pre-swirl, whereas the influence of rotor speed is minor for a seal with small number of teeth (less than 5). "Swirl webs," a first instance of swirl brakes, could sufficiently reduce the inlet pre-swirl velocity, and accordingly the seal destabilizing forces. Test rotordynamic force coefficients remain approximately constant and are independent of rotor eccentricity to 50% of the seal clearance. The test results support the "eccentricity independent" model discussed in Ref. [5]. Benckert and Wachter find no appreciable difference in the cross-coupled stiffness of an ILS and a TOS LS. Measured stiffness coefficients for a comparatively long ($L/D \rightarrow 1$) LS are negative. Later in 1984, Leong and Brown [12] (1984) report similar results, i.e., most TOR and TOS LSs show a negative direct stiffness; though noting an exception for a short LS ($L/D = 0.1$) with only five cavities.

In 1986, Childs and Scharrer [13] test TOR & TOS labyrinth seals and report their rotordynamic force coefficients. The authors present direct damping coefficients for the first time. The test results show the stiffness and damping coefficients are sensitive to the inlet tangential (swirl) velocity and increase with an increase in inlet pressure. Later, Thieleke and Stetter (1990)

[3] This part has been partially reproduced from "Gas Labyrinth Seals: on the Effect of Clearance and Operating Conditions on Wall Friction Factors – a CFD Investigation" by Wu, T., and San Andrés, L., 2019, Tribol. Int, 131, pp. 363-376.

[14] point out that the cross-coupled force, arising within each cavity, depends on the change of circumferential velocity from one cavity to the next.

In 1988, Childs et al. [2] measure the leakage and force coefficients for an ILS (C_r = 0.25 mm, average tooth pitch is 5 mm, L/D = 0.34) and a TOS LS (C_r = 0.305 mm, tooth pitch is 4 mm, L/D = 0.30). The authors test the seals at a rotor speed up to 16,000 rpm (½$D\Omega$ = 126 m/s) while the supply pressure ranges from 3.0 bar to 8.0 bar ($PR = P_{in}/P_{out}$ = 3.0-8.0). The test results evidence the ILS leaks substantially less (up to 60%) than the conventional TOS LS. Childs et al. note the ILS has frequency dependent rotordynamic force coefficients, which in the 1980s posed a conflict with the generally-held view that force coefficients provide a frequency-independent relation between reaction forces and rotor displacements. Compared to see-through (TOR and TOS) Ls designs, the ILS usually has a lower and negative cross-coupled stiffness (k). However, a see-through LS shows approximately twice the direct damping coefficient than the corresponding coefficient in an ILS. The direct stiffness coefficient (K) for both configurations is negative; the see-through configuration shows half the magnitude of the direct stiffness for the ILS.

In 1999, Baumann [10] reports a thorough investigation on the effect of labyrinth seals on the stability of high-pressure centrifugal compressors. The units equip with TOS LSs and groove-comb LSs, similar to an ILS or a stepped LS. The author finds that the shop test identified direct stiffness and logarithmic decrement (δ), a measure of viscous damping ($\xi \simeq \delta/2\pi$), for both seal types decrease as the compressor discharge pressure increases. Hence the choice of labyrinth seal affects the compressor system amplification factor and the placement of its critical speed.

In 2007, Paolillo et al. [15] demonstrate the impact of rotor speed on labyrinth seal leakage. The ratio between rotor speed ($U_{rotor} = R\Omega$) and axial flow velocity (W), U_{rotor}/W, plays an important role. When $U_{rotor}/W < 1$, rotor speed has a negligible effect on seal leakage. Li et al. [16]

(2011) later confirm this finding through both experimental and numerical analyses. On the other hand, for $U_{rotor}/W > 1$, the seal leakage could significantly decrease. For large velocity ratios $U_{rotor}/W > 5$, the seal leakage decreases more than 20% respect to that at a low velocity ratio conditions [15].

Besides rotor speed, as shown in 2008 by Gamal and Vance [4], the impact of labyrinth seal teeth thickness on seal leakage is also of interest. The authors report that doubling the teeth thickness reduces seal leakage by 10% - 20% for the test seals at all considered supply pressures (P_{in} ranges from 2 bar to 6.9 bar). As the fluid jet leaves the constriction (seal tooth), it expands into the subsequent downstream cavity. Both the clearance and the thickness of the tooth affect the angle of expansion, and therefore the amount of carried over kinetic energy [17]. Therefore, increasing the teeth thickness reduces seal leakage. Also, a thicker bladed seal may increase the frictional loss in the restriction. Test results also evidence that a reduction in cavity depth by up to 80% (the cavity depth ranges from 2.5 mm to 12.7 mm) has virtually no impact on seal leakage. The experimental and numerical analysis results from Li et al. [18] also confirm this finding.

Recall that the frequency dependent characteristic of rotordynamic force coefficients reported by Childs et al. [2] in 1988. Recent test results [19-22] evidence that LSs possess frequency dependent rotordynamic force coefficients; in particular, the direct stiffness coefficient. The test cross-coupled stiffness is only sensitive to the inlet pre-swirl velocity and not rotor speed. Thus, an inlet pre-swirl rather than rotor speed has a stronger influence on the seal effective damping ratio.

2.2 Analyses for Labyrinth Seals

Besides the experimental investigations, theoretical analyses for labyrinth seals are well documented since the early 1900s. In the past, researchers have produced analyses predicting the leakage and rotordynamic force coefficients of labyrinth seals. Notable to this day are the bulk-flow models (BFM) advanced by Vance and Murphy (1980) [23], Kostyuk (1972) [24], Iwatsubo et al. (1980, 1982) [25, 26], and Childs and Scharrer (1986) [27].

A BFM uses film averaged fluid pressure and flow velocities, while the wall shear stress is based on friction factors. Therefore, the BFM predictions strongly depend on the empirical coefficients, i.e., the flow discharge coefficient and the friction factor coefficients. Prior researchers have advanced several friction factor and leakage models to estimate labyrinth seal performance.

In 1908, Martin [28] considers the labyrinth to be a series of discrete throttling processes akin to the flow through a series of orifices. He derives a formula for the leakage flow through a labyrinth seal based on this model using a number of simplifying assumptions.

Later in 1935, Egli [29] examines the effect of changing the number of sharp-edged flow restrictors (teeth) and recommended that Martin's formula be used only when there are four or more throttling restrictors in series. For fewer restrictions, he used the Saint Venant-Wantzel orifice equation for each flow restriction. Egli offers test results for staggered labyrinths which show that the flow coefficient depends on the clearance and thickness of the restrictor. Later, based on Egli's [29] work, Hodkinson [17] (1939) modifies the leakage equation with a semi-empirical expression for the kinetic energy carry-over coefficient.

In 1964, Neumann [30] develops an empirical leakage formula applicable to gases and in contrast to liquids as typical orifice equations does. The formula includes a semi-empirical flow

coefficient and a kinetic energy carry-over coefficient. The semi-empirical flow coefficient, accounting for the further contraction of flow after it has passed through the plane of the restrictors (teeth), is a function of the pressure ratio between the upstream and downstream cavities. The kinetic energy carry-over coefficient is determined based on the seal geometry (tooth number, radial clearance, and the seal length). In labyrinth gas seal BFM predictions, solving the Neumann's leakage equation with an iterative technique gives the leakage through a seal as well as the intermediate seal cavity pressure.

In the bulk-flow model, fluid flow wall shear stresses, an energy dissipation mechanism, are determined in terms of wall friction factors. Therefore, the friction factor plays a prominent role in the rotordynamic force coefficients predictions. Hirs [6] first proposes adopting a Blasius-type pipe friction model ($f = n\mathrm{Re}^m$) in the BFM to evaluate wall friction factors, and from which to calculate the wall surface shear stresses. For smooth surface annular seals, the Blasius friction factor model (n = 0.079, m = -0.25) shows a moderate accuracy against test results [8].

However, for seals with textured surfaces, the Blasius friction model ($f = n\mathrm{Re}^m$) could not accurately estimate textured wall friction factors. Several experiments [10, 31, 32] have gathered seals performance and leakage information indicating that the friction factor increases with an increase in seal clearance, thus contradicting the theoretical predictions based on Moody or Blasius friction factor models. In 2000, Al-Qutub et al. [10] develop a new friction factor model for a honeycomb surface as derived from a static seal tester. The friction factor is found to be a function of Reynolds number and seal clearance only. The seal clearance plays a dominant role in this new friction factor model.

Later, through a CFD approach for liquid annular seals with deliberately macro textured surfaces, Villasmil (2002, 2006) [31, 32] finds that within a specific Reynolds number range, the

maximum friction factor observed in a specific textured pattern size is independent of the actual clearance, which appears to be related to the cavity length to clearance ratio and the physical cavity size itself. The CFD simulations indicate that textured surface area and its aspect ratios are the parameters defining the friction factor at a given seal clearance. Among those parameters, the surface textured area ratio is the primary parameter defining the flow resistance; a larger surface-textured area ratio leads to more substantial flow resistance (friction factors). The aspect ratio of the textured pattern plays a moderate role once the above-cited ratios are defined. Shallow patterns provide larger friction factors over the deep pattern designs. Besides, the size of the textured pattern relative to the actual clearance also affects the flow resistance.

To evaluate the impact of friction factor on the BFM predictions, D'Souza and Childs [33] (2002) predict the rotordynamic force coefficients of honeycomb gas seals with three variations of the Blasius pipe-friction model: (i) a basic model where the Reynolds number is a linear function of the local clearance, $f_s = n_s Re^{m_s}$ (ii) a model where the coefficient is a function of the local clearance, and (iii) a model where the coefficient and exponent are functions of the local clearance. Their comparisons show that the friction factor model choice is vital in the effective damping coefficient predictions, in particular, at a lower frequency range (60-70 Hz) where industrial centrifugal compressors and steam turbines may become unstable [33]. At higher frequencies, predicted stiffness and damping coefficients tend to deliver identical results for all of the friction models.

Unlike bulk-flow techniques, 3D CFD analysis makes no assumptions on the seal geometry, thus allowing (with a few million nodes) the analysis of fluid flow in an arbitrarily shaped domain, including stepped LSs and ILSs. As commercial software is readily accessible and computers processing speed continuously increase, computational fluid dynamics (CFD) analysis based

approaches to solving the Navier-Stokes equations of turbulent flow in seals is (becoming) standard engineering practice.

Once a flow solution is found, integration of the CFD predicted pressure field yields the reaction force acting on the rotor/stator surfaces, therefore leading to the estimation of the rotordynamic force coefficients. Moore [34] reports CFD derived LS predictions showing good correlation with experimental data for both rotordynamic force coefficients and leakage. The authors claim a (marginal) improvement over BFM predictions.

To obtain a seal reaction force, the following experimental methods are common practice: (1) "Pressure" method: assume the axial pressure fluctuations in the cavities are negligible and obtain the force by integrating the measured pressure on the stator (only a few points are needed); (2) "Stator Force" method: utilize a hydraulic shaker to excite the stator and directly measure the force on the stator wall; and (3) "Rotor Force" method: measure the force on the rotor using magnetic bearings (Kwanka [35] and Wagner [36]).

To quantify the influence of the above test methods on the results, Schettel et al. (2005) [37] calculate the rotordynamic force coefficients from CFD predicted flow fields in the way prescribed by each method. The authors present a comparison between experimentally obtained and CFD predicted stiffness coefficients for a comb-grooved labyrinth seal. The test results serve to validate a CFD predicted pressure field. The "Pressure" and "Stator Force" methods do not account for the influence of the up/downstream flow sections, whereas the CFD results show these areas generate a considerable part of the radial force [37]. On the other hand, the "Rotor Force" method integrates all the pressure field over the whole rotor surface including the up/downstream flow sections. The estimated rotordynamic force coefficients indicate that the stiffness coefficients (K, k) strongly depends on the method used. Compared to the other two methods, the "Rotor Force" method

predicts a significantly lower *K* and higher *k.* Therefore, the impact of the up/downstream flow sections on the rotordynamic force coefficients should also be a concern when designing a new machine [37].

The improvements in the efficiency and power output of turbomachines require optimizations of gas seals. Labyrinth seals, with their simple structure and reliable performance, are preferred. Except for tighter seal clearances, seal configurations are evolving continuously to reduce leakage, e.g., from a see-through design to a stepped labyrinth configurations. Utilizing CFD simulations, Kim et al. [38, 39] analyze the influence of labyrinth seal configurations on leakage behavior in terms the flow function ($\phi = \dot{m}\sqrt{T_{in}}/(A_c P_{in})$, where $\dot{m}$ is the mass flow rate, A_c is the cross section area, T_{in} and P_{in} are the inlet total temperature and pressure, respectively). The see-through labyrinth seal flow function increases with respect to the pressure ratio as well as the radial clearance. However, for a stepped labyrinth seal, an increase in radial clearance yields a more significant flow resistance (pressure loss) for an equivalent flow function [39]. That is, the flow function decreases with an increase in radial clearance. CFD simulations of a stepped labyrinth seal show the leakage is different when flow direction reverses. For a divergent flow arrangement (see Figure 2 (a)), the jet flow out of a clearance hits the next tooth wall more strongly as the clearance increases. On the other hand, for a convergent flow arrangement (see Figure 2 (b)), a larger clearance provides a more abrupt turning of the flow from a tooth tip to the next. Both the above flow fields change lead to a more substantial pressure drop across the tooth tips. Therefore, for a stepped labyrinth seal, the flow function decreases when an increase in seal clearance. A later study by Kang et al. (2010)[40] show that except for the seal teeth configuration, the stepped labyrinth seal leakage considerably depends on the land (rotor) surface structure. For a honeycomb

land surface, the flow function decreases with an increase of the clearance to honeycomb width ratio.

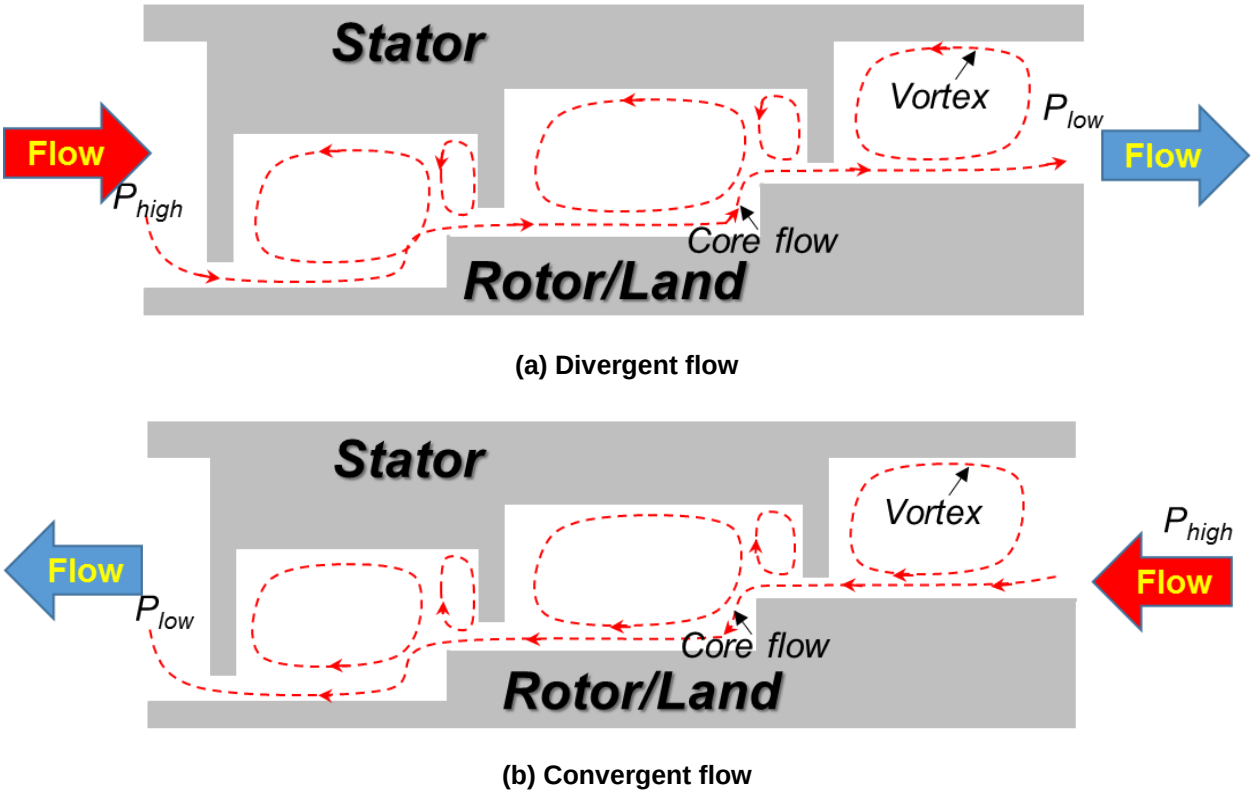

Figure 2. Schematic view of a stepped labyrinth seal: (a) diversion flow direction, and (b) conversion flow direction.

Compared to BFM predictions, CFD solutions deliver details of the flow field, which allows an in-deep knowledge of seal performance. For example, Pugachev et al. [41-43], through CFD predictions of a short comb-grooved seal, find a linear relationship between the stiffness coefficients and inlet swirl force (product of mass flow rate and inlet swirl velocity, $\dot{m} \cdot U_0$). Increasing the clearance from 0.27 mm to 0.5 mm roughly doubles the seal leakage as well as the magnitude of direct stiffness, and halves the cross-coupled stiffness.

In 2013, Gao and Kirk [44] numerically investigate an ILSs with a commercial CFD software and applied a rotating frame transformation to convert the transient state flow (with a whirling

rotor) to a steady state one. The authors assume the rotordynamic force coefficients are frequency independent. Unfortunately, prior test results [2] show the rotordynamic force coefficients of the ILs are frequency dependent. Therefore, the obtained CFD predictions may need further validation.

Recently, the rapidly increased computational capacity, as well as the development of advanced algorithms (e.g., Genetic Algorithm), promote research on seal geometry optimization. In 2016, Dai et al. [45] utilize the Genetic Algorithm to identify the optimal configuration of a labyrinth seal. Multiple advanced designs are examined in detail through CFD simulations. In comparison to the baseline geometry (straight tooth see-through labyrinth seal), seals with grooves on the tooth tips show an improvement of 16% in sealing efficiency.

Rai et al. (2016) [46] utilize a 2D CFD analysis to assess the improvement in the leakage performance of a labyrinth seal and propose a new seal configuration with "air-curtains" (air injection) from the stator. The air-curtains work as fluidic barriers breaking the jet through flow in the seal leakage path. The CFD analysis evidence that implementing air-curtain in the labyrinth seal could reduce leakage by up to 50% of the conventional LS design.

Although the improvement in computational capability, 3D CFD simulations are still time-consuming and computationally expensive when compared to the BFM. For example, Migliorini et al. (2012, 2014) [47, 48] present a new CFD/Bulk-flow hybrid method to determine rotordynamic coefficients of gas seals. Briefly, the authors utilize CFD to determine the steady-state bulk-flow variables (pressure and averaged velocities across the clearance), and a bulk-flow perturbation method to obtain the reaction forces of an eccentric whirling rotor. This hybrid method predictions show better accuracy with experimental results in Ref. [49], as compared to a conventional BFM. With a computation time on the order of a typical bulk-flow analysis, the

CFD/BFM hybrid method predicts rotordynamic characteristics comparable to the full 3D transient CFD analysis.

Recently, San Andrés et al. [50] present a CFD modified BFM analysis for circumferentially shallow grooved liquid seals. Integrating the friction factors and the penetration angles in a cavity derived from CFD results into an original BFM, the authors show a significant improvement of the BFM predictions. The BFM predictions show agreement within 14% compared to experimental estimated rotordynamic force coefficients in Ref.[51].

In 2018, Cangioli et al. [52] test a staggered labyrinth seal report(C_r = 0.5 mm, average tooth pitch is 3 mm, D = 220 mm). The authors test the seals at a rotor speed of 12,000 rpm (½$D\Omega$ = 138 m/s) while the supply pressure ranges from 64.6 bar to 91.9 bar ($PR = P_{out}/P_{in}$ = 0.72, 0.77). Cangioli et al. [52] modify a BFM by taking the inlet and outlet regions into consideration in the rotordynamic force coefficients calculation. The modified BFM shows an improved accuracy in rotordynamic force coefficients predictions when compared to the test results.

In 2019, Wu and San Andrés [53] presents a computational fluid dynamic (CFD) investigation quantifying the effects of labyrinth seal geometry and operating conditions on the rotor and stator circumferential friction factors ($f_{r\theta}$, $f_{s\theta}$). These are needed to improve bulk-flow model (BFM) predictions of the evolution of circumferential flow velocity and the seal force coefficients. The paper systematically studied the effects of operating conditions and seal geometry on the wall friction factors and derived new coefficients for the Blasius's friction factor model.

Recently, San Andrés et al. [54] report measurements of mass flow rate and cavity pressures for an interlocking labyrinth seal (ILS) operating over a wide range of supply and exit pressures and rotor speeds. The measurements show rotor speed has a negligible effect on the seal leakage. Both CFD and BFM predictions of leakage show a very good agreement with the test data. In this

work, the authors find a unique loss coefficient for the four cavity ILS that is valid for all operating conditions.

For labyrinth seals, mechanical energy dissipation is achieved through a series of flow restrictions (teeth) and sudden expansions in the deep cavities. As the fluid accelerates through the narrow tip clearance below a sharp tooth, a fraction of its pressure (head) is converted into kinetic energy, and which is dissipated through small scale turbulence-viscosity interaction in the immediate cavity downstream. To estimate the mass flow rate in a LS engineering analyses use Neumann's [30] formula, $\dot{m}_i = \mu_{1i}\mu_{2i}\left(\pi DC_r\right)\sqrt{P_{i-1}^2 - P_i^2/R_gT}$, $i = 1,2,\cdots$, an orifice like equation relating flow to pressure drop, and that uses a flow coefficient (μ_{2i})and a kinetic energy carry-over (μ_{1i}) coefficient [55]. For both TOS LS and TOR LS, $\mu_{1i} = \sqrt{NT/[(1-\lambda)NT + \lambda]}$, $\lambda = 1-\left(1+16.6\ C_r / L_i\right)^{-2}$ depends on the seal clearance C_r, cavity width or tooth pitch L_i, and total teeth number NT; whereas, μ_{1i} = 1 in an ILS [55].

For a LS having a large C_r/L_i ratio, simple bulk-flow model (BFM) could not accurately predict the mass flow rate. Thus, better assessing the kinetic energy carry-over coefficient in a LS is of great significance to improve BFM leakage predictions, and a modification of the bulk-flow model with CFD derived results could be a practical way.

In sum, the bulk-flow model is efficient to model leakage and force coefficients but lacks accuracy due to its multiple simplifications (e.g., the empirical coefficients in the friction factor model), whereas CFD simulations, although requiring more intellectual effort as well as computing time, shows better agreements with test results. Therefore, a modification of the bulk-flow model with CFD derived results could be a practical way to improve the accuracy of the BFM predictions.

III. BULK-FLOW MODLE PREDICTION OF LABYRINTH GAS SEALS[4]

3.1 Governing Equations

In 1986, Childs and Scharrer [27] (based on Iwatsubo's model [25, 26]) derived the equations of a one control volume bulk flow model for a labyrinth seal. The following update follows the same method. Figure 3 shows schematic views of an ILS with radial clearance C_r and rotor radius R_s. Teeth on both the rotor and the stator have the same geometry, with B as a tooth height and L_i as a tooth pitch.

The flow domain is divided into n cavities separated by blades. As Figure 4 shows, within the i^{th} cavity, the pressure is P_i, and the mean circumferential velocity is U_i. The velocity U_i differs from one cavity to the next, but it is sufficiently similar in a single cavity to permit its bulk flow representation. The mass flow rate through the upstream and downstream teeth $\dot{m}_i=\dot{m}_{i+1}$.

The gas density (ρ_i) follows the ideal gas law, $\rho_i=P_i/(Z_gR_gT)$, where R_g and Z_g are the gas constant and the gas compressibility factor, and T is the gas temperature[5]. Figure 5 depicts the forces on a control volume, and which serves to derive the circumferential momentum equation.

In a cavity, the flow mass conservation equation and momentum transport equation along the circumferential (θ) direction are [27]:

$$\frac{\partial(\rho_i A_i)}{\partial t}+\frac{\partial(\rho_i U_i A_i)}{R_s\ \partial\theta}+\bar{\dot{m}}_{i+1}-\bar{\dot{m}}_i=0 \tag{1}$$

$$\frac{\partial(\rho_i U_i A_i)}{\partial t}+\frac{\partial(\rho_i A_i U_i^{\,2})}{R_s\ \partial\theta}=-\frac{A_i}{R_s}\frac{\partial P_i}{\partial\theta}+(\tau_{r_i}a_{r_i}-\tau_{s_i}a_{s_i})L_i \tag{2}$$

[4] This part has been reproduced from "Gas Labyrinth Seals: on the Effect of Clearance and Operating Conditions on Wall Friction Factors – a CFD Investigation" by Wu, T., and San Andrés, L., 2019, Tribol. Int, 131, pp. 363-376.

[5] Since experimental investigations do not show significant temperature changes throughout the seal, the model assumes isothermal flow conditions [5].

where $A_i = (B + C_r)L_i$ is the area of a cavity cross-section.

Using Neumann's equation [2] that relates the mass flow rate ($\dot{m}$) through a tooth clearance (C_r) as a function of the upstream (P_{i-1}) and downstream (P_i) cavity pressures,

$$\bar{\dot{m}}_i(\pi D) = \dot{m}_i = \mu_{1i}\mu_{2i}(\pi D C_r)\sqrt{\frac{P_{i-1}^2 - P_i^2}{R_g T}},\ i = 1, 2, \cdots, N \tag{3}$$

where, μ_{1i} is a kinetic energy carry-over coefficient, and μ_{2i} is a flow discharge coefficient, see Ref. [2].

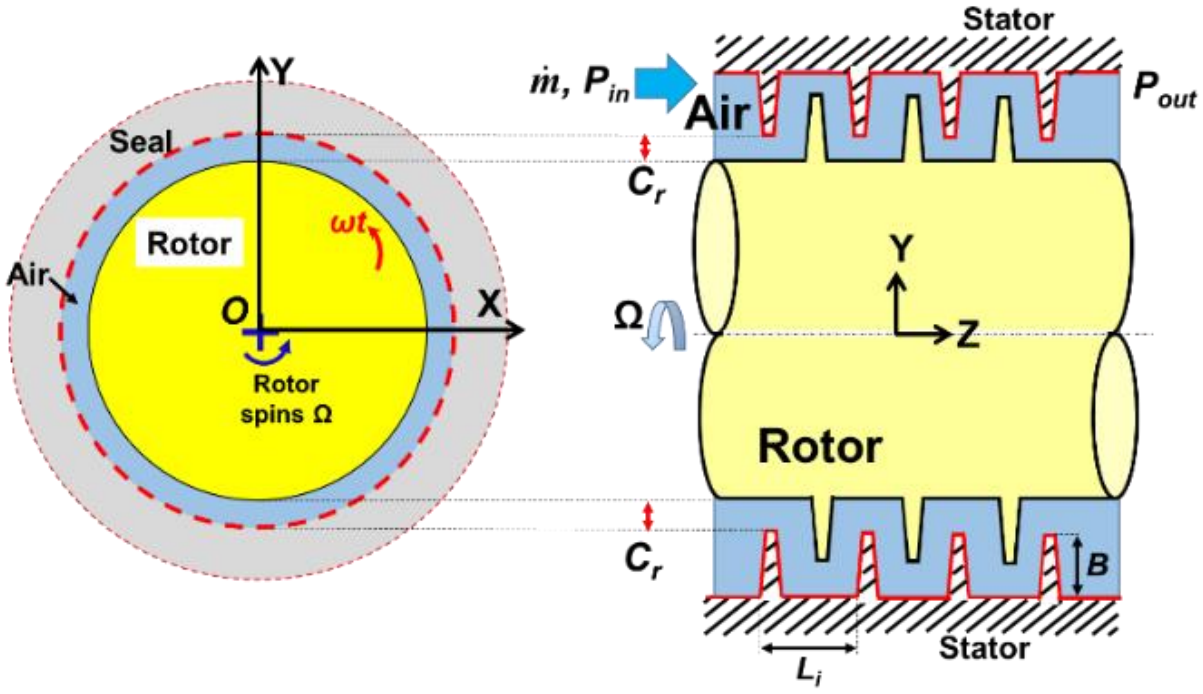

Figure 3. Schematic view (not to scale) of an interlocking labyrinth seal (ILS).

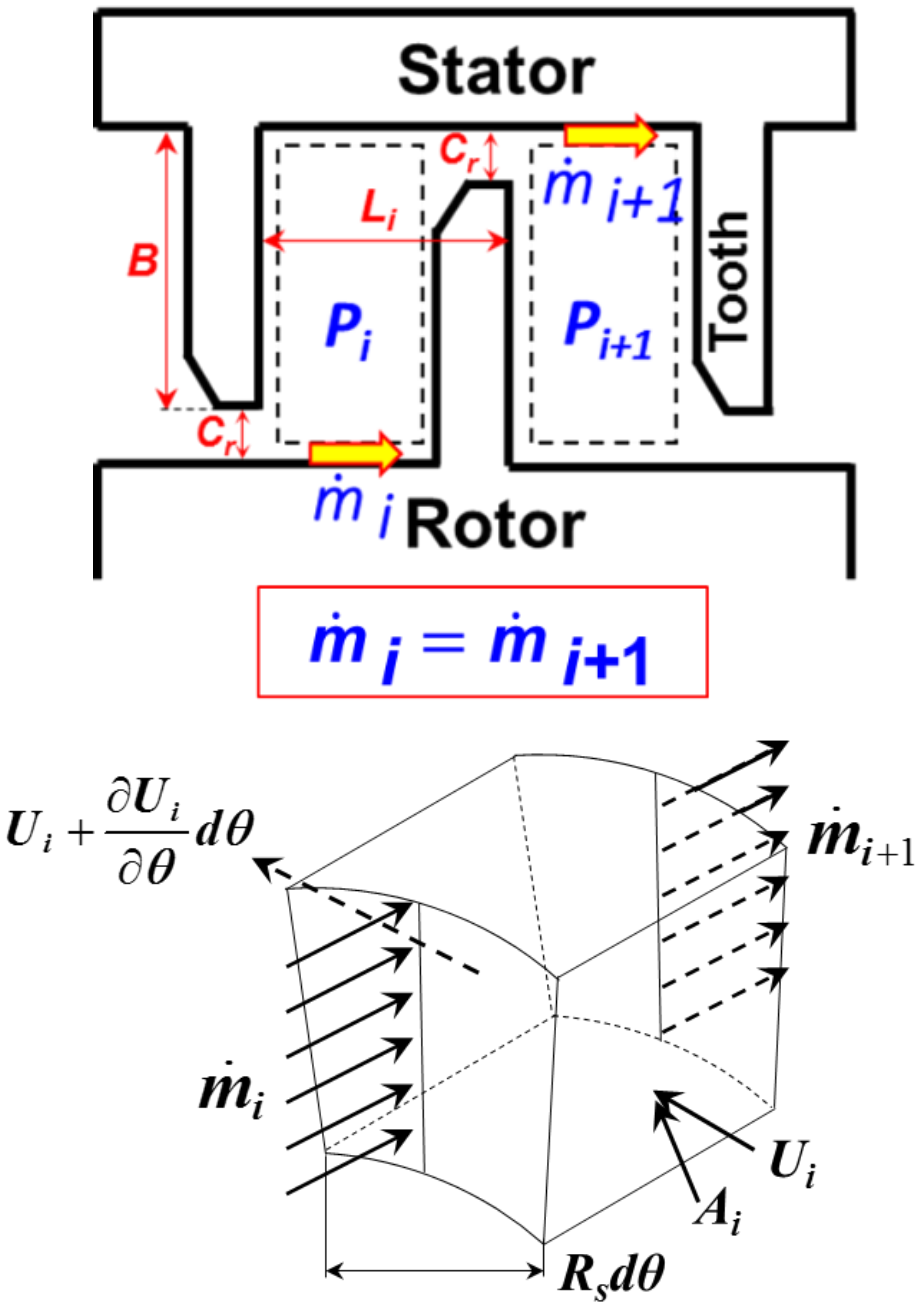

Figure 4. Schematic views of a one-control-volume model (*i* = the cavity number).

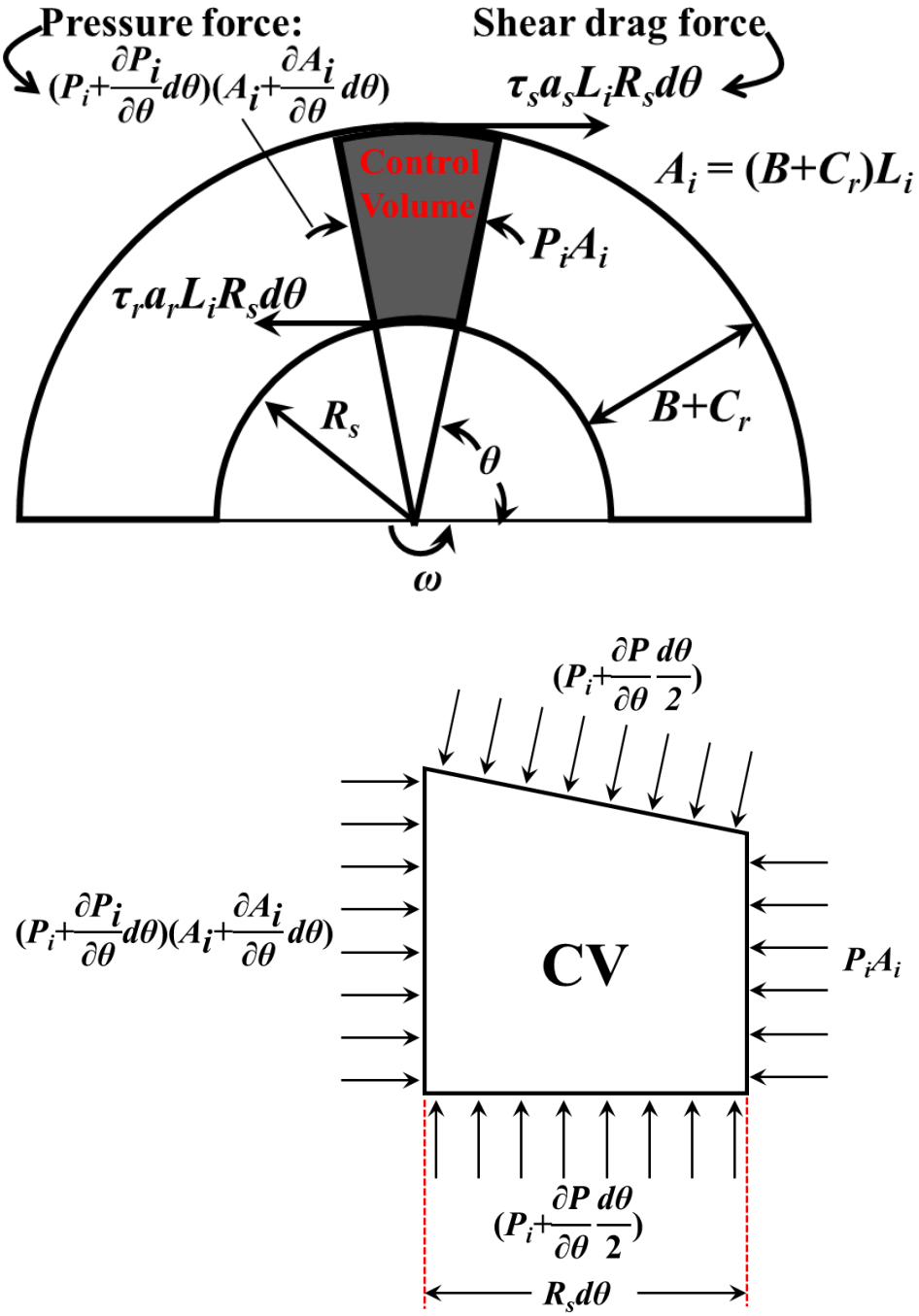

Figure 5. Forces on the control volume of a labyrinth seal (*i* = the cavity number).

For a *see-through* labyrinth seal (TOR or TOS) with diameter *D*, the Neumann's empirical leakage equation (Eqn. (4)) with Chaplygin's [30] flow coefficient (μ_{2i}) predicts the gas leakage

($\dot{m}$) across a seal tooth with tip clearance C_r [2, 31]. For a *see-through* (TOR a TOS) labyrinth seal, the kinetic energy carry-over coefficient (μ_{1i}) is a function of the seal geometry

$$\mu_{1i} = \left(\frac{NT}{(1-\lambda)NT + \lambda} \right)^{\frac{1}{2}} \tag{4}$$

$$\lambda = 1 - \left(1 + 16.6\, C_r / L_i\right)^{-2} \tag{5}$$

For the first tooth in a see-through LS and all the teeth in an ILS, μ_{1i} equals unity [2]. Note λ is constant in a seal with uniform teeth spacing (cavity widths and depth).

Consider as an example a TOS LS with seven teeth, C_r = 0.2 mm and L_i = 5 mm, C_r/L_i = 0.04; and Figure 8(a) thus shows the change of μ_1 with respect to the ratio C_r/L_i. μ_1 increases monotonically with C_r/L_i, starts at a magnitude of one and approaches to a maximum value ~2.6.

The flow discharge coefficient μ_{2i} uses Chaplygin's formula, Gurevich (1966) [2, 31] and equals

$$\mu_{2i} = \frac{\pi}{\pi + 2 - 5\beta_i + 2\beta_i^2} \tag{6}$$

with

$$\beta_i = \left(\frac{P_{i-1}}{P_i} \right)^{\frac{\gamma-1}{\gamma}} - 1 \tag{7}$$

where γ is the ratio of specific heats. For air, γ=1.4. Figure 8(b) shows the change of μ_2 with respect to the pressure ratio (P_{i-1}/P_i). Note μ_2 is proportional to the increase in cavity pressures (upstream/downstream). Prior to the flow choking across a tooth, the largest (P_{i-1}/P_i) is, the higher μ_2 becomes.

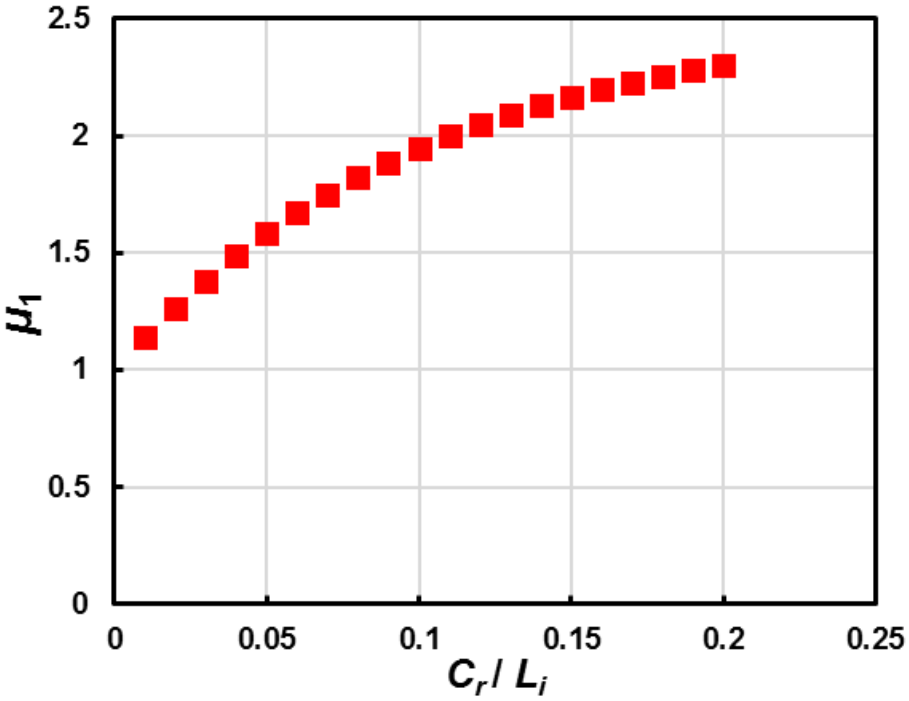

(a) μ_1 vs. C_r/L_i

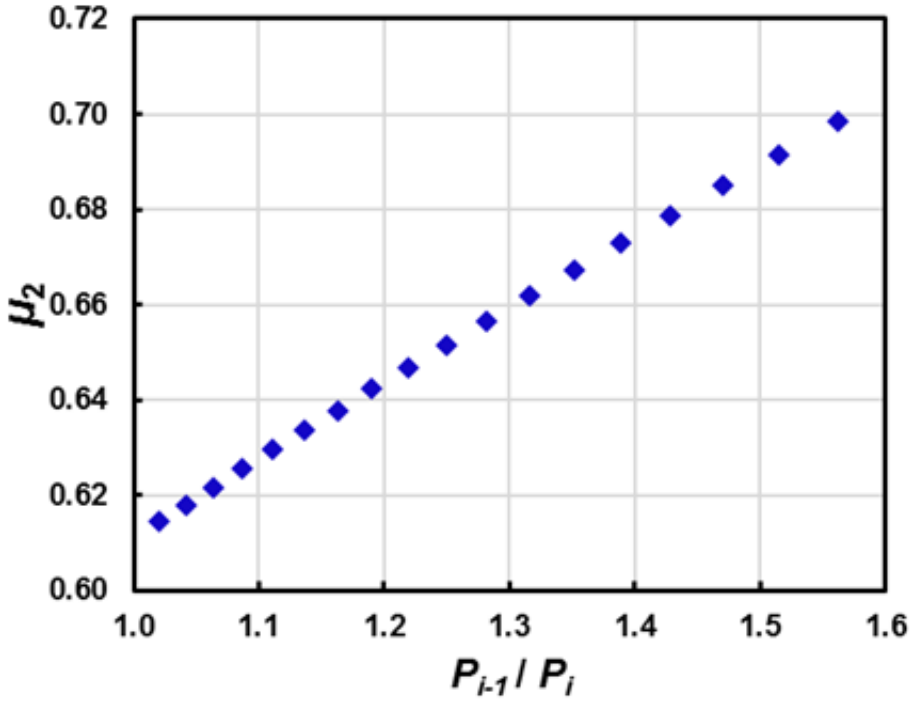

(b) μ_2 vs. (P_{i-1}/ P_i)

Figure 6. A sample see-through labyrinth seal with seven teeth: (a) variation of kinetic energy carry-over coefficient μ_1 vs. C_r/L_i; and (b) flow discharge coefficient μ_2 vs. (P_{i-1}/ P_i) : cavity pressures upstream/downstream.

In Eq. (2) a_{r_i} and a_{s_i} are dimensionless lengths introduced in Ref. [5]. For **TOR LS**: $a_{r_i} = (2B + L_i)/L_i$, $a_{s_i} = 1$; **TOS LS**: $a_{r_i} = 1$, $a_{s_i} = (2B + L_i)/L_i$. Since the **ILS** has teeth both on stator and rotor, $a_{r_i} = a_{s_i} = (B + L_i)/L_i$.

The shear stress (τ_{r_i}, τ_{s_i}) acting on the rotor and stator are defined in terms of friction factors (f_r, f_s) [5].At the rotor surface,

$$\tau_{r_i} = f_{r_i}\left(\frac{1}{2}\rho_i U_{r_i}^{\ 2}\right) = n_r Re_r^{\ m_r}\left(\frac{1}{2}\rho_i U_{r_i}^{\ 2}\right) \tag{8}$$

where $$Re_r = \frac{\left|R_s\Omega - U_i\right| D_{h_i}}{\nu_i},\ U_{ri} = R_s\Omega - U_i$$

And at the stator surface, $$\tau_{s_i} = f_{s_i}\left(\frac{1}{2}\rho_i U_{s_i}^{\ 2}\right) = n_s Re_s^{\ m_s}\left(\frac{1}{2}\rho_i U_{s_i}^{\ 2}\right) \tag{9}$$

where $$Re_s = \frac{\left|U_i\right| D_{h_i}}{\nu_i},\ U_{s_i} = U_i$$

Above (n_r, m_r) and (n_s, m_s) are empirical coefficients of Blasius friction model (usually for a smooth surface, $n_r = n_s = 0.079$, $m_r = m_s = -0.25$) [5], and D_{h_i} is the hydraulic diameter

$$D_{h_i} = \frac{2(C_r + B)L_i}{(C_r + B + L_i)} \tag{10}$$

Following Childs and Scharrer [27], subtracting Eqn.(1) times U_i from Eqn.(2) yields the following primitive form of the momentum Eqn. (2):

$$\rho_i A_i \frac{\partial U_i}{\partial t} + \rho_i U_i A_i \frac{\partial U_i}{R_s \partial\theta} + \bar{\dot{m}}_i (U_i - U_{i-1}) = -\frac{A_i}{R_s}\frac{\partial P_i}{\partial\theta} + (\tau_{r_i} a_{r_i} - \tau_{s_i} a_{s_i}) L_i \tag{11}$$

At the seal inlet and exit planes, the pressure undergoes a pressure drop and rise due to fluid inertia. Let $W = (\dot{m}/\rho)/(\pi D C_r)$ be a bulk-flow axial velocity. Then

$$P_i = P\big|_{z=0} = P_{in} + \frac{\rho}{2}(1+\xi)W^2\Big|_{z=0} \tag{12}$$

$$P_i = P\big|_{z=L} = P_{out} + \frac{\rho}{2}C_s W^2\Big|_{z=L} \tag{13}$$

where ξ is an entrance pressure loss coefficient, and C_s is an exit pressure recovery coefficient. In addition, the entrance circumferential velocity into the seal is $U\big|_{z=0} = \alpha R\Omega$, with α as a known inlet pre-swirl ratio.

3.2 Leakage, Pressure Distribution and Circumferential Velocity

For a LS gas flow that is unchoked, the ratio of inlet (supply) pressure (P_{in}) and outlet (discharge) pressure (P_{out}) must satisfy [56]:

$$\frac{P_{in}}{P_{out}} < r_c = \left(\frac{\gamma+1}{2}\right)^{\frac{\gamma}{\gamma-1}} \sqrt{b_1\mu_1^{\,2} + b_1(NT-2)+1} \quad (=4.4, \text{ for ILS listed in Table 1}) \tag{14}$$

where, $b_1 = 1-\left(\frac{\gamma+1}{2}\right)^{-\frac{2\gamma}{\gamma-1}}$ (=0.729, for air). Thus, in the BFM, the first step checks whether the flow is choked or not through Eqn. (14). Note the critical pressure ratio (r_c) is a function of the number of teeth (NT). Increasing the number of teeth raises r_c.

For a *see-through* labyrinth seal (TOR or TOS) with diameter D, the Neumann's empirical leakage equation (Eqn. (3)) with Chaplygin's [57] flow coefficient (μ_{2i}) predicts the gas leakage ($\dot{m}$) across a seal tooth with tip clearance C_r [5, 56]. For a *see-through* (TOR a TOS) labyrinth seal, the kinetic energy carry-over coefficient (μ_{1i}) is a function of the seal geometry

$$\lambda = 1-\left(1+16.6\ C_r / L_i\right)^{-2} \tag{15}$$

$$\mu_{1i} = \left(\frac{NT}{(1-\lambda)NT + \lambda} \right)^{\frac{1}{2}} \tag{16}$$

For the first tooth in a see-through LS and all the teeth in an ILS, μ_{1i} equals unity [5]. Note λ is constant in a seal with uniform teeth spacing (cavity widths and depth). For a typical 7 teeth ILS (C_r = 0.2 mm, L_i = 5 mm), C_r/L_i = 0.04; thus $\lambda \sim 0.64$.

Table 1 lists the geometry and operating conditions of an ILS with four teeth on the stator and three teeth on the rotor surface (NT=7). The first tooth (facing a high pressure) is on the stator. Figure 7 depicts an axial view of the seal (ILS) with lengthy upstream and downstream sections considered for a CFD analysis. Childs [5] recommends a kinetic energy carry-over coefficient (μ_{1i}) = 1 for use in the leakage Eqn. (3) across all teeth of an interlocking seal.

Table 1. Interlocking labyrinth seal dimensions (4 teeth on stator and 3 teeth on rotor[6]), gas properties and operating conditions.

Seal Geometry	Overall length, L	41.79 mm
	Inner diameter, D	150 mm
	Radial clearance, C_r	0.2 mm
	Teeth number, NT	7
	Tooth pitch, L_i	3.75 mm
	Height, B	3 mm
	Width at tip, L_t	0.3 mm
Gas Properties	Density(at 12 bar), ρ	13.9 kg/m^3
	Kinematic viscosity, ν	1.51×10^{-5} m^2/s
	Temperature, T	300 K
Operating Conditions	Supply pressure, P_{in}	13 bar
	Discharge pressure, P_{out}	5 bar
	Pressure Ratio, $PR = P_{in}/P_{out}$	2.6
	Rotor speed, Ω	7,500 rpm ($\frac{1}{2}D\Omega \approx 59$ m/s)
	Inlet Pre-swirl Ratio, α	0

[6] ILS being tested at TAMU in 2017.

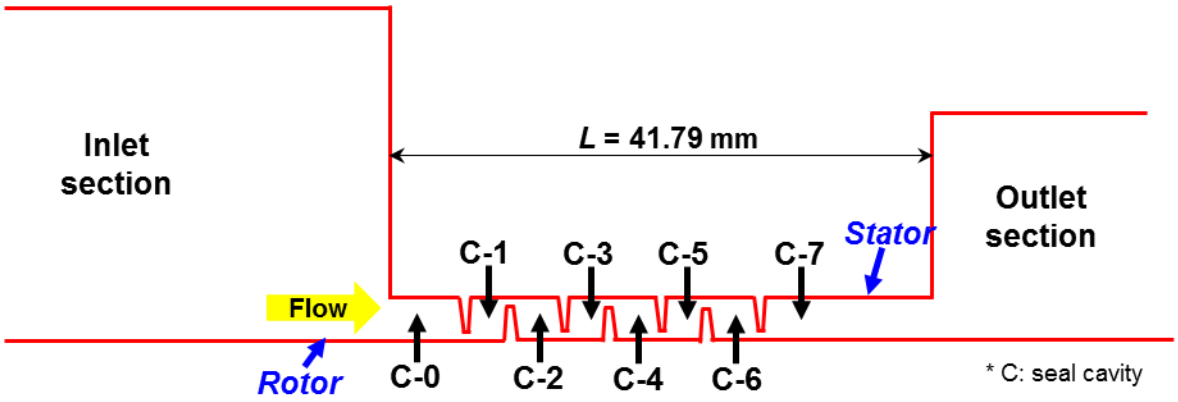

Figure 7. Schematic view of an interlocking labyrinth seal, C-: cavity number. 4 teeth on stator and 3 on rotor (*NT*=7).

For air, γ=1.4. Let, as in Ref. [56],

$$\dot{m} = \frac{\dot{m}\sqrt{R_g T}}{\pi D C_r} \tag{17}$$

Since $\dot{m} = \dot{m}_1 = \dot{m}_2 = \cdots = \dot{m}_{NT}$, and using Eqn. (3), let

$$k_1 = \frac{\dot{m}}{\mu_{2i}} = \mu_{1i}\sqrt{P_{i-1}^2 - P_i^2} \tag{18}$$

Thus, for i=1, μ_{1i}=1,

$$P_0^2 - P_1^2 = k_1^2 \tag{19}$$

Since all teeth and cavities are equal, then

$$P_1^2 - P_2^2 = \frac{k_1^2}{\mu_{1*}^2}; \quad P_2^2 - P_3^2 = \frac{k_1^2}{\mu_{1*}^2}; \quad ....; P_6^2 - P_7^2 = \frac{k_1^2}{\mu_{1*}^2} \tag{20}$$

Recall $\mu_{12} \ldots = \mu_{17} = \mu_{1*}$=1. Add Eqns. (19) and (20) to obtain

$$k_1 = \sqrt{\frac{P_0^2 - P_{NT}^2}{1 + \frac{(NT-1)}{\mu_{1*}^2}}} \tag{21}$$

with $P_0 = P_{in}$ = 1.3×10^6 Pa, $P_7 = P_{out}$ = 5×10^5 Pa; Eqn. (21) delivers k_1=6.6×10^5 Pa. The gas pressure at the first cavity follows from Eqn. (19) as $P_1^2 = k^2 - P_0^2$. Pressures in the subsequent cavities use

Eqn. (26). Next, a β_i coefficient, Eqn. (7), is calculated from the ratio $\left(P_{i-1}/P_i\right)$, and Eqn. (6) delivers the flow discharge coefficient μ_{2i}. Recall that mass flow continuity implies $\dot{m}_1=\dot{m}_2=\cdots \dot{m}_{NT}=\dot{m}$, Eqn. (3) produces the mass flow rate ($\dot{m}_i$) through each tooth.

The distribution of circumferential velocity in the seal is of importance in determining the fluid induced stresses on the shaft. Solving Eqn. (3) with the cavity pressures and mass flow rate obtained delivers the bulk-flow circumferential velocity (U_i) in each cavity.

Choked Gas Flow Case For choked flow (i.e. whose Mach number ≥1), the calculation starts with a guess pressure value of the cavity before the last tooth. With the guess pressure value of (NT-1) cavity, the mass flow rate across ($\dot{m}$) the last tooth is

$$\dot{m}_{NT} = \frac{\mu_{1\_NT}\mu_{2\_NT}\left(\pi DC_r\right)P_{NT-1}}{\sqrt{R_g T}}\sqrt{1-\left(\frac{P_{NT}}{P_{NT-1}}\right)} \tag{22}$$

Recall the mass flow continuity ($\dot{m}_i=\dot{m}_{i+1}=\cdots=\dot{m}_{NT}$); thus, the upstream cavity pressures (P_i) are obtained through the steps discussed earlier.

3.3 Flow Perturbation Analysis

For the i^{th} cavity, the continuity equation (1), circumferential momentum Eqn. (2) and leakage Eqn. (3) are the governing equations for the variables U_i, P_i, and m_i. For small amplitude rotor motions ($\Delta e_x, \Delta e_y$) of frequency ω, the film thickness (H) as depicted in Figure 8 is

$$H = C_r + e^{j\omega t}(\Delta e_x \cos\theta + \Delta e_y \sin\theta) \tag{23}$$

The velocity and pressure fields are expressed as the sum of a zeroth order and first order complex fields, describing the equilibrium condition and the perturbed motions, i.e.

$$\phi = \phi\{P, U, W\} = \phi_0 + e^{jwt}(\Delta e_x \ \phi_x + \Delta e_y \ \phi_y),\ j = \sqrt{-1} \tag{24}$$

Substitution of the flow variables into the governing equations yields the differential equations for the zeroth and first-order flow fields.

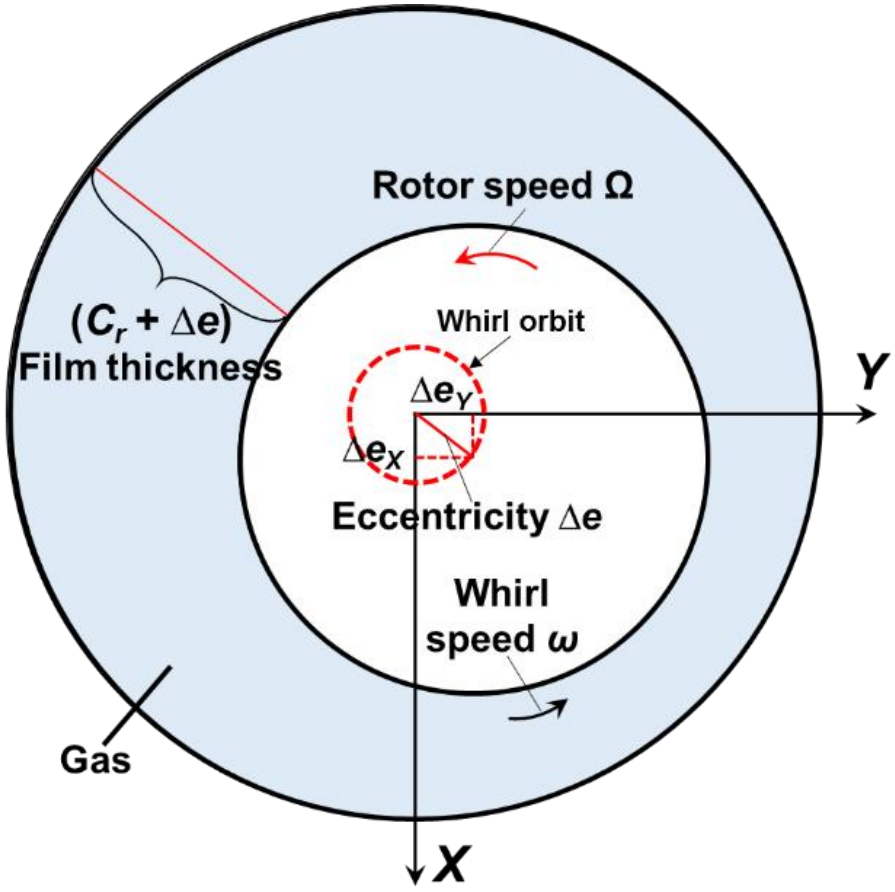

Figure 8. Small amplitude rotor motions about the centered position.

The zeroth order flow equations

$$\bar{\dot{m}}_i = \bar{\dot{m}}_{i+1}\ ,\ i = 1, 2, 3, \ldots \tag{25}$$

$$\bar{\dot{m}}_0 (U_{0i} - U_{0i-1}) = (\tau_{r0i} a_{r_i} - \tau_{s0i} a_{s_i}) L_i \tag{26}$$

determine the mass flow rate $\dot{m}_0$, the cavity pressures (P_{i0}) and the velocity field (U_{i0}) for a rotor centered position. First-order equations are not detailed for brevity.

Childs [5] details the procedure to solve the partial differential equations governing the fluid flow. The perturbation analysis renders the seal static and dynamic reaction forces as

$$-\begin{bmatrix} F_{X(\omega)} \\ F_{Y(\omega)} \end{bmatrix} = -\begin{bmatrix} F_{X0} \\ F_{Y0} \end{bmatrix} + \begin{bmatrix} D_{(\omega)} & E_{(\omega)} \\ G_{(\omega)} & F_{(\omega)} \end{bmatrix} \begin{bmatrix} X_{(\omega)} \\ Y_{(\omega)} \end{bmatrix} \tag{27}$$

The functions *D*-*F* are frequency-dependent and obtained as

$$\begin{bmatrix} D \\ G \end{bmatrix}_{(\omega)} = R_s \int_0^L \int_0^{2\pi} P_X \begin{bmatrix} \cos\theta \\ \sin\theta \end{bmatrix} d\theta\, dz; \begin{bmatrix} E \\ F \end{bmatrix}_{(\omega)} = R_s \int_0^L \int_0^{2\pi} P_Y \begin{bmatrix} \cos\theta \\ \sin\theta \end{bmatrix} d\theta\, dz \tag{28}$$

Note that for motions about a centered rotor position, $D = F(j\omega)$, $E = -G$. Stiffness and damping coefficients follow from

$$K_{(\omega)} + j\,\omega C_{(\omega)} \leftarrow D_{(\omega)};\; k_{(\omega)} + j\,\omega c_{(\omega)} \leftarrow E_{(\omega)} \tag{29}$$

The BFM analysis procedure is well documented in Refs. [5, 27, 58]. In brief, the BFM solution procedure follows the steps:

(1) Determine whether the flow is choked or not by comparing the inlet pressure against the critical inlet pressure (as discussed later);

(2) Calculate the mass flow rate, cavity pressure distribution and the cavity circumferential velocity.

(3) Solve the first order (perturbed) equations for a given whirl frequency (ω), integrate the dynamic pressure acting on the rotor surface to calculate the reaction forces, and thus obtaining the rotordynamic force coefficients.

IV. CFD MODEL ANALYSIS[7]

Predictions of rotordynamic force coefficients using a BFM strongly depend on the wall friction factors as well as the leakage (Neumann's) equation. Prior investigations evidence the friction factor is a function of the seal operating conditions and the seal geometry. The Blasius friction model currently used in the BFM is only a function of the Reynolds number ($f = n\,\mathrm{Re}^{m}$, typically n = 0.079, and m = -0.25).

The momentum Eqn. (2) shows that only the circumferential direction friction factors ($f_{r\theta}$, $f_{s\theta}$) are of interest in the BFM. Therefore, only $f_{r\theta}$ and $f_{s\theta}$ are quantified in this work. The TOS seal geometry and its operating conditions applied in this work are based on a TOS labyrinth seal tested by Vannini et al. (2014) [59]. Table 2 details the TOS labyrinth seal geometry and operating parameters. Figure 9 shows a schematic view of the TOS labyrinth seal, having 14 teeth on the stator. The teeth are equally distributed with pitch length L_i of 5 mm. To investigate the effect of seal geometry and operating conditions on the friction factors, the seal clearance varies[8] from $0.8C_r$ to $1.2C_r$for the three types of LS. Similarly, perturbations also apply to the seal operating conditions. For all TOS labyrinth seals (various radial clearances), the rotor speed ranges from 7,000 rpm to 15,000 rpm. Air enters the seal with supply pressure P_{in} = 60, 73, 100 bar (absolute) and room temperature (27 ^{o}C). The seal outlet the exit pressure (P_{out}) is set to determine a pressure ratio ($PR = P_{out}/P_{in}$) ranging from 0.4 to 0.85.

[7] This part has been partially reproduced from "Gas Labyrinth Seals: on the Effect of Clearance and Operating Conditions on Wall Friction Factors – a CFD Investigation" by Wu, T., and San Andrés, L., 2019, Tribol. Int, 131, pp. 363-376.

[8] The radial clearance C_r varies ±20% in this work. A larger change in radial clearance, up to $2C_r$, is recommended for a later study.

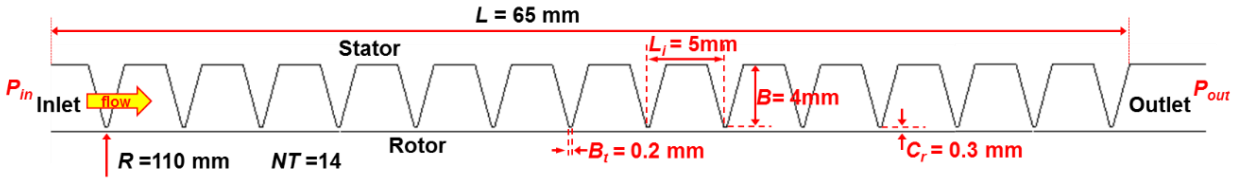

Figure 9. Schematic view of TOS labyrinth gas seal in Ref. [59].

Table 2. Dimensions and operating conditions of the teeth-on-stator (TOS) labyrinth seal in Ref. [59].

Seal Geometry	Seal length, L	65 mm
	Rotor diameter, D	220 mm
	Radial clearance, C_r	0.3 mm
	Teeth number, NT	14
	Tooth pitch, L_i	5 mm
	Height, B	4 mm
	Width at tip, b_t	0.2 mm
Air Properties (ideal gas)	Density, ρ @13bar	15.1 kg/m^3
	Temperature, T	300 K
	Sound speed, V_s	314 m/s
	Viscosity, ν	1.51×10^{-5} m^2/s
Operating Conditions	Supply pressure, P_{in}	60 bar ~ 100 bar
	Pressure ratio, $PR= P_{out}/P_{in}$	0.40 ~ 0.85
	Pre-swirl velocity, U_0	0 ~ 0.72 $R\Omega$
	Rotor Speed, Ω ($R\Omega$)	5-15 krpm (58 ~173 m/s)

Figure 10 shows the computational domain and corresponding mesh for the TOS labyrinth seal with nominal radial clearance. 15 mm in length extensions at the seal upstream and downstream flow sections capture the flow field before and after the seal section, respectively. Various mesh sets, their total node count ranging from 2.8 million to 10 million, serve to conduct a mesh independence analysis, see Table 3. The grid independence analysis is not discussed here for simplicity. The grid independence test indicates a mesh with 8.7 million nodes is sufficient to capture the flow field characteristics.

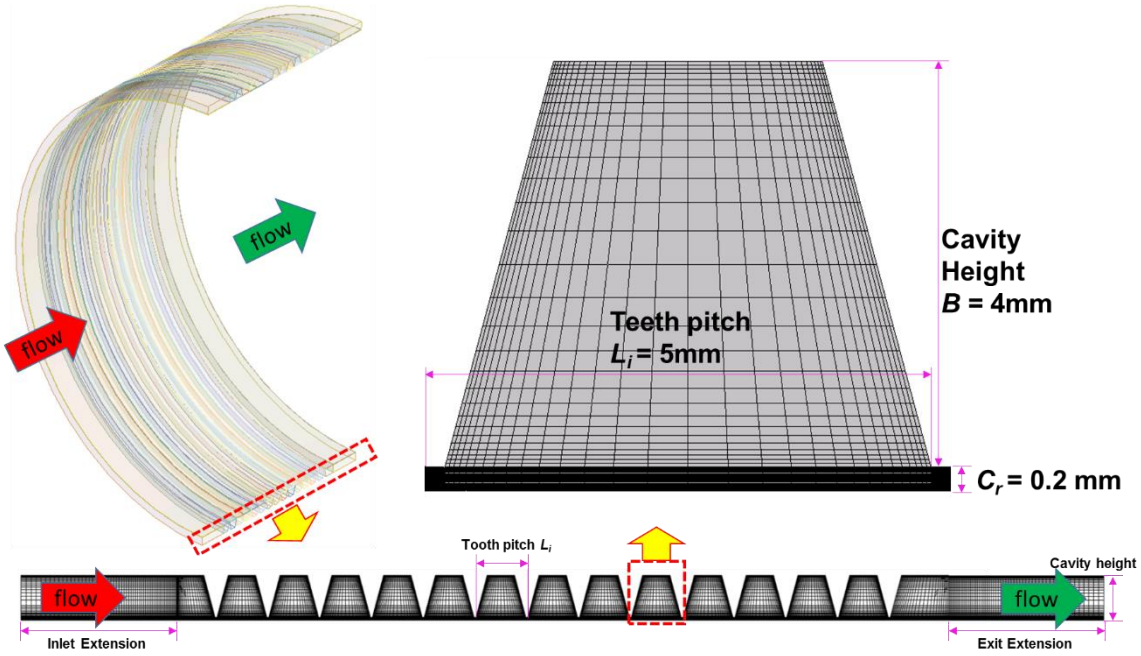

Figure 10. CFD mesh for a TOS labyrinth gas seal.

Table 3. Details of mesh distribution for model labyrinth seals.

	Node number/ mesh size
Radial clearance	30
Tooth section	30
Cavity depth/length	30
Circumferential	180 (2° apart)
Min. mesh orthogonal quality	0.99

V. CFD DERIVED FRICTION FACTORS[9]

Recall the circumferential wall friction factors ($f_{r\theta} = n_r Re^{mr}$, $f_{s\theta} = n_s Re^{ms}$) are functions of the circumferential Reynolds numbers,

$$Re_{r\theta} = \rho\left(U - R\Omega\right) D_h \big/ \mu \tag{30}$$

$$Re_{s\theta} = \rho U D_h \big/ \mu \tag{31}$$

For a compressible fluid, the density (ρ) is a function of the local pressure, thus varying from cavity to cavity. From the seal inlet plane towards the outlet plane, the circumferential flow velocity develops. Recall, the BFM assumes the cavity pressure (and density), and the circumferential velocity are constant within a cavity. Therefore, all the above variables extracted from CFD results for a friction factor analysis should correspond to the width and radial depth across film average values of a whole cavity.

Figure 11(a) shows the contours of density along the seal. The density within a cavity (#1-#13) is almost uniform; and so does the tangential velocity in a cavity. Figure 11(c) and (d) depict the average (normalized) density (ρ/ρ_s) and the average (normalized) circumferential velocity (U/U_{rotor}, $U_{rotor} = R\Omega$) from the seal inlet plane to the outlet plane.

[9] This part has been partially reproduced from "Gas Labyrinth Seals: on the Effect of Clearance and Operating Conditions on Wall Friction Factors – a CFD Investigation" by Wu, T., and San Andrés, L., 2019, Tribol. Int, 131, pp. 363-376.

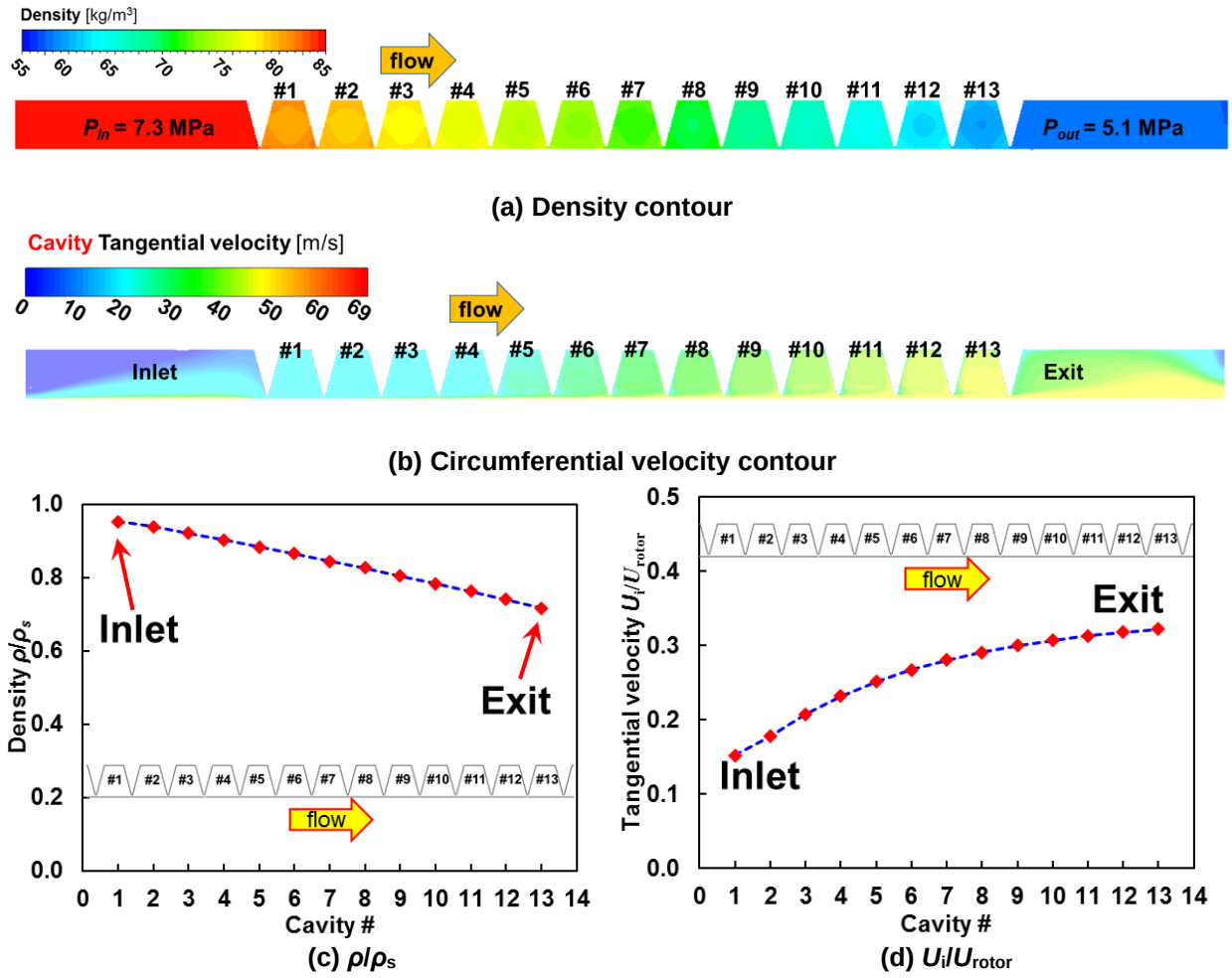

Figure 11. CFD predictions for a TOS LS: (a) density contours; (b) circumferential velocity contours; (c) averaged cavity density (ρ/ρ_s); (d) averaged cavity tangential velocity (U_i/U_{rotor}). P_{in} = 7.3 MPa, P_{out} = 5.1 MPa, rotor speed = 12 krpm (138 m/s).

5.1 Effect of Radial Clearance (C_r) on Friction Factor f_θ

Figure 12 shows the wall shear stresses, $\tau_{r\theta}$ and $\tau_{s\theta}$, on the rotor and stator surfaces, along the axial direction for three radial clearances (C_r). The CFD predictions show $\tau_{r\theta} \gg \tau_{s\theta}$, i.e. a larger drag on the rotor surface than on the stator. An increase in radial clearance, from $0.8\times C_r$ to $2\times C_r$, increases the rotor surface shear stress ($\tau_{r\theta}$); whereas the stator surface shear stress ($\tau_{s\theta}$) decreases. As expected, the seal leakage is sensitive to changes in radial clearance, as a ±20% change in

clearance causes ~±30% variation in seal leakage. On the other hand, doubling the radial clearance increases leakage by 175%.

Figure 13 depicts the average cavity circumferential velocity (U_i/U_{rotor}) as well as the cavity density (ρ/ρ_s) versus axial length for four clearances, (0.8, 1, 1.2, 2)×C_r. Interestingly, the CFD results show the static pressure (P) distribution does not change with clearance (C_r); thus, the cavity density ($\rho \sim P$) distribution remains the same in spite of the changes in radial clearance. Figure 13 (b) depicts the evolution of the circumferential velocity U (cross film average) in each cavity. Recall the null inlet pre-swirl velocity, $U \approx 0$ at the seal entrance plane. Due to the rotor surface shear stress, the circumferential velocity develops and increases from the seal inlet towards the exit. As expected, U decreases for a seal with a large radial clearance (2×C_r). Here note the flow within the 1st cavity shows a stronger recirculation zone for the LS with a larger radial clearance, and which contributes to a decrease in that cavity circumferential velocity. Note that, the tighter the clearance is, the larger U_i/U_{rotor} is, and $U_i/U_{rotor} \rightarrow 0.3$ at the seal exit plane.

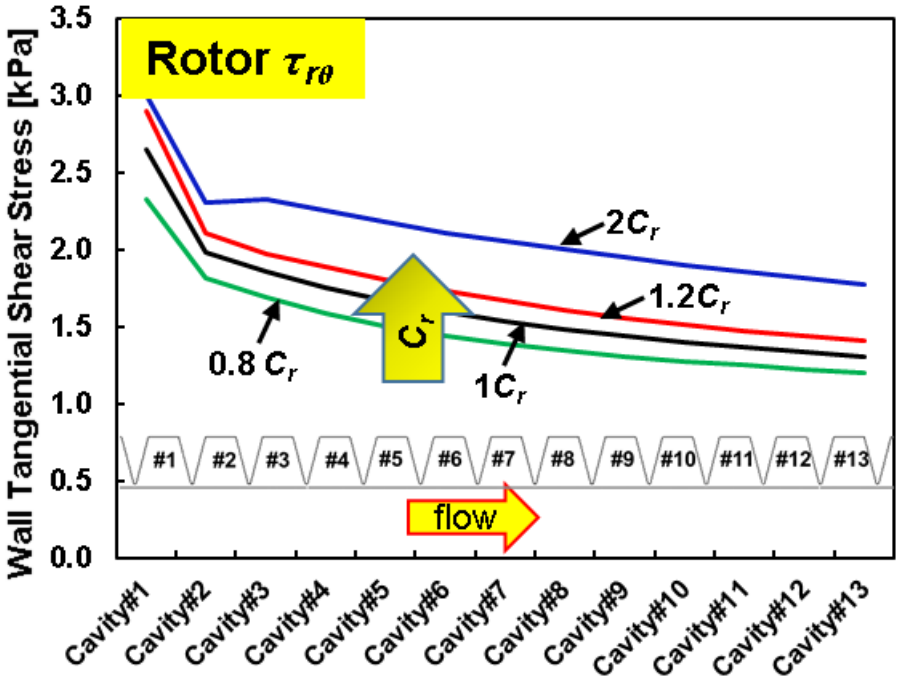

(a) $\tau_{r\theta}$ (rotor)

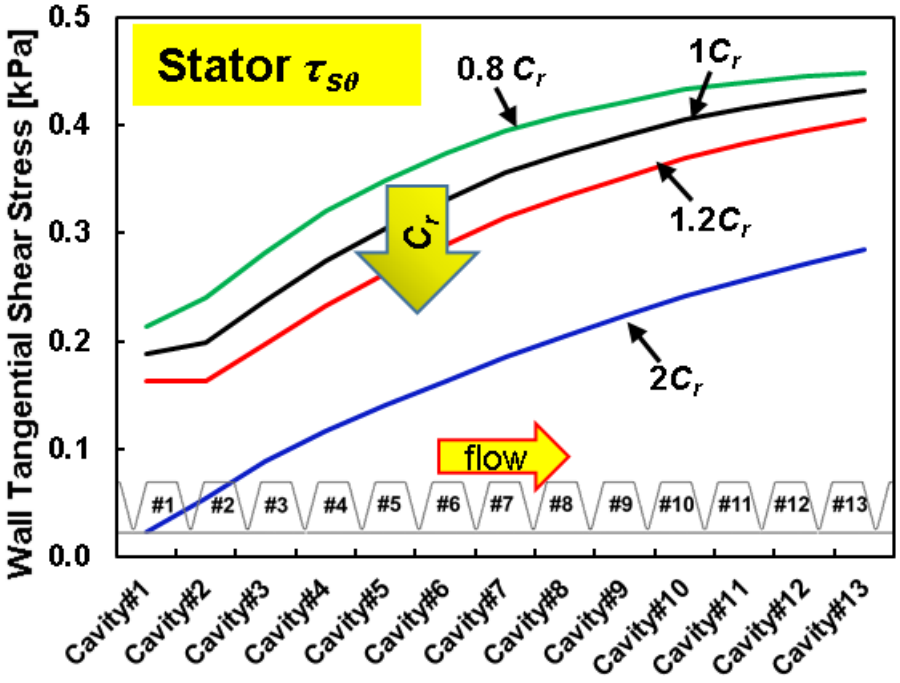

(b) $\tau_{s\theta}$ (stator)

Figure 12. Wall shear stresses $\tau_{r\theta}$ and $\tau_{s\theta}$ vs. cavity # for four radial clearances (0.8, 1, 1.2, 2)×C_r: (a) rotor surface $\tau_{r\theta}$; (b) stator surface $\tau_{s\theta}$. TOS LS: P_{in} = 7.3 MPa, P_{out} = 5.1 MPa, rotor speed = 12 krpm ($R\Omega$ = 99 m/s), α_{inlet} = 0.

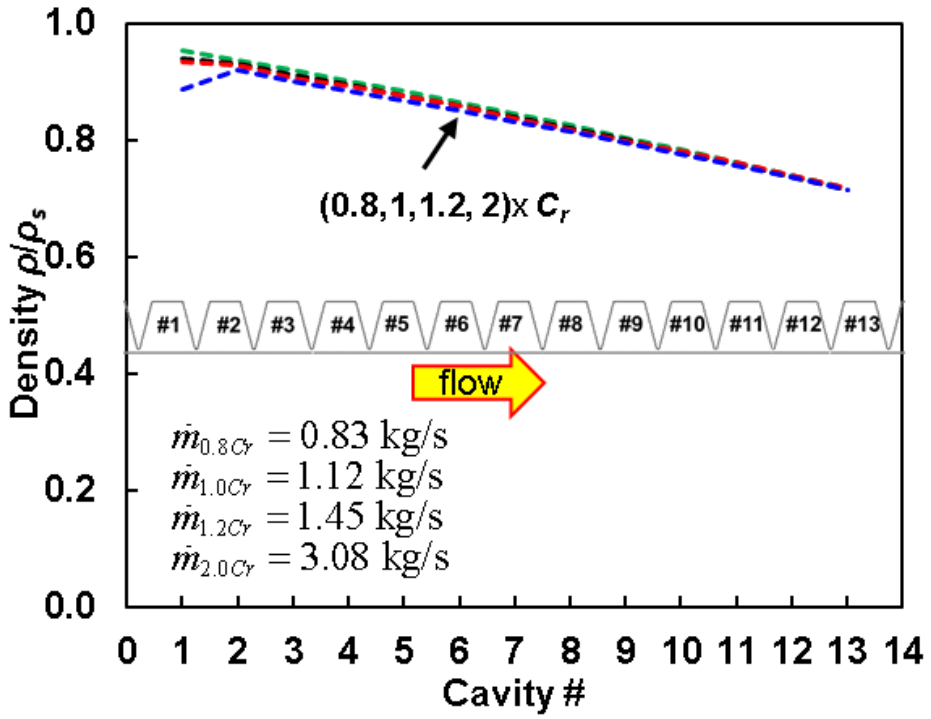

(a) ρ/ρ_s

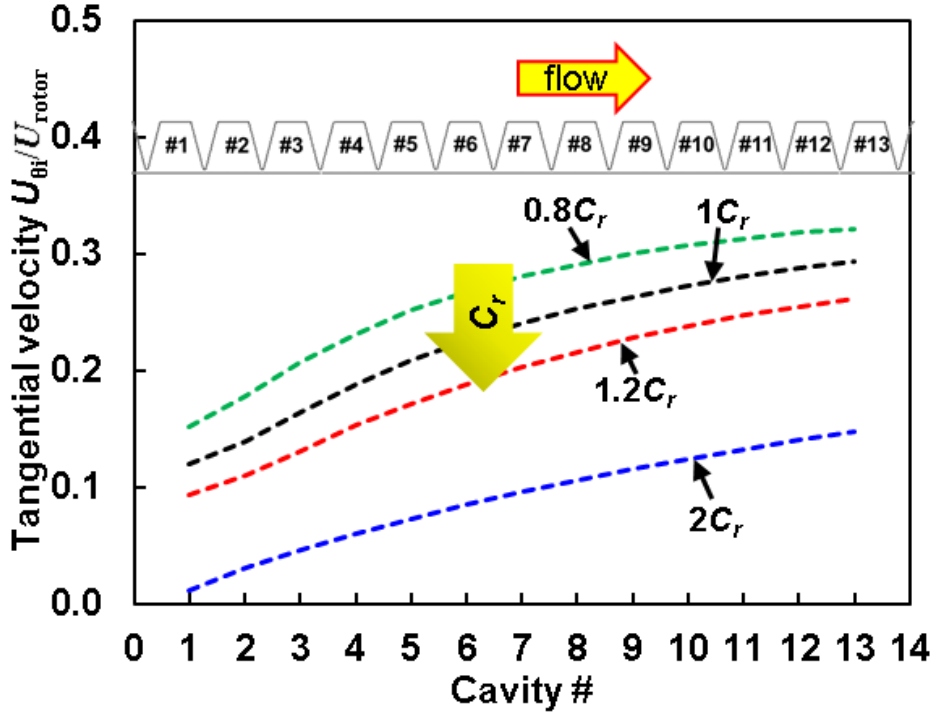

(b) U_i/U_{rotor}

Figure 13. Cavity Circumferential velocity U_i/U_{rotor} and density ρ/ρ_s vs. cavity number for four radial clearances (0.8, 1, 1.2, 2)×C_r. TOS LS: P_{in} = 7.3 MPa, P_{out} = 5.1 MPa, rotor speed = 12 krpm ($R\Omega$ = 99 m/s), α_{inlet} = 0.

Recall Eqn. (5), the relation between the wall shear stresses ($\tau_{r\theta}$, $\tau_{s\theta}$) and the wall friction factor ($f_{r\theta}$, $f_{s\theta}$). Hence, with the above flow parameters extracted from CFD results, one can derive the wall friction factor at each cavity. Figure 14 depicts $f_{r\theta}$ and $f_{s\theta}$ at operating conditions with respect to changes in radial clearance. Figure 14 (a) and (b) show the f's when the seal operates at P_{in} = 7.3 MPa and P_{out} = 5.1 MPa, while those in Figure 14 (c) and (d) are obtained at P_{in} = 10 MPa and P_{out} = 4 MPa. When the radial clearance increases from 1×C_r to 2×C_r, the 1st cavity flow circulatory motion gets stronger that causes a large pressure drop, see Figure 15. However, increasing the radial clearance to 2×C_r significantly decreases the cavity circumferential velocity (see Figure 13). Hence, for a LS with 2×C_r, the magnitude of the derived $f_{s\theta}$ near the seal entrance plane is significantly larger than in other cavities. Though the rotor surface has a larger shear stress ($\tau_{r\theta}$), considering the difference in relative tangential velocity U_{ri} and U_{si}, the CFD delivers $f_{r\theta} \ll f_{s\theta}$. Notably, the rotor surface wall friction factor ($f_{r\theta}$) remains unchanged as the radial clearance increases from 0.8×C_r to 2×C_r. On the other hand, increasing the radial clearance (C_r) promotes the growth of the stator surface friction factor ($f_{s\theta}$), a ~ 25% rise when the radial clearance changes from 0.8×C_r to 1×C_r or from 1×C_r to 1.2×C_r. Doubling the radial clearance (C_r) leads to a ~110% increase in $f_{s\theta}$.

Figure 16 shows $f_{r\theta}$ and $f_{s\theta}$ from both CFD (friction factor not cavity averaged) and the Blasius friction factor model ($f_{r\theta,s\theta} = 0.079\ Re_{r\theta,s\theta}^{-0.25}$) vs. axial length. The Blasius friction model is based on the CFD predicted cavity density (ρ) and tangential velocity (U). Note the CFD $f_{r\theta} << f_{s\theta}$ which varies slightly within a cavity. On the other hand, the CFD $f_{s\theta}$ shows a large variation within a cavity as the local velocity suddenly changes near a stator wall. The Blasius friction factor model underestimates both $f_{r\theta}$ and $f_{r\theta}$ when compared to those f's derived from CFD.

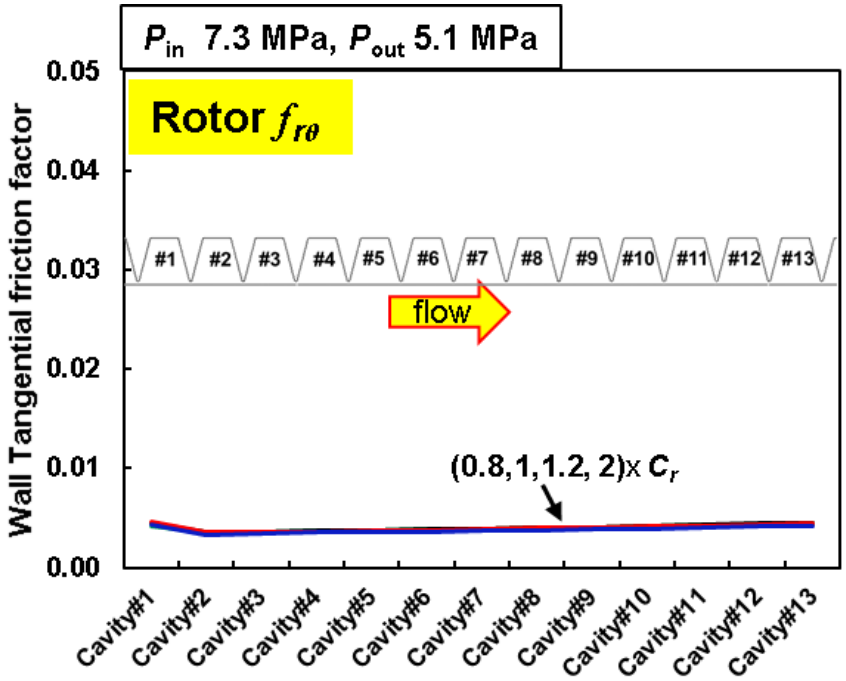

(a) $f_{r\theta}$

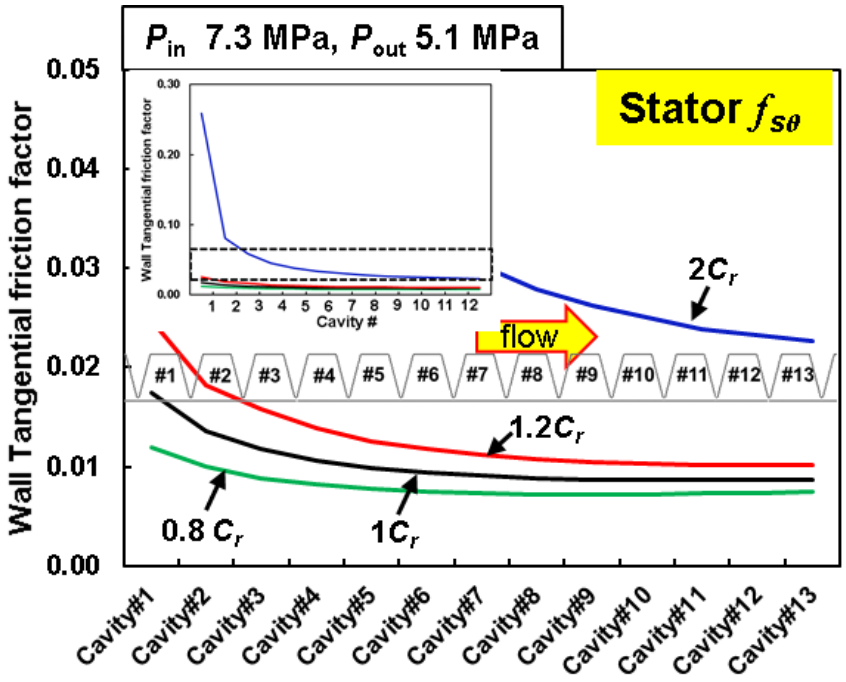

(b) $f_{s\theta}$

(continued)

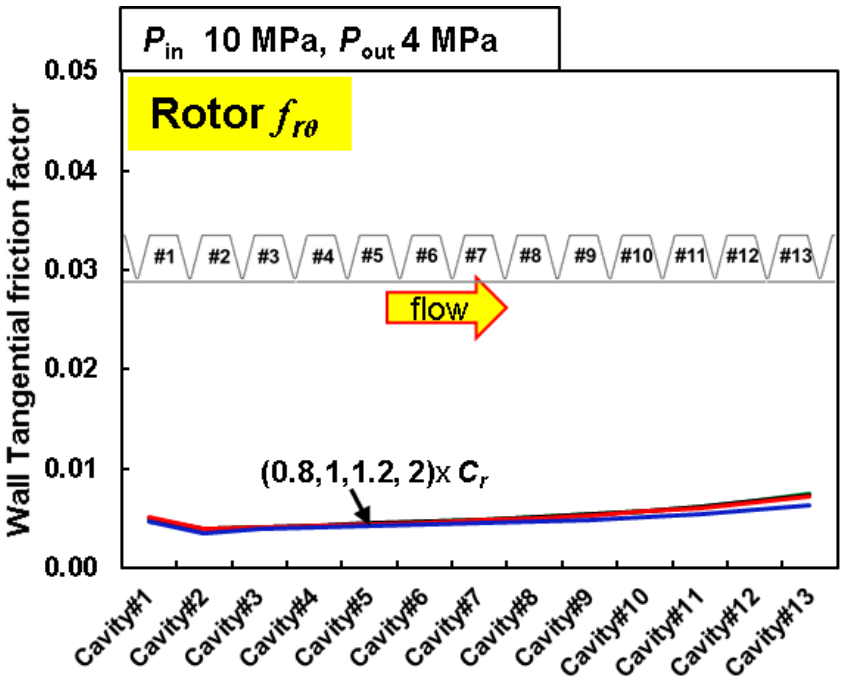

(c) $f_{r\theta}$

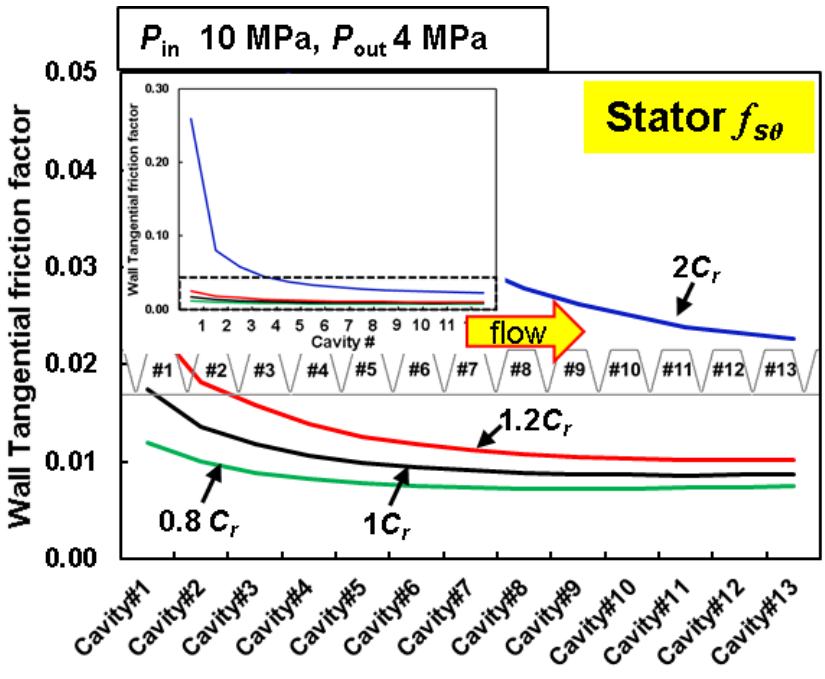

(d) $f_{s\theta}$

Figure 14. CFD derived friction factors $f_{r\theta}$, $f_{s\theta}$ vs. cavity number for four radial clearances (0.8, 1, 1.2, 2)×C_r. TOS LS: (a) and (b) P_{in} = 7.3 MPa, P_{out} = 5.1 MPa; (c) and (d) P_{in} = 10 MPa, P_{out} = 4 MPa. Rotor speed = 12 krpm ($R\Omega$ = 99 m/s), α_{inlet} = 0.

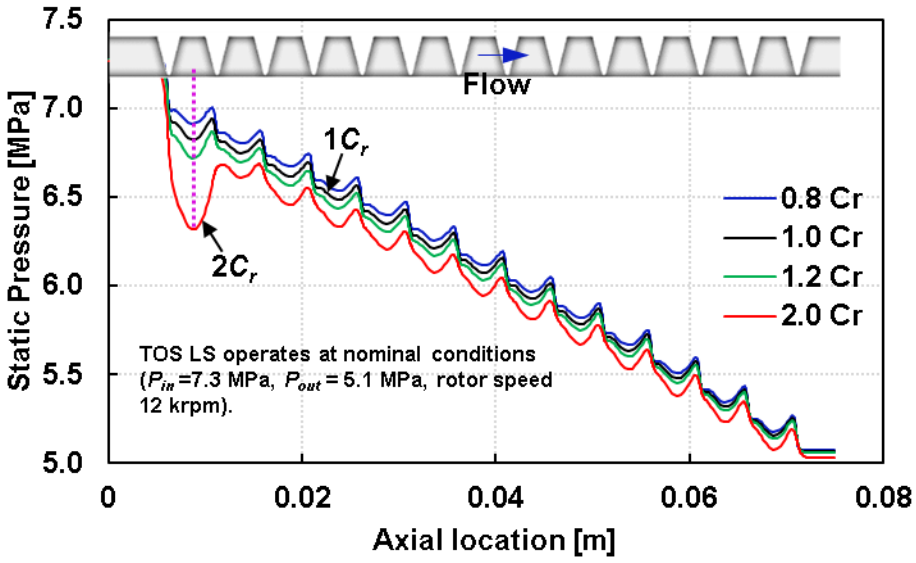

Figure 15. CFD predicted pressure along the axial direction for four radial clearances (0.8, 1, 1.2, 2)×C_r. TOS LS with P_{in} = 7.3 MPa, P_{out} = 5.1 MPa, rotor speed = 12 krpm ($R\Omega$ = 99 m/s), α_{inlet} = 0.

Please note that for all the cases herein, the curve fits of the CFD derived friction factors give $m_s = m_r = -0.25$. As listed in Table 4, the newly derived coefficient n_r is ~ twice the classical one (n = 0.079). Note the axial flow Reynolds number Re_{axial} = 7.3×10^4 ~ 2.6×10^5, and the circumferential flow Reynolds numbers at the rotor ($Re_{r\theta}$) and stator ($Re_{s\theta}$) surfaces range from 1.5×10^6 ~ 2.8×10^6 and 3.1×10^4 ~ 7.2×10^5, respectively. When C_r varies -20% to 100% of its nominal value, n_r is constant; whereas, n_s is nearly proportional to the change in C_r. The larger the $Re_{s\theta}$, the smaller n_s is. Notably, the stator surface friction factor is significantly underestimated by the classical friction factor model (n = 0.079, m = -0.25). The CFD derived coefficient n_s is thrice the typical magnitude.

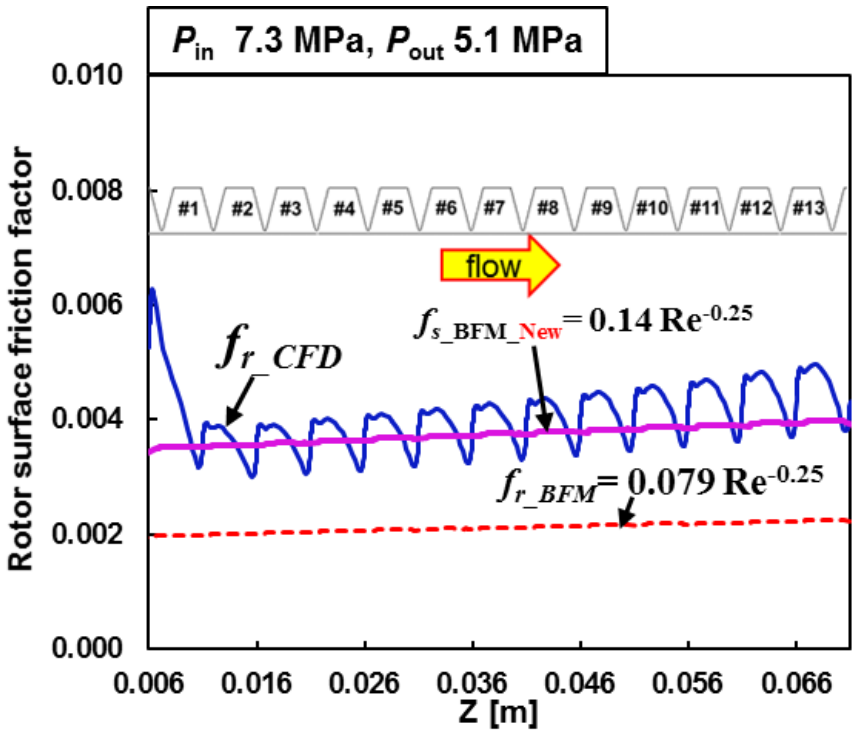

(a) $f_{r\theta}$

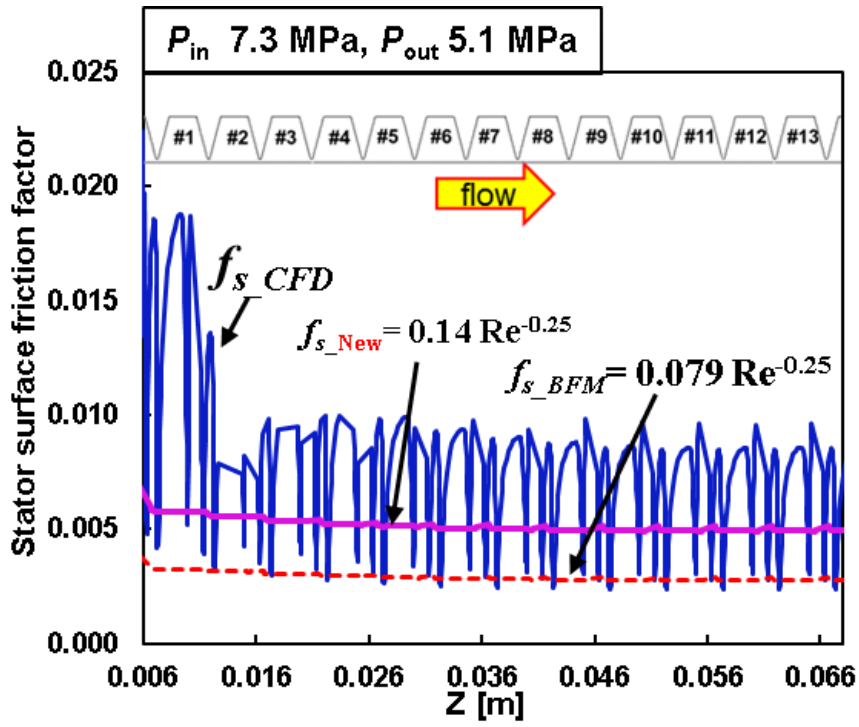

(b) $f_{s\theta}$

Figure 16. BFM derived friction factors ($f_{r\theta}$, $f_{s\theta}$) and CFD friction factor ($f_{r\theta}$, $f_{s\theta}$) vs. axial length. TOS LS (1C_f): P_{in} = 7.3 MPa, P_{out} = 5.1 MPa, rotor speed = 12 krpm ($R\Omega$ = 99 m/s), α_{inlet} = 0. f's with new (n, m) coefficients included.

Table 4. New coefficients (*n*, *m*) for Blasius friction factor model obtained from four clearances. Range of Reynolds numbers noted.

$\times C_r$	Rotor			Stator			Axial Reynolds number (Re_{axial})
	n_r	m_r	$Re_{r\theta}$	n_s	m_s	$Re_{s\theta}$	
0.8	0.14	-0.25	$1.5\times10^6 \sim 2.8\times10^6$	0.23	-0.25	$4.3\times10^5 \sim 7.2\times10^5$	$7.3\times10^4 \sim 2.6\times10^5$
1	0.14			0.28		$3.3\times10^5 \sim 6.4\times10^5$	
1.2	0.14			0.35		$2.7\times10^5 \sim 5.7\times10^5$	
2	0.14			0.59		$3.1\times10^4 \sim 3.3\times10^5$	

5.2 Effect of Rotor Speed (Ω) on Friction Factor f_θ

Figure 17 shows the wall shear stresses $\tau_{r\theta}$ and $\tau_{s\theta}$ for operation at four rotor speeds ($R\Omega$ = 58 m/s to 173 m/s, Re_r = 6.6 ×10^5 to 3.1 ×10^6, and Re_s = 1.2 ×10^5 to 6.4 ×10^5). The radial clearance is set as 1C_r. Rotor speed enhances both $\tau_{r\theta}$ and $\tau_{s\theta}$. On the other hand, $\tau_{r\theta} \gg \tau_{s\theta}$ due to a higher shear drag on the rotor surface. Figure 17 (c) shows $\tau_{r\theta}/(R\Omega)$, the rotor tangential wall shear stress per unit circumferential velocity presents a negligible change with respect to an increase in rotor speed Ω (except in the region close to the seal entrance).

Figure 18 depicts the cavity circumferential velocity $U_i/(R\Omega)$ and density (ρ_i/ρ_s). The circumferential velocity increases with rotor speed, whereas the cavity density (or pressure) retains the same magnitude regardless of a rotor speed change, see Figure 18 (b). This shows rotor speed does not affect LS leakage, as is well known.

Recall the wall friction factors ($f_{r\theta} = 2\tau_{r\theta} \big/ \rho(U - R\Omega)^2$, $f_{s\theta} = 2\tau_{s\theta} \big/ \rho U^2$) are functions of the wall shear stress and cavity relative velocity. The increase in rotor speed promotes both $\tau_{r\theta}$ and $\tau_{s\theta}$ and U_i. Thus, Figure 19 demonstrates the effect of rotor speed on the wall friction factors $f_{r\theta}$ and $f_{s\theta}$. One should notice the scale difference as $f_{r\theta} \ll f_{s\theta}$. The CFD predicted $f_{r\theta}$ and $f_{s\theta}$ decrease with respect to an increase in rotor speed, and so do too $f_{r\theta}/(R\Omega)$ and $f_{s\theta}/(R\Omega)$.

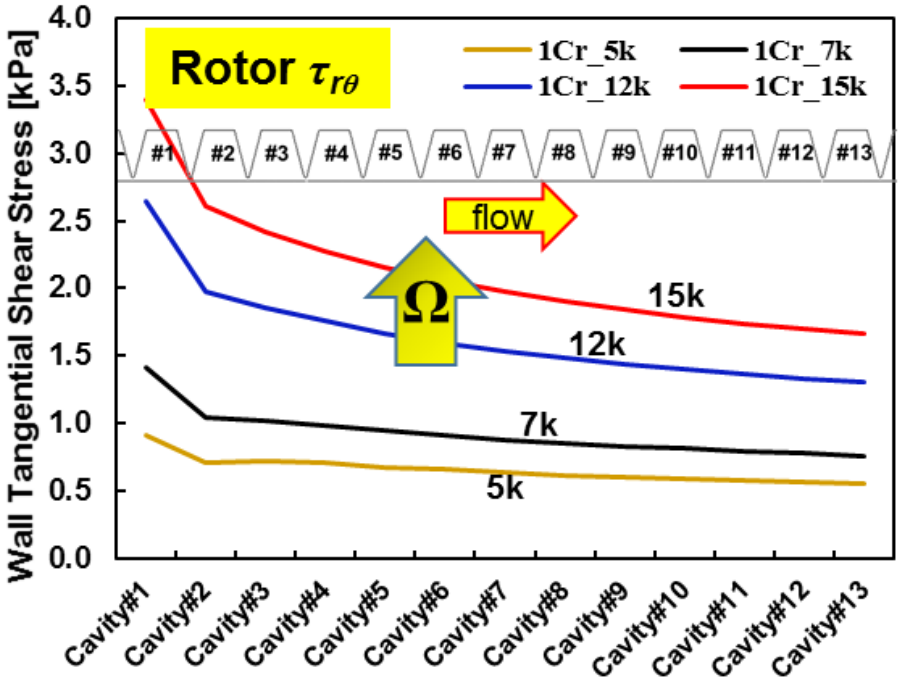

(a) $\tau_{r\theta}$

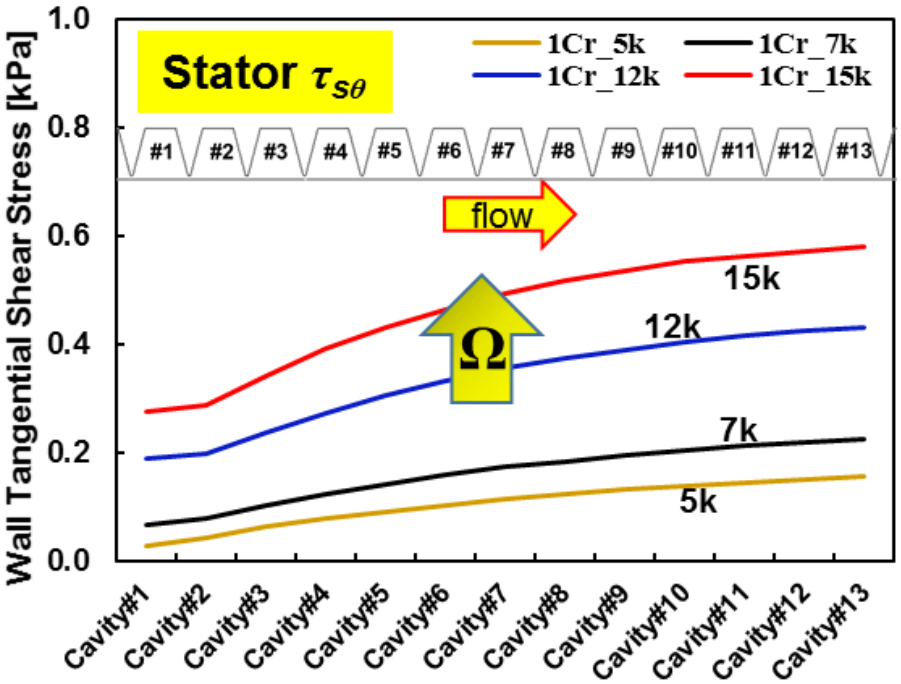

(b) $\tau_{s\theta}$

(continued)

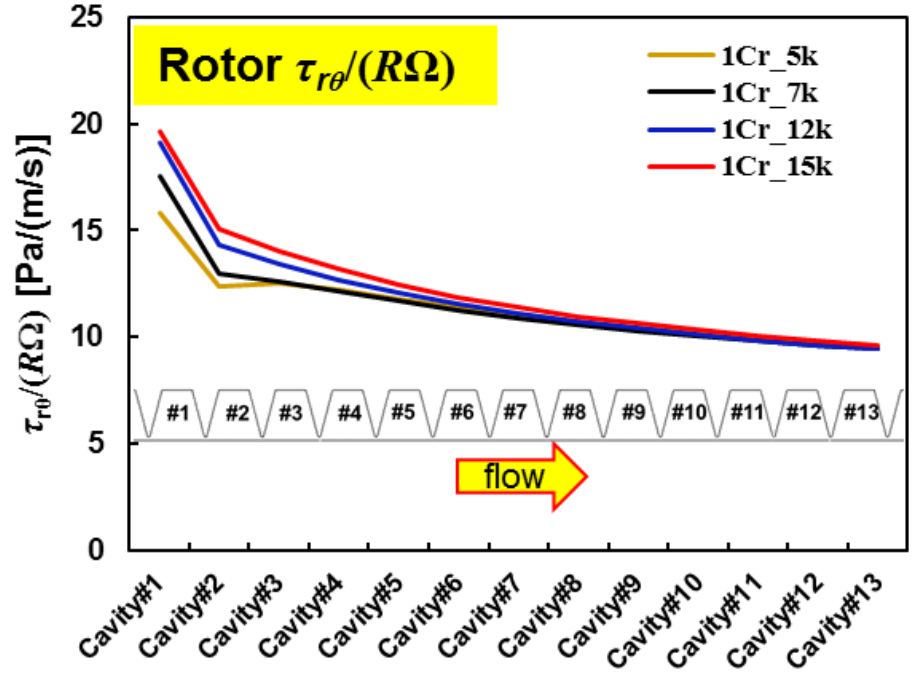

(c) $\tau_{r\theta}/(R\Omega)$

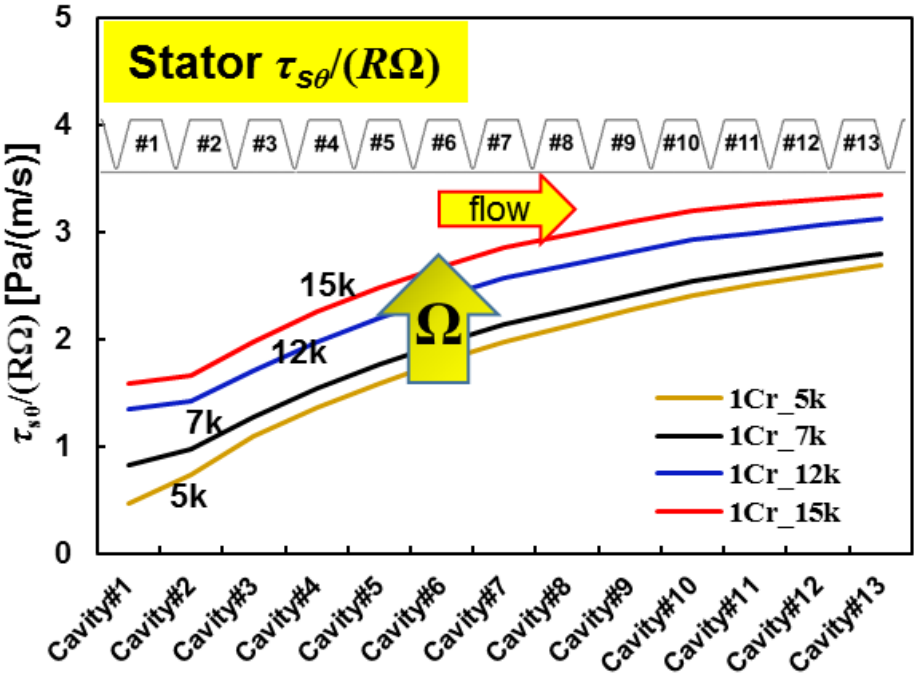

(d) $\tau_{s\theta}/(R\Omega)$

Figure 17. Wall shear stresses $\tau_{r\theta}$ and $\tau_{s\theta}$ vs. cavity number for operation at four rotor speeds Ω = (5, 7, 12, 15)×krpm: (a) rotor surface $\tau_{r\theta}$; (b) stator surface $\tau_{s\theta}$; (c) rotor surface $\tau_{r\theta}/(R\Omega)$; (d) stator surface $\tau_{s\theta}/(R\Omega)$. TOS LS (1C_r): P_{in} = 7.3 MPa, P_{out} = 5.1 MPa.

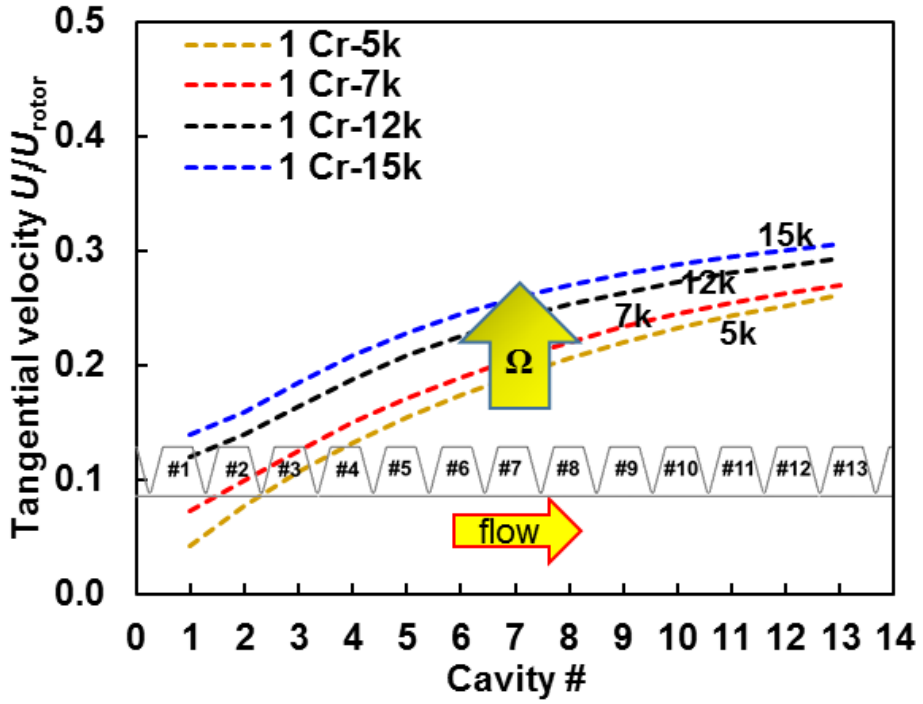

(a) U_i/U_{rotor}

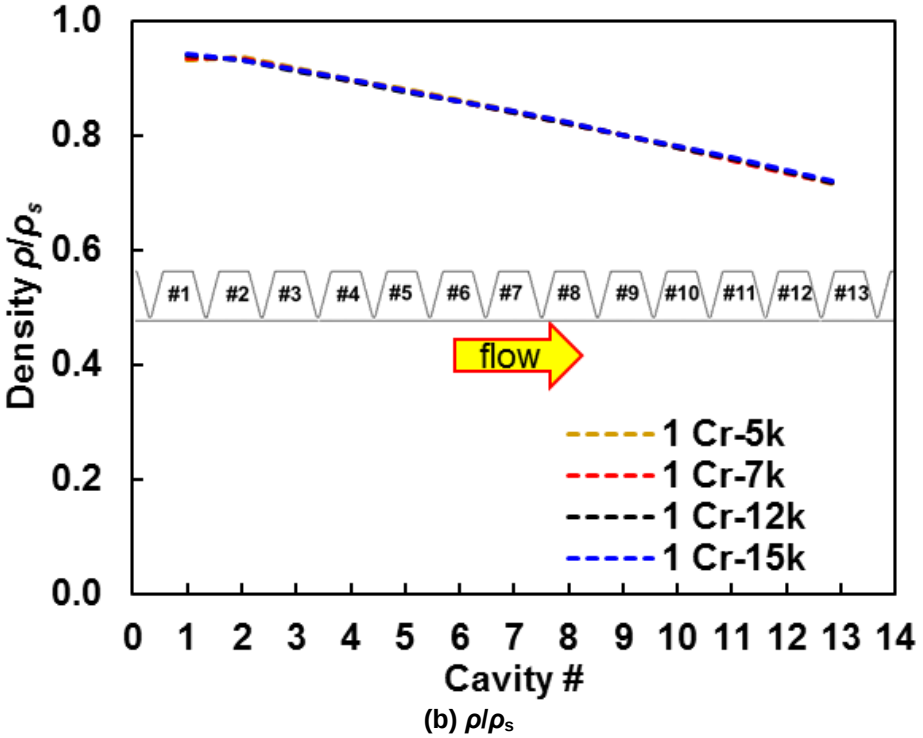

(b) ρ/ρ_s

Figure 18. Seal circumferential velocity U_i/U_{rotor} and density ρ/ρ_s vs. cavity number for operation at four rotor speeds Ω = (5, 7, 12, 15)×krpm. TOS LS: P_{in} = 7.3 MPa, P_{out} = 5.1 MPa.

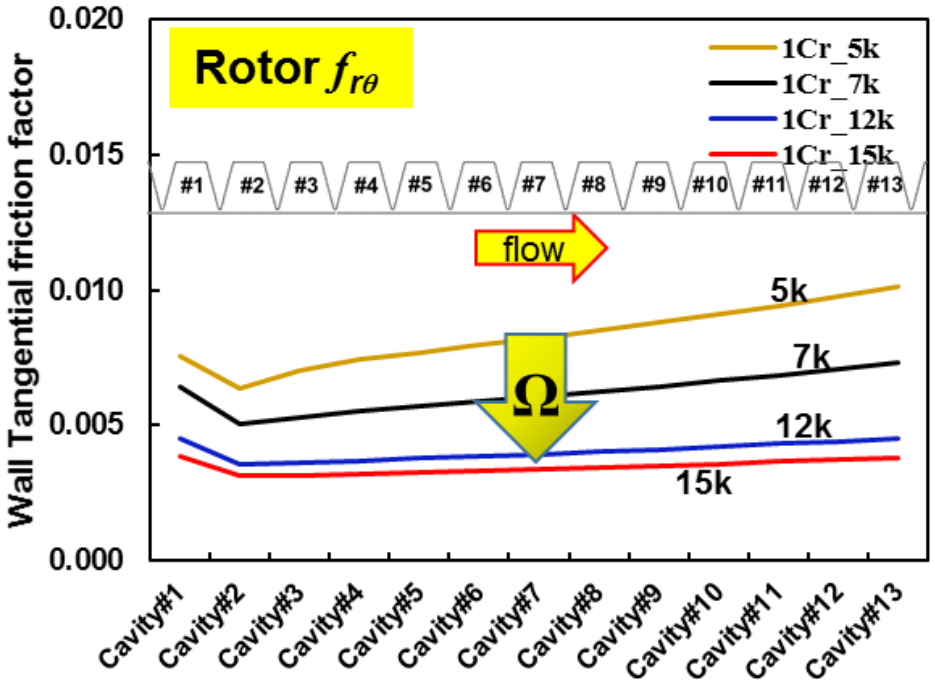

(a) $f_{r\theta}$

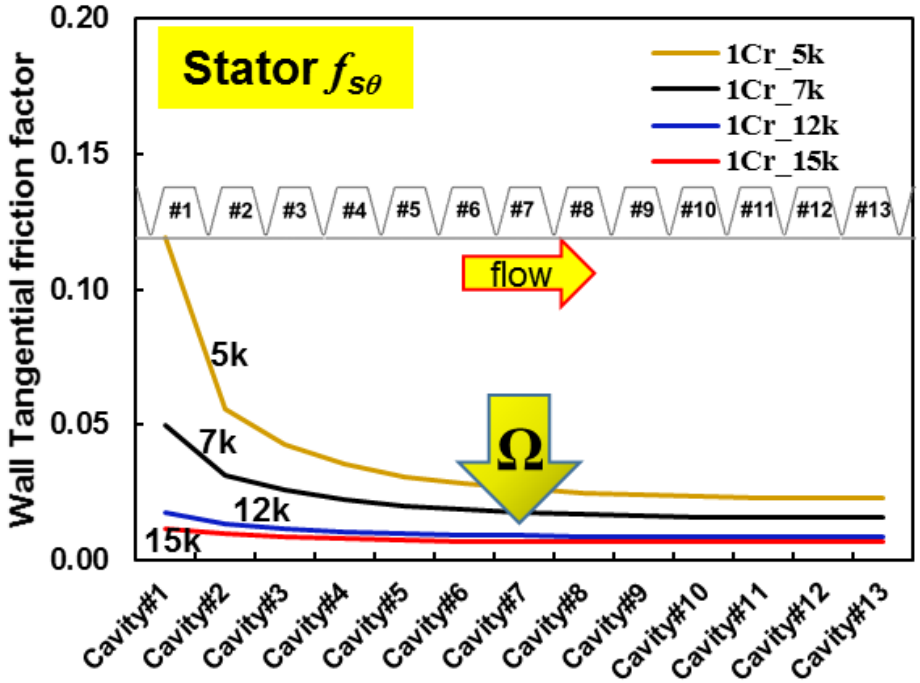

(b) $f_{s\theta}$

(continued)

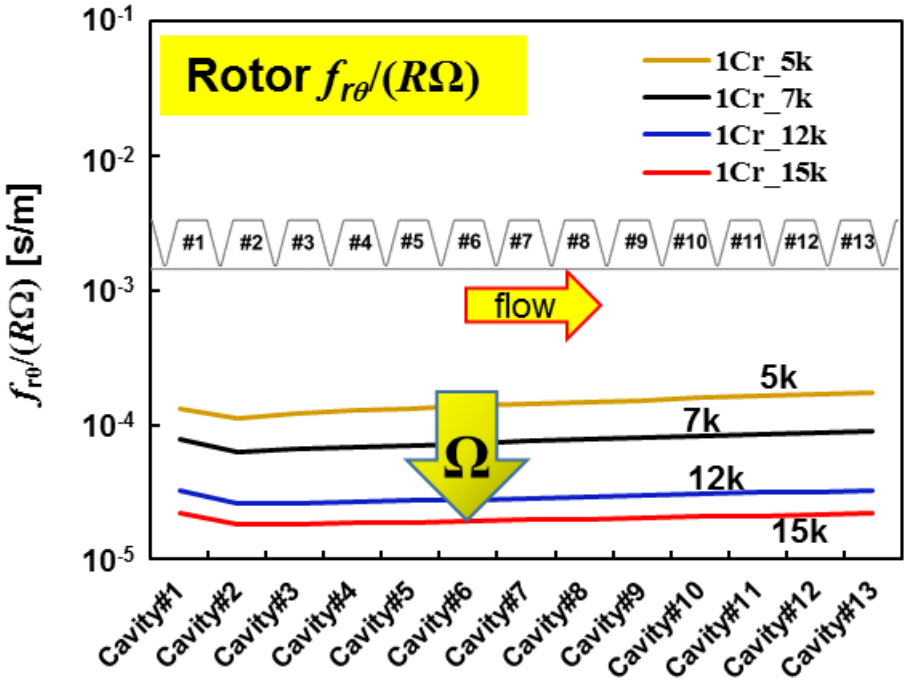

(c) $f_{r\theta}/(R\Omega)$

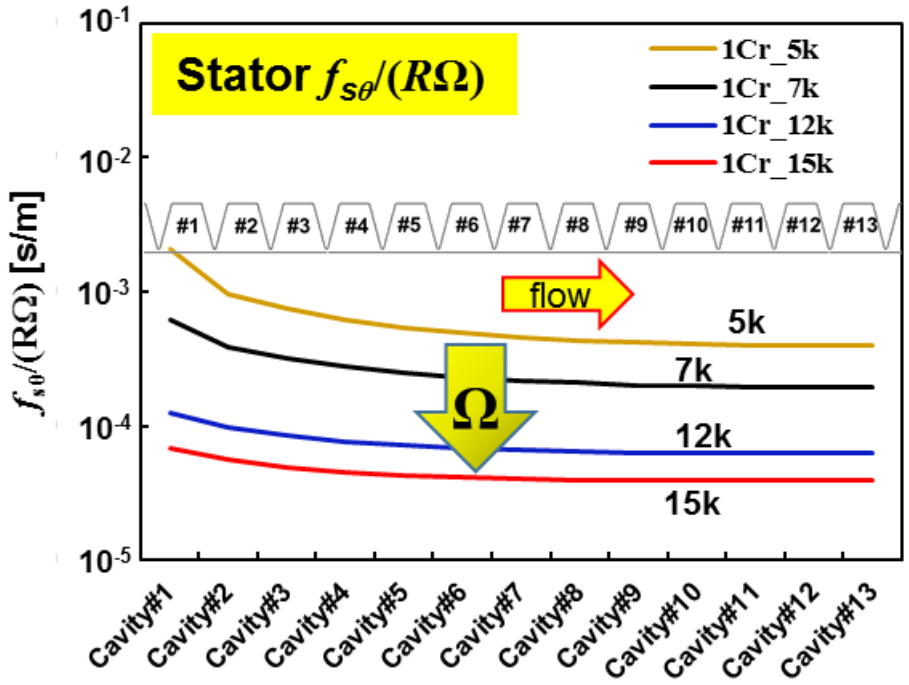

(d) $f_{s\theta}/(R\Omega)$

Figure 19. Friction factors ($f_{r\theta}$, $f_{s\theta}$,) and ($f_{r\theta}$, $f_{s\theta}$)/($R\Omega$) vs. cavity number for operation at four rotor speeds Ω = (5, 7, 12, 15)×krpm. TOS LS (1C$_r$): P_{in} = 7.3 MPa, P_{out} = 5.1 MPa.

Table 5 lists the new friction factor coefficients (n, m) for four rotor speeds. The CFD obtained friction factor coefficients (n, m) are quite large (up to 9 times) than the classical ones (n = 0.079, m = -0.25), particularly when the seal operates at a low rotor speed.

Table 5. New friction factor coefficients (n, m) obtained for four rotor speeds.

Ω (krpm)	RΩ (m/s)	n_r	m_r	n_s	m_s
5	58	0.25	-0.25	0.70	-0.25
7	81	0.20		0.48	
12	138	0.14		0.28	
15	173	0.13		0.23	

5.3 Effect of Pressure Ratio ($PR = P_{out}/P_{in}$) on Friction Factor f_θ

The pressure ratio $PR = (P_{out}/P_{in})$ is a critical parameter for LS leakage and rotordynamic force coefficients. Figure 20 depicts rotor and stator wall shear stresses, $\tau_{r\theta}$ and $\tau_{s\theta}$, for various supply pressures (in the legend, P stands for the supply pressure in bar). Changes in the supply pressure P_{in} and the discharge pressure P_{out} establish pressure ratios ranging from 0.4 to 0.85. As Figure 20 shows, when the supply pressure P_{in} is fixed, the wall shear stresses ($\tau_{r\theta}$, $\tau_{s\theta}$) decrease with respect to an increase in the pressure ratio PR (or the discharge pressure P_{out}). On the other hand, when PR is fixed, an increase in the supply pressure results in larger wall shear stresses $\tau_{r\theta}$ and $\tau_{s\theta}$.

Figure 21 (a) shows the average cavity circumferential velocity $U_i/(R\Omega)$ and density (ρ_i/ρ_s) vs. cavity number for various pressure ratios, PR. As the PR increases from 0.40 to 0.85, both the cavity circumferential velocity $U_i/(R\Omega)$ and density ρ_i/ρ_s increase. Notably, when the pressure ratio (PR) is fixed, the circumferential velocity $U_i/(R\Omega)$ as well as (ρ_i/ρ_s) remains the same regardless of the changes in the supply or discharge pressure (P_{in} or P_{out}). On the other hand, as the cavity density ρ_i is a function of the local pressure, (ρ_i/ρ_s) increases with a larger discharge pressure (larger PR), see Figure 21 (b).

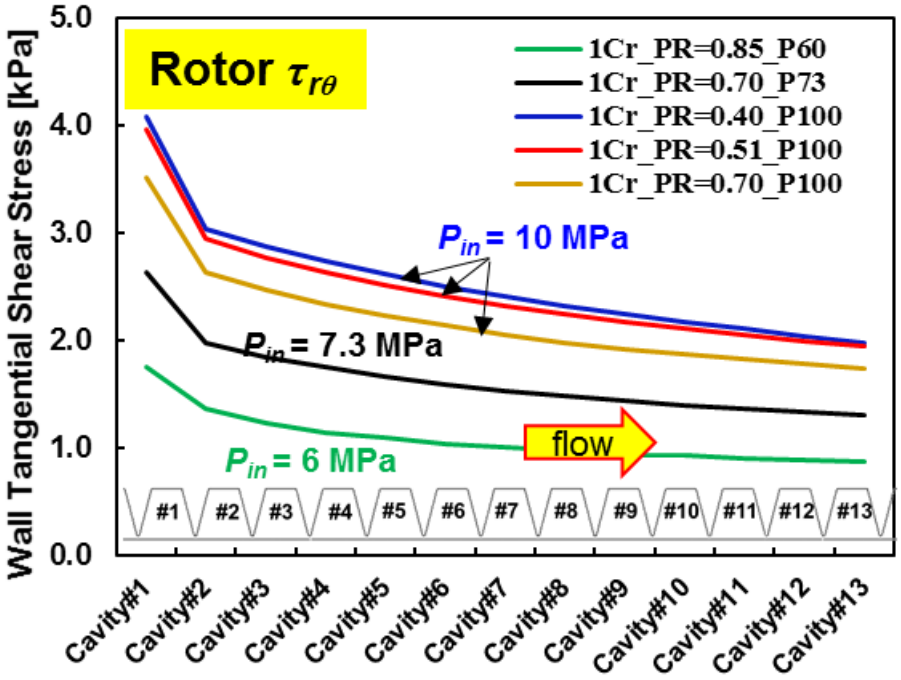

(a) $\tau_{r\theta}$

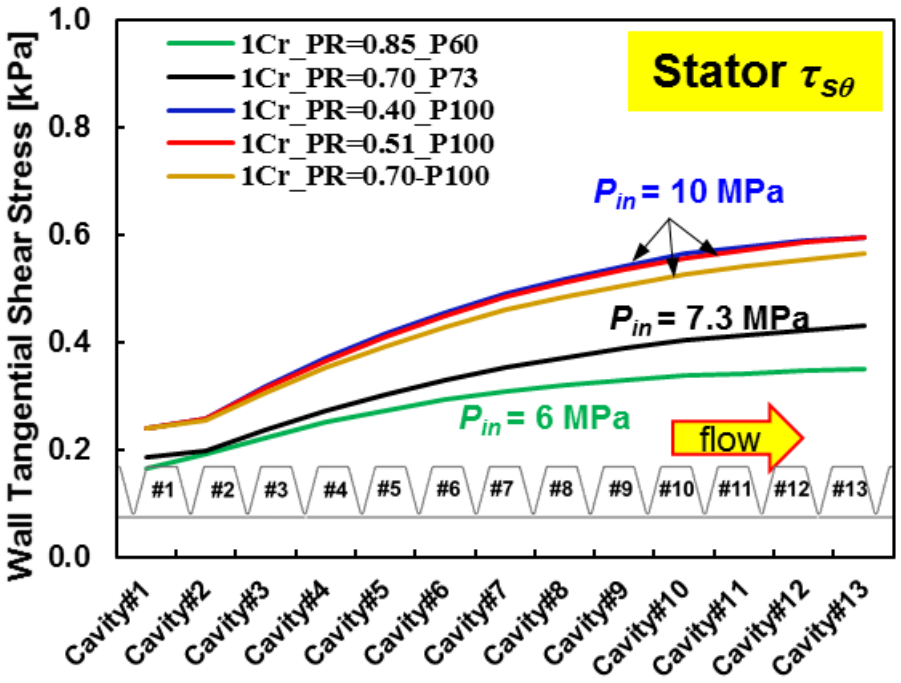

(b) $\tau_{s\theta}$

Figure 20. Wall shear stresses $\tau_{r\theta}$ and $\tau_{s\theta}$ vs. cavity number for operation at four pressure ratios *PR* = 0.40-0.85. TOS LS (1C$_r$): rotor speed = 12 krpm, P_{in} and P_{out} vary.

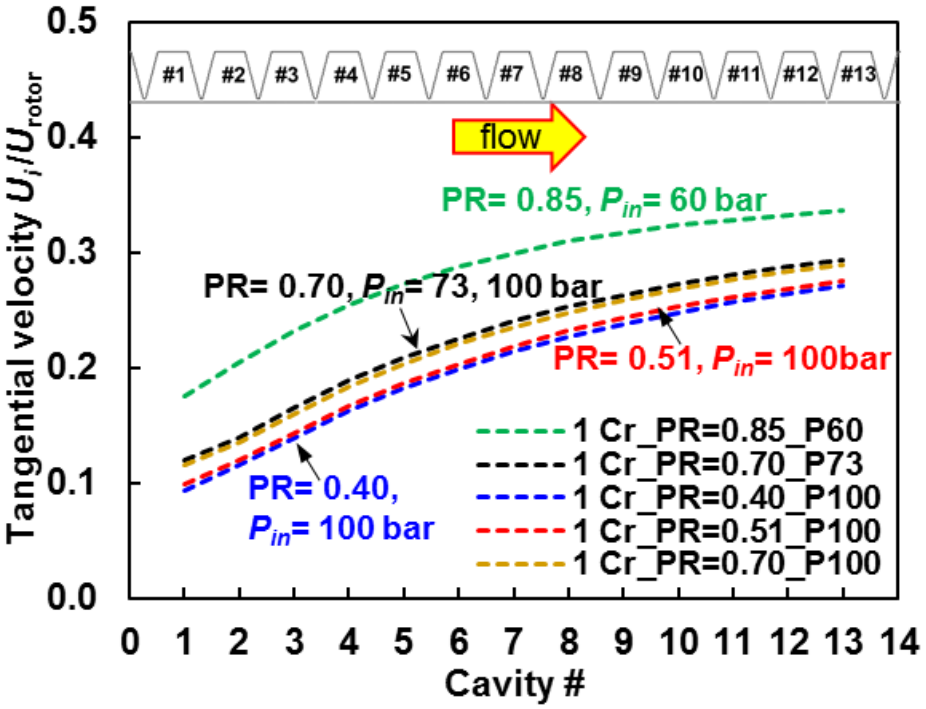

(a) U_i/U_{rotor}

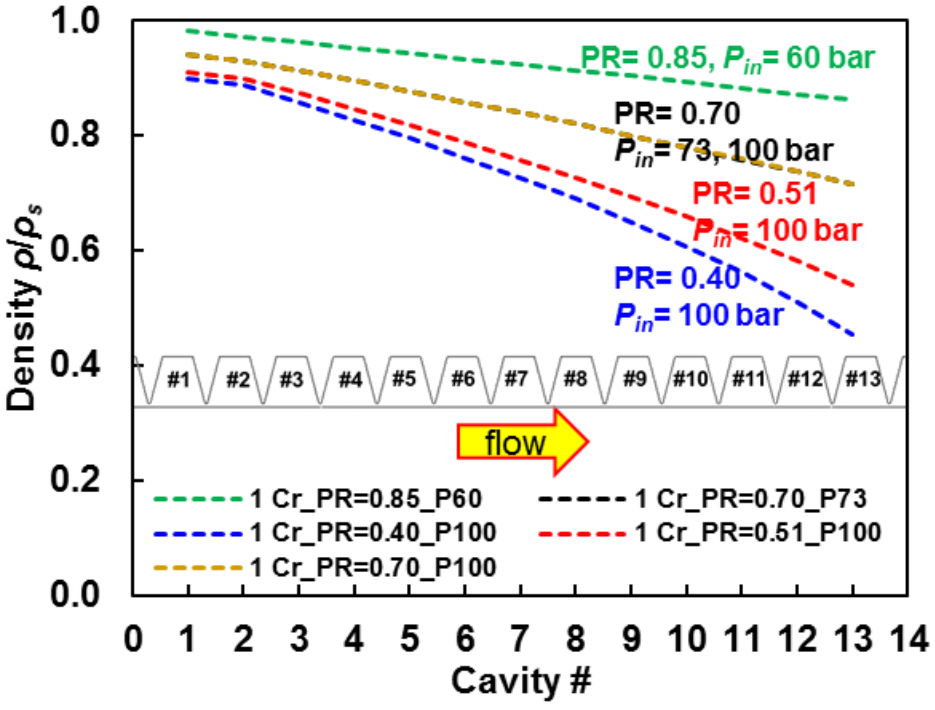

(b) ρ/ρ_s

Figure 21. Circumferential velocity U_i/U_{rotor} and density ρ/ρ_s vs. cavity number for operation at four pressure ratios *PR* = 0.40-0.85. TOS LS: rotor speed = 12 krpm, P_{in} and P_{out} vary.

Figure 22 shows the rotor and stator circumferential friction factors, $f_{r\theta}$ and $f_{s\theta}$, for distinct variations in pressure ratios (*PR*). As the supply pressure P_{in} increases from 6.3 MPa (63 bar) to 10 MPa (100 bar), and the discharge pressure varies from 4 MPa to 7 MPa, the pressure ratio *PR* ranges from 0.40 to 0.85. CFD results indicate that the friction factors ($f_{r\theta}$, $f_{s\theta}$) are sensitive to an increase in *PR*. An increase in *PR* results in a lower circumferential friction factor for both the rotor and the stator surfaces. When the pressure ratio (*PR*) is fixed, the friction factors ($f_{r\theta}$ and $f_{s\theta}$) remain the same regardless of the variations in the supply or discharge pressure (P_{in} or P_{out}). Table 6 lists the new friction factor coefficients (*n*, *m*) for four pressure ratios.

The CFD obtained friction factor coefficients (*n*, *m*) are larger than those of the classical model (*n* = 0.079, *m* = -0.25), particularly on the stator surface. At a low pressure ratio condition, the CFD predicted *f* is up to 5 times higher than the classical Blasius *f* estimation.

Table 6. New friction factor coefficients (*n*, *m*) obtained for four pressure ratios.

PR	P_{in} (bar)	n_r	m_r	n_s	m_s
0.40	100	0.20	-0.25	0.43	-0.25
0.51	100	0.18		0.38	
0.70	73, 100	0.14		0.28	
0.85	60	0.12		0.17	

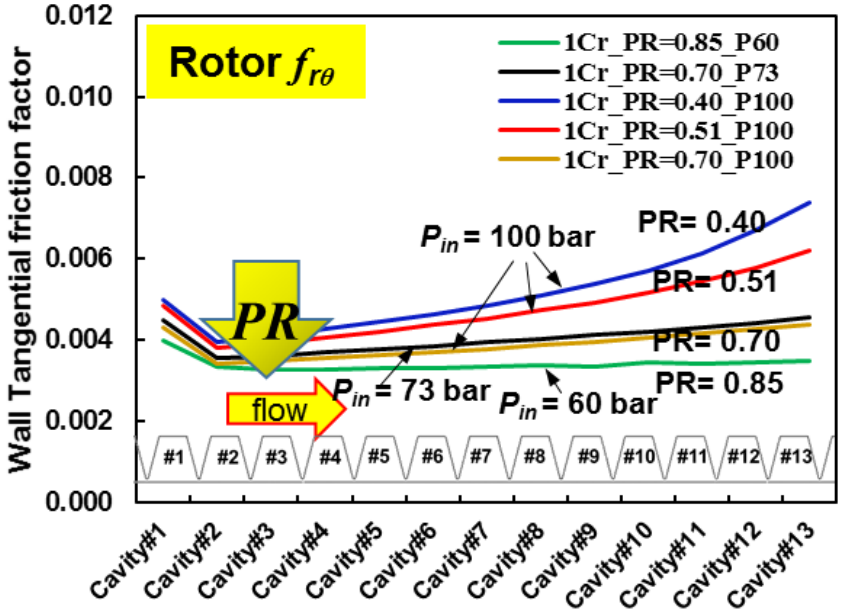

(a) $f_{r\theta}$

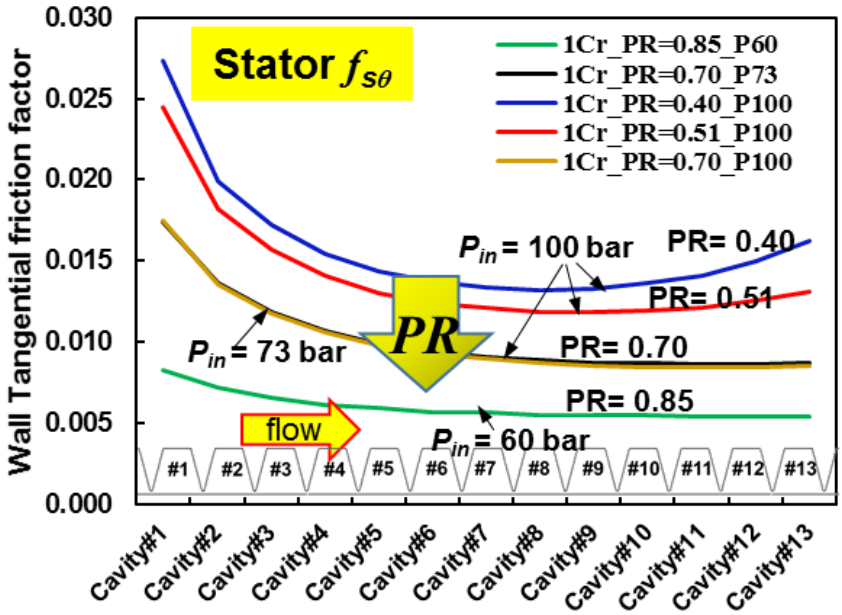

(b) $f_{s\theta}$

Figure 22. Friction factors $f_{r\theta}$ and $f_{s\theta}$ vs. cavity number for operation at four pressure ratios *PR* = 0.40-0.85. TOS LS (1C$_r$): rotor speed = 12 krpm, P_{in} and P_{out} vary.

5.4 Effect of Pre-Swirl Velocity Ratio ($\alpha = U_0/R\Omega$) on Friction Factor f_θ

Prior research has evidenced that the inlet pre-swirl velocity ratio $\alpha = U_0/(R\Omega)$ has a significant impact on the cross-coupled stiffness of a labyrinth seal. Figure 23 and Figure 24 illustrate the effect of the inlet pre-swirl velocity ratio (α) on the wall shear stresses $\tau_{r\theta}$ and $\tau_{s\theta}$, the cavity circumferential velocity $U_i/(R\Omega)$, and the cavity density (ρ_i/ρ_s). With an increase in α, the difference between $\tau_{r\theta}$ and $\tau_{s\theta}$ becomes smaller and smaller. Generally, when the pre-swirl ratio (α) increases, the rotor wall shear stress $\tau_{r\theta}$ decreases, and the stator wall shear stress $\tau_{s\theta}$ increases. As expected, a larger pre-swirl velocity promotes a larger cavity average circumferential velocity, see Figure 24(a). As Figure 24(b) depicts, the CFD results show a negligible impact of the circumferential pre-swirl velocity on the seal cavity density (or pressure) distribution.

Figure 25 depicts the wall friction factors $f_{r\theta}$ and $f_{s\theta}$ for four pre-swirl ratios (α). Interestingly, the rotor wall friction factor $f_{r\theta}$ is quite similar for operation with pre-swirl ratios (α) ranging from 0.42 to 0.72. On the other hand, the stator surface friction factor $f_{s\theta}$ decreases as α increases from 0.42 to 0.72.

Table 7 lists the new friction factor coefficients (n, m) obtained for four inlet pre-swirl ratios. The CFD obtained friction factor coefficients n_r is about 2 times of the classical one (n = 0.079); on the other hand, when operated at a low inlet pre-swirl ratio, n_s is about 2.5 times of the value (n = 0.079) used in a classical Blasius friction model. Notable, when increasing the inlet pre-swirl ratio (α), the CFD obtained n_r remains constant, while n_s decreases with α.

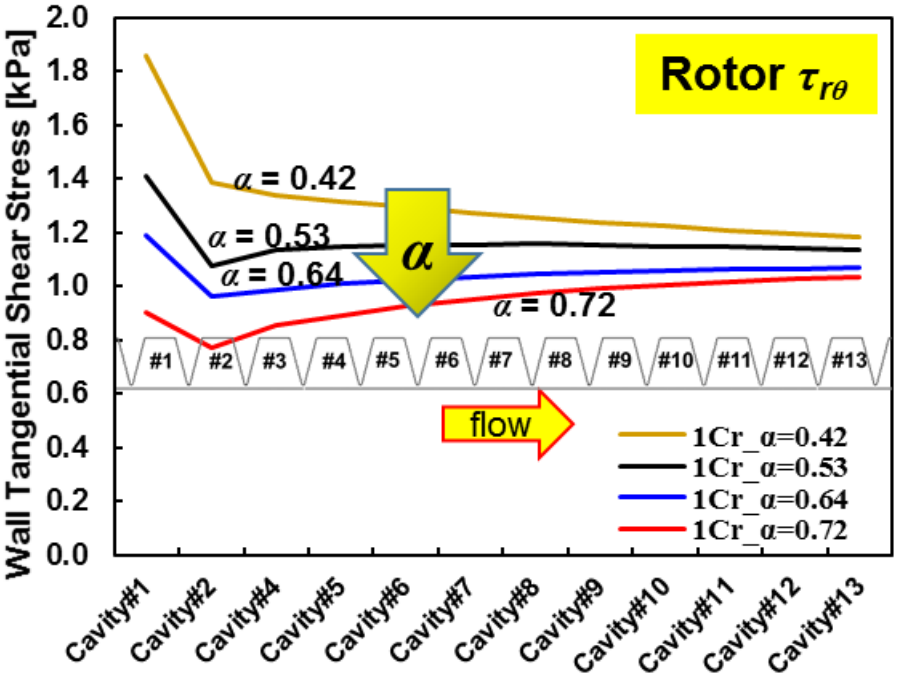

(a) $\tau_{r\theta}$

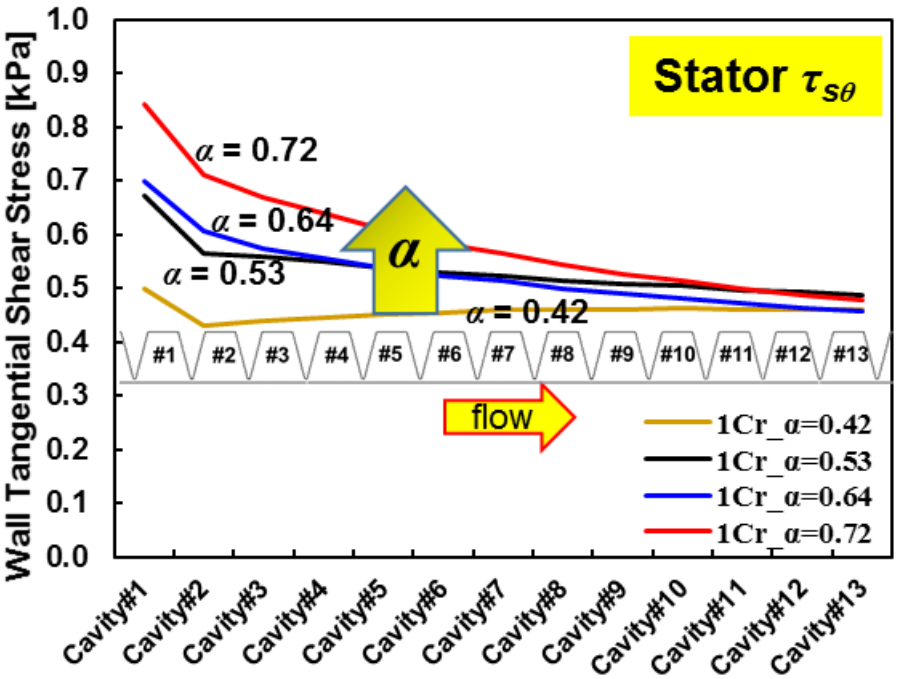

(b) $\tau_{s\theta}$

Figure 23. Circumferential wall shear stresses $\tau_{r\theta}$ and $\tau_{s\theta}$ vs. cavity number for operation at four inlet pre-swirl ratios α = 0.42-0.72. TOS LS (1C$_r$): P_{in} = 7.3 MPa, P_{out} = 5.1 MPa, rotor speed = 12 krpm.

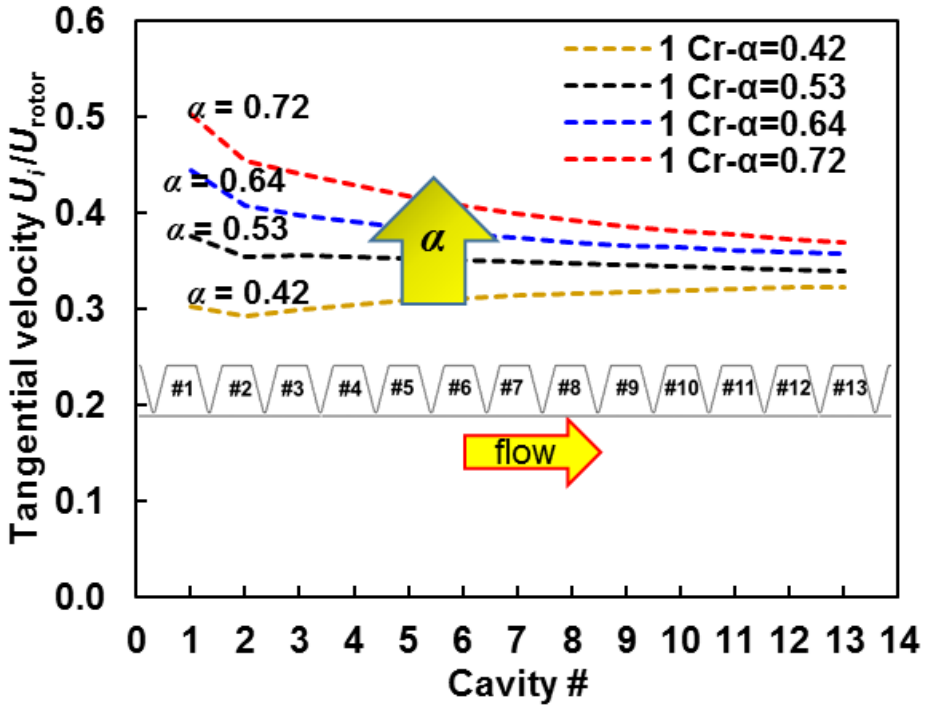

(a) U_i/U_{rotor}

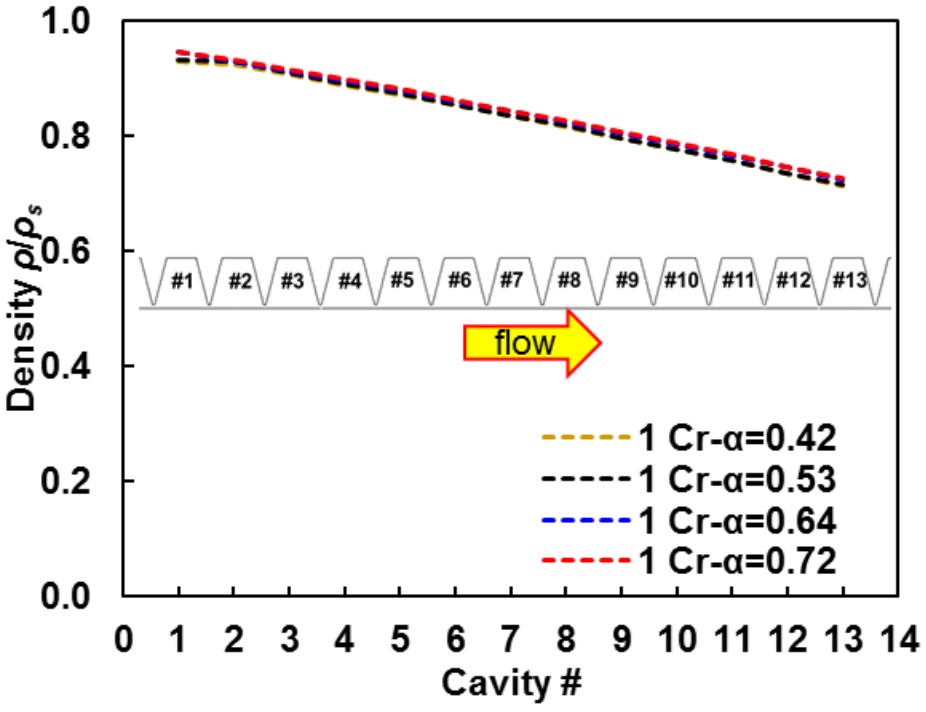

(b) ρ/ρ_s

Figure 24. Circumferential velocity U_i/U_{rotor} and density ρ/ρ_s vs. cavity number for operation at four inlet pre-swirl ratios α = 0.42-0.72. TOS LS (1C$_r$): P_{in} = 7.3 MPa, P_{out} = 5.1 MPa, rotor speed = 12 krpm.

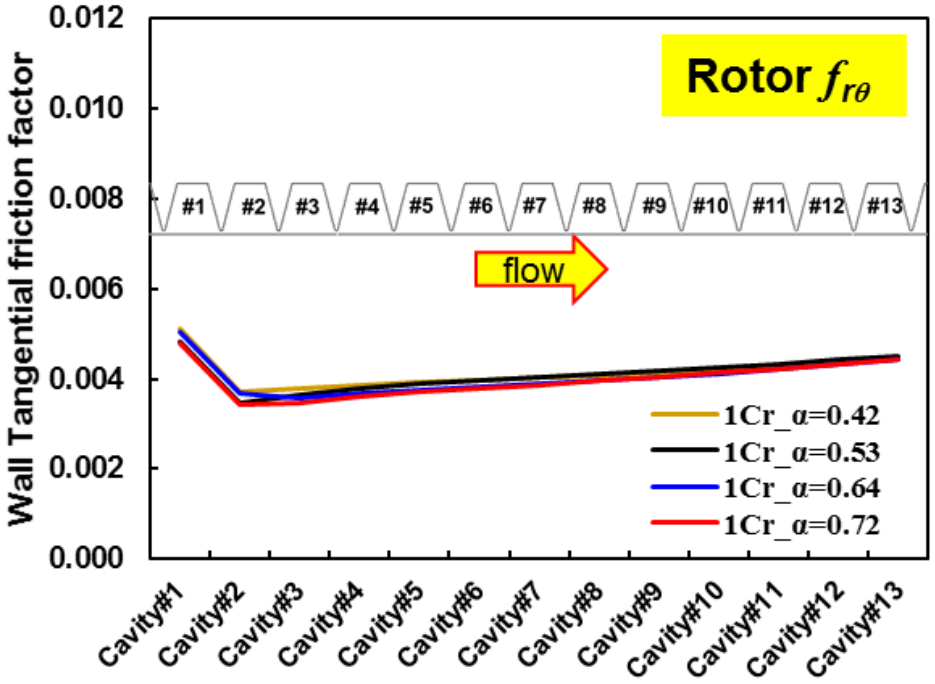

(a) $f_{r\theta}$

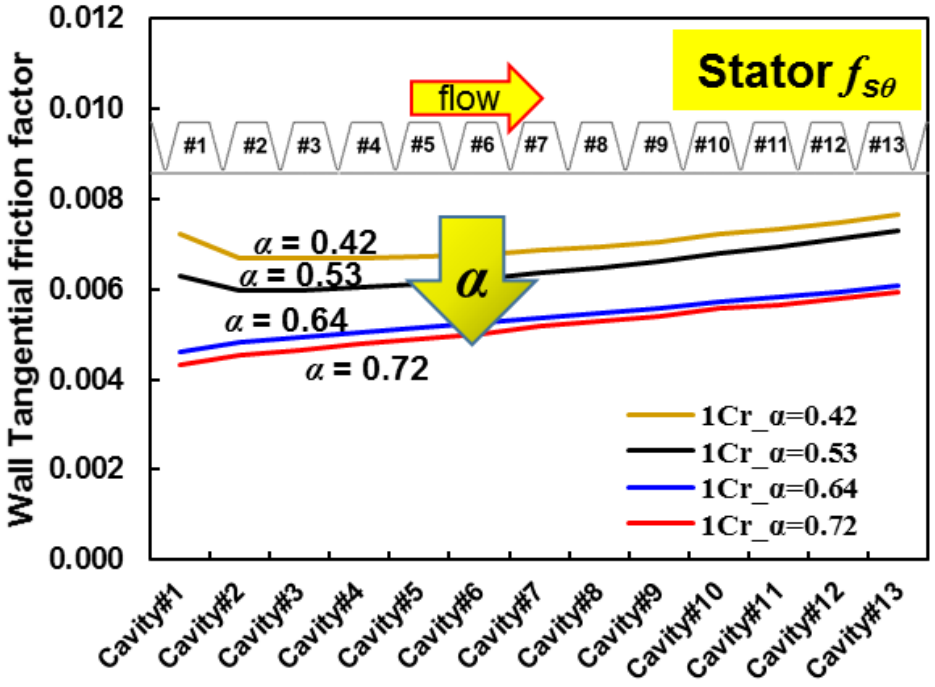

(b) $f_{s\theta}$

Figure 25. Friction factor $f_{r\theta}$ and $f_{s\theta}$ vs. cavity number for operation at four inlet pre-swirl ratios α = 0.42-0.72. TOS LS (1C$_r$): P_{in} = 7.3 MPa, P_{out} = 5.1 MPa, rotor speed = 12 krpm.

Table 7. New friction factor coefficients (*n*, *m*) obtained for four inlet circumferential velocity ratios (*α*).

α	n_r	m_r	n_s	m_s
0.42	0.14	-0.25	0.20	-0.25
0.53			0.19	
0.64			0.17	
0.72			0.16	
Classical	0.079	-0.25	0.079	-0.25

5.5 Summary

This section presents a CFD analysis of a TOS LS to quantify the effect of seal clearance and operating conditions on the wall surface friction factors ($f_{r\theta}$, $f_{s\theta}$). Based on a TOS LS presented by Vannini et al. [59] and tested in 2014, the radial clearance varies from 0.8 C_r (0.24 mm) to 2.0 C_r (0.6 mm), and the rotor speed increases from 5 krpm to 15 krpm ($R\Omega$ = 58 ~173 m/s). The supply pressure ranges from 60 bar to 100 bar, and the pressure ratio PR varies from 0.40 to 0.85. In addition, the inlet pre-swirl velocity ratio $\alpha = U_0/(R\Omega) = 0.42\sim0.72$.

The CFD predictions show the traditional Blasius friction factor model underestimates the friction factors on both rotor and stator surfaces. The rotor surface friction factor $f_{r\theta}$ is independent of changes (-20% ~ +100%) in clearance (C_r) or the inlet presiwrl ratio (α); whereas an increase in rotor speed (Ω) or pressure ratio (PR) decreases $f_{r\theta}$. On the other hand, an increase in rotor speed (Ω), pressure ratio (PR) and inlet preswirl ratio decreases $f_{s\theta}$, the stator friction factor. Besides, $f_{s\theta}$ increases with an increase in radial clearance (C_r). CFD predictions show that $f_{r\theta}$ and $f_{s\theta}$ are only sensitive to the pressure ratio, but not to the magnitude of the supply pressure or discharge pressure.

The CFD predictions deliver a set of new coefficients (n, m) for the friction factor $f=nRe^m$ and affected by changes in tip clearance and operating conditions. The CFD (n, m)'s are larger than those from the classical formula, n = 0.79, m = -0.25. Hence denoting the classical f model under

estimates the rotor and stator wall friction factors. A forthcoming multivariable analysis will later deliver more adequate correlations with (n,m) as functions of the considered parameters.

Later, an updated friction factor model, considering the multiple variables discussed above, will be derived and embeded into the BFM to improve its accuracy to predict the evolution of the circumerential flow velocity and the seal rotordynamic force coefficients, the cross-coupled stiffness in particular.

5.6 Derived Friction Factor Model

5.6.1 Rotor Surface Friction Factor $f_{r\theta}$

The above analysis shows that the friction factor on the rotor surface ($f_{r\theta}$) is fairly independent of the radial clearance (C_r) and the inlet pre-swirl velocity (U_0). On the other hand, $f_{r\theta}$ varies with respect to both rotor surface speed $R\Omega$ and the pressure ratio PR. One should note that the effect of rotor surface speed ($R\Omega$) could be expressed in terms of the stator circumferential Reynolds number $\mathrm{Re}_{r\theta} = \rho D_h (U - R\Omega)/\mu$.

Shown in Figure 26, the labyrinth seal radial clearance varies from (0.8×) to (2.0×) C_r, for a fixed PR = 0.7, the rotor surface friction factor ($f = n\,\mathrm{Re}^m$) coefficient $n_{r\theta}$ decreases with an increase in rotor surface speed ($R\Omega$). The supply pressure P_{in} varies from 60 ~ 100 bar, while the discharge pressure P_{out} = 40 ~ 70 bar, thus creating a pressure ratio PR = 0.4 ~ 0.9. The rotor surface circumferential friction factor $n_{r\theta}$ decreases with an increase in PR.

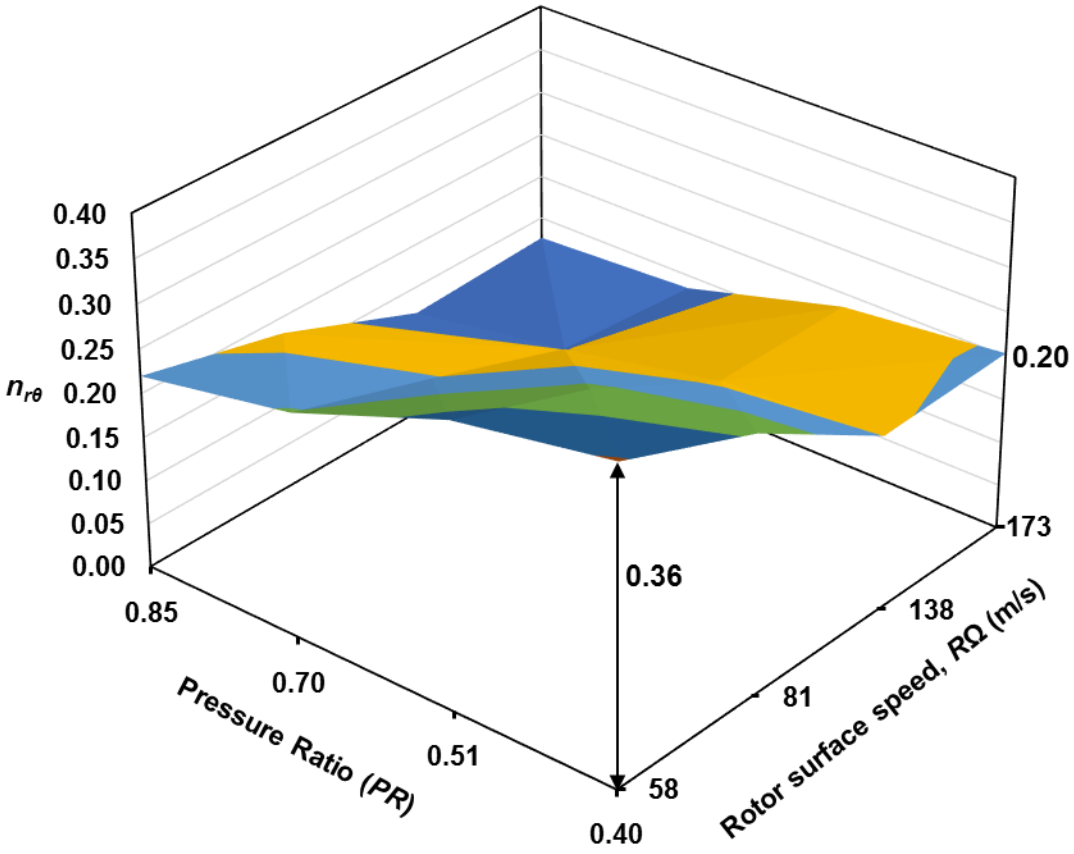

Figure 26. Coefficient $n_{r\theta}$ for friction factor ($f_{r\theta}$) vs. rotor surface speed ($R\Omega$) and vs. pressure ratio (PR) for operation at four radial clearances (0.8, 1.0, 1.2, 2.0)×C_r.

As depicted in Figure 27, $n_{r\theta}$ decreases with an increase in the Reynolds number $Re_{r\theta}$ or pressure ratio PR. $n_{r\theta}$ approaches 0.15 as $Re_{r\theta}$ keeps increasing. Please note that as $n_{r\theta}$ is also a function of PR, there are multiple values for a fixed $Re_{r\theta}$ corresponding to different PR as depicted in Figure 27. As discussed earlier, $n_{r\theta}$ is a function of $Re_{r\theta}$ and PR. Therefore, a curve fit gives the correlation between $n_{r\theta}$ and PR as well as $Re_{r\theta}$,

$$n_{r\theta} = (-11.87 \times PR + 18.36)\,\mathrm{Re}_{r\theta}^{-0.29} \tag{32}$$

where the circumferential flow Reynolds number relative to rotor surface $Re_{r\theta}$ ranges from 8.2×10^5 to 3.2×10^6.

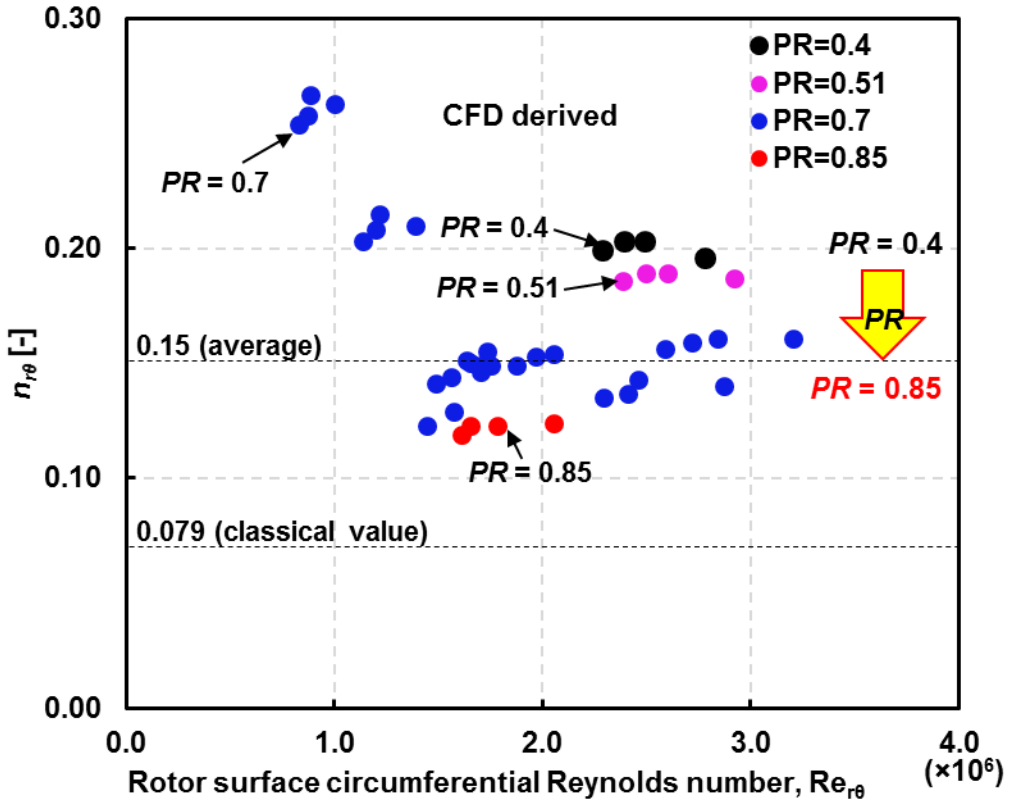

Figure 27. CFD derived coefficient $n_{r\theta}$ for friction factor vs. rotor surface circumferential Reynolds number ($Re_{r\theta}$). LS radial clearances = (0.8, 1.0, 1.2, 2.0)×C_r, P_{in} = 6 ~ 10 MPa, P_{out} = 4 ~ 7 MPa, rotor speed Ω = 5 ~ 15 krpm.

Figure 28 depicts the coefficient $n_{r\theta}$ for the friction factor $f_{r\theta}$ as derived from the CFD results and predicted by the above new model (Eqn. 32) versus rotor circumferential Reynolds number $Re_{r\theta}$. The results show the modified $n_{r\theta}$ has an improved (than the classical Blasius model, $n_{r\theta}$ = 0.079) accuracy when compared with the CFD derived results.

Therefore, the friction factor on the rotor surface ($f_{r\theta} = n_{r\theta}\,\mathrm{Re}_{r\theta}^{-0.25}$) could be expressed as

$$\begin{aligned} f_{r\theta} &= [(-11.87 \times PR + 18.36)\,\mathrm{Re}_{r\theta}^{-0.29}] \times \mathrm{Re}_{r\theta}^{-0.25} \\ &= (-11.87 \times PR + 18.36)\,\mathrm{Re}_{r\theta}^{-0.54} \end{aligned} \tag{33}$$

where $Re_{r\theta}$ ranges from 8.2×10^5 to 3.2×10^6, and the curve fit correlation coefficient R^2 = 0.89.

Figure 29 depicts the rotor surface friction factors ($f_{r\theta}$) derived from the CFD results as well as that predicted by the above new model (Eqn. 33) and the original Blasius friction factor model ($f = 0.079\,\mathrm{Re}^{-0.25}$). The original Blasius friction factor model significantly under estimates $f_{r\theta}$ by ~50%. On the other hand, the modified friction factor ($f_{r\theta}$) model shows a much better accuracy when compared to the CFD derived $f_{r\theta}$. For $Re_{r\theta} < 1.0 \times 10^6$, the maximum discrepancy between the modified friction factor model and the CFD predicted $f_{r\theta}$ is ~25%. For $Re_{r\theta} > 1.0 \times 10^6$, the modified friction factor model predicts $f_{r\theta}$ within 10% of the CFD derived results.

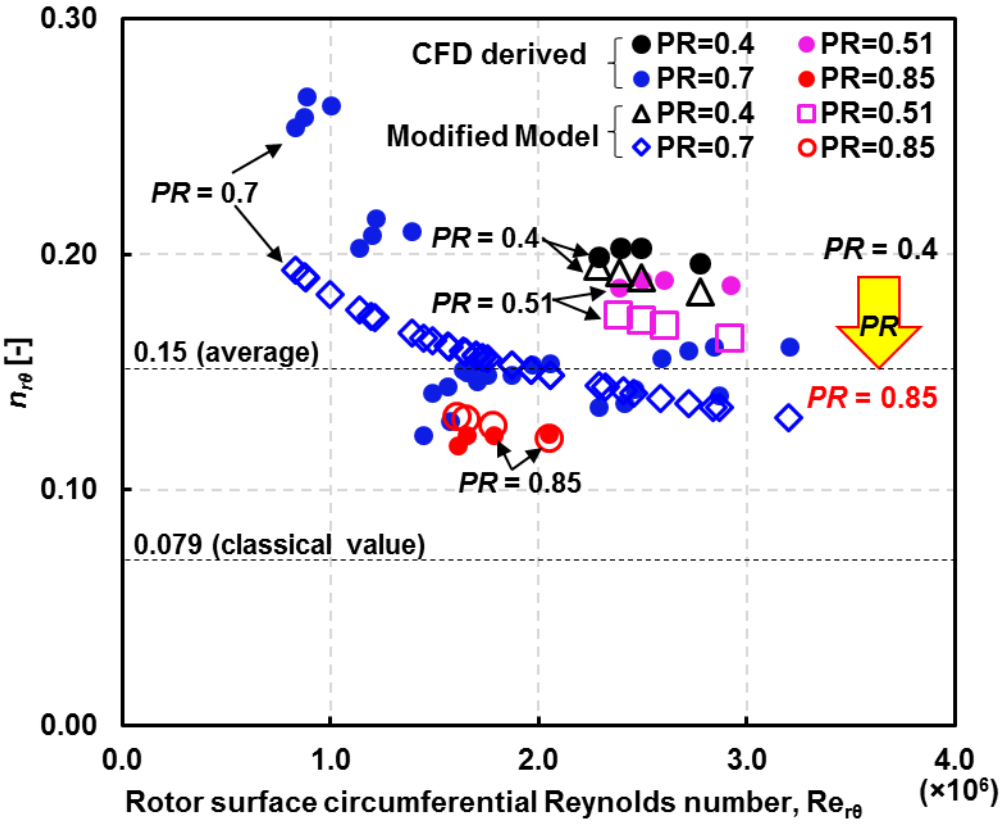

Figure 28. CFD derived and new model predicted coefficient $n_{r\theta}$ for friction factor vs. rotor surface circumferential Reynolds number ($Re_{r\theta}$). LS radial clearances = (0.8, 1.0, 1.2, 2.0)×C_r, P_{in} = 6 ~ 10 MPa, P_{out} = 4 ~ 7 MPa, rotor speed Ω = 5 ~ 15 krpm.

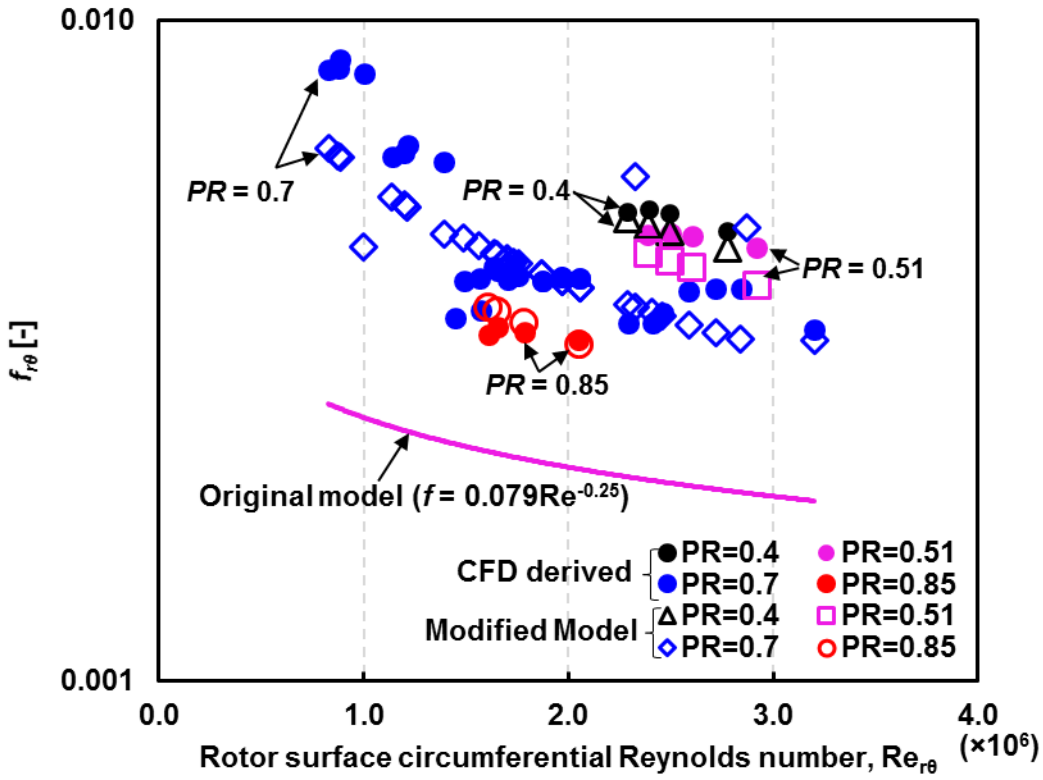

Figure 29. Rotor surface friction factor $f_{r\theta}$ vs. stator surface circumferential Reynolds number ($Re_{r\theta}$): CFD derived, modified model and original model. LS radial clearances = (0.8, 1.0, 1.2, 2.0)×C_r, P_{in} = 6 ~ 10 MPa, P_{out} = 4 ~ 7 MPa, rotor speed Ω = 5 ~ 15 krpm, inlet swirl velocity ratio α =0 ~ 0.73.

5.6.2 Stator Surface Friction Factor $f_{s\theta}$

The CFD analysis results show that the friction factor on the stator surface ($f_{s\theta}$) is a function of the radial clearance (C_r), pressure ratio PR, rotor surface speed $R\Omega$, and the inlet swirl velocity (U_0). Figure 30 depicts the CFD derived coefficient $n_{s\theta}$ for friction factor $f_{s\theta}$ versus the pressure ratio (PR) and rotor surface speed ($R\Omega$). $n_{s\theta}$ decreases with respect to an increase in rotor surface speed ($R\Omega$) or the pressure ratio (PR).

One should note that the effect of the radial clearance (C_r), rotor surface speed ($R\Omega$) and the pre-swirl velocity (U_0) can be expressed in terms of the circumferential Reynolds number relative

to the stator surface, $\mathrm{Re}_{s\theta} = \rho D_h U/\mu$. On the other hand, $n_{s\theta}$ is also proportional to changes in *PR*. Therefore, $n_{s\theta}$ could be expressed as a function of $Re_{s\theta}$ and *PR*.

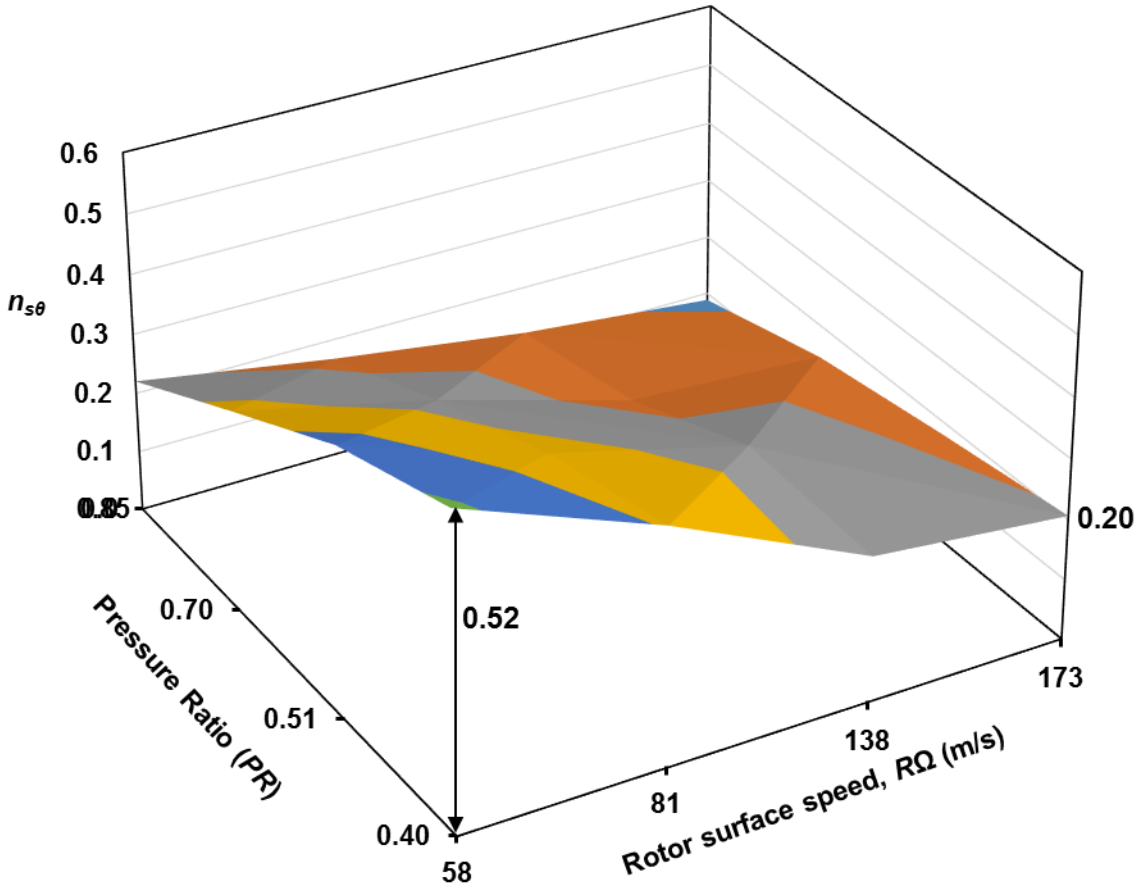

Figure 30. CFD derived coefficient $n_{s\theta}$ for friction factor $f_{s\theta}$ vs. pressure ratio (*PR*) and rotor surface speed ($R\Omega$). LS radial clearances = 0.8C_r, P_{in} = 6 ~ 10 MPa, P_{out} = 4 ~ 7 MPa, rotor speed Ω = 5 ~ 15 krpm, inlet swirl velocity ratio α = 0.

To consider the effects of the radial clearance (C_r), pressure ratio *PR*, rotor surface speed $R\Omega$, and the inlet swirl velocity (U_0), a curve fit gives $n_{s\theta}$ as

$$n_{s\theta} = (-24.6 \times PR + 30.7) Re_{s\theta}^{-0.32} \tag{34}$$

where the Reynolds number $Re_{s\theta}$ ranges from 7.2×10^4 to 1.1×10^6 and *PR* = 0.4 ~ 0.85. As depicted in Figure 31, $n_{s\theta}$ decreases with an increase in the Reynolds number $Re_{s\theta}$ and pressure ratio *PR*; $n_{s\theta}$

approaches 0.1 as $Re_{s\theta}$ increases. Please note that since $n_{s\theta}$ is also a function of *PR* the graph shows multiple values for a fixed $Re_{s\theta}$ and corresponding to different *PR*, as depicted in Figure 31.

Figure 32 depicts both the CFD derived and the above new model (Eqn. 34) coefficient $n_{s\theta}$ versus $Re_{s\theta}$. The results show the modified model for $n_{s\theta}$ has a better accuracy when compared with the CFD derived results, than the classical Blasius model ($n_{s\theta} = 0.079$).

Therefore, the friction factor on the stator surface ($f_{s\theta} = n_{s\theta}\,\mathrm{Re}_{s\theta}^{-0.25}$) is expressed as

$$\begin{aligned} f_{s\theta} &= [(-24.6 \times PR + 30.7) Re_{s\theta}^{-0.32}] \times \mathrm{Re}_{s\theta}^{-0.25} \\ &= (-24.6 \times PR + 30.7)\,\mathrm{Re}_{s\theta}^{-0.57} \end{aligned} \tag{35}$$

where $Re_{s\theta}$ ranges from 7.2×10^4 to 1.1×10^6, and the curve fit correlation coefficient $R^2 = 0.80$.

Figure 33 depicts the stator surface friction factors ($f_{s\theta}$) derived from the CFD results as well as that predicted by the above new model (Eqn. 35) and the original Blasius friction factor model ($f = 0.079\,\mathrm{Re}^{-0.25}$). The original model significantly under estimates $f_{s\theta}$. On the other hand, the new friction factor model shows a significantly improved accuracy when compared to the CFD derived $f_{s\theta}$.

For $Re_{r\theta} < 2.0\times10^5$, the maximum discrepancy between the modified friction factor model and the CFD predicted $f_{r\theta}$ is ~50%. For $Re_{r\theta} > 2.0\times10^5$, the modified friction factor model predicts $f_{r\theta}$ within 15% of the CFD derived results.

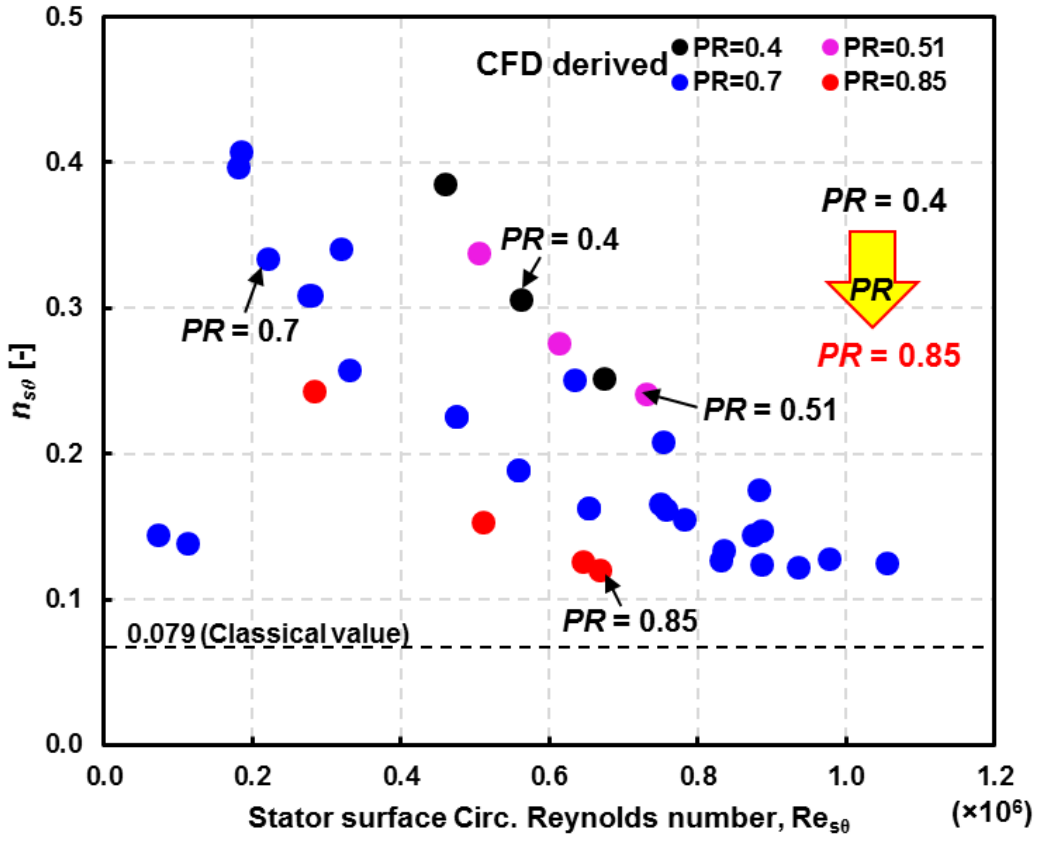

Figure 31. CFD derived coefficient $n_{s\theta}$ for friction factor $f_{s\theta}$ vs. stator surface circumferential Reynolds number ($Re_{s\theta}$). LS radial clearances = (0.8, 1.0, 1.2, 2.0)×C_r, P_{in} = 6 ~ 10 MPa, P_{out} = 4 ~ 7 MPa, rotor speed Ω = 5 ~ 15 krpm, inlet swirl velocity ratio α =0 ~ 0.73.

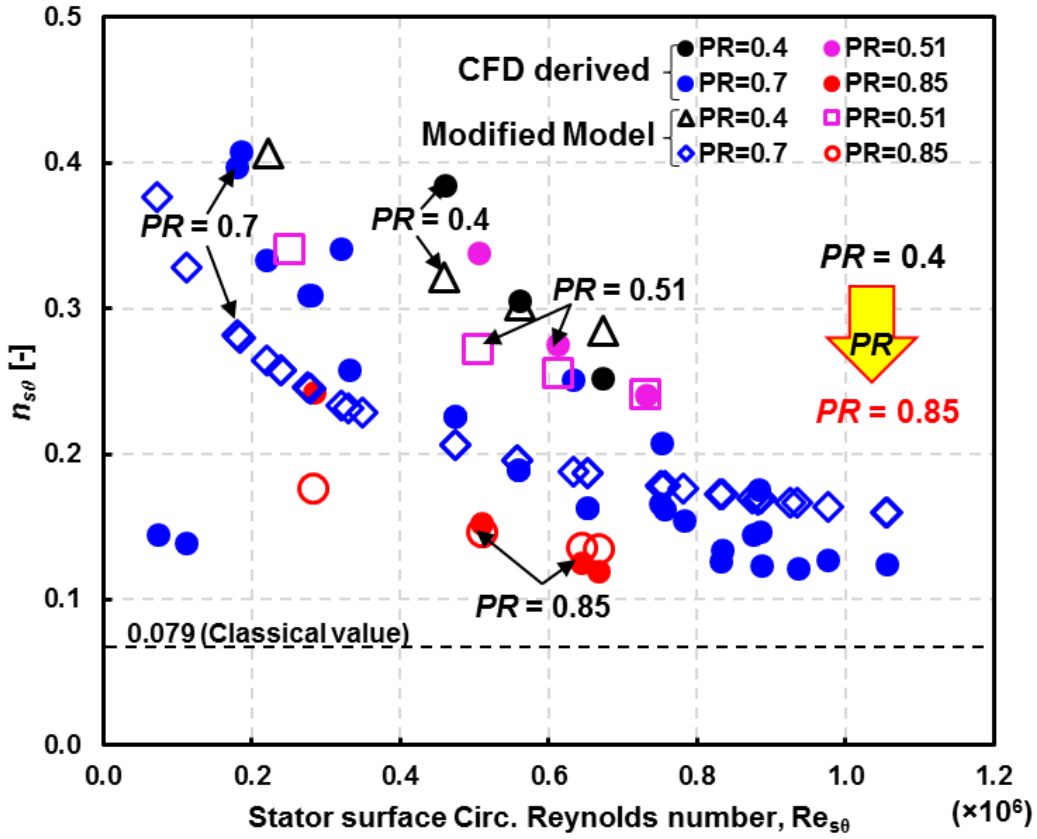

Figure 32. CFD derived and new model predicted coefficient $n_{s\theta}$ for friction factor $f_{s\theta}$ vs. stator surface circumferential Reynolds number ($Re_{s\theta}$). LS radial clearances = (0.8, 1.0, 1.2, 2.0)×C_r, P_{in} = 6 ~ 10 MPa, P_{out} = 4 ~ 7 MPa, rotor speed Ω = 5 ~ 15 krpm, inlet swirl velocity ratio α =0 ~ 0.73.

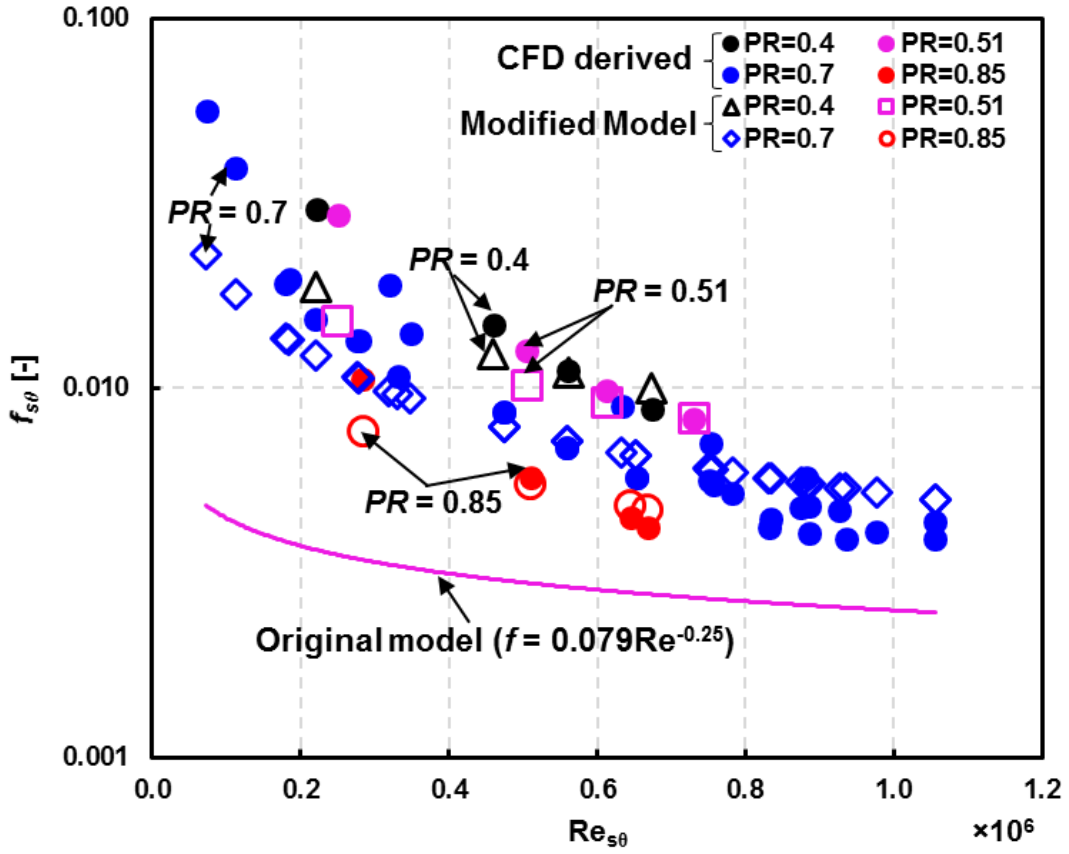

Figure 33. Stator surface friction factor $f_{s\theta}$ vs. stator surface circumferential Reynolds number ($Re_{s\theta}$): CFD derived, new model and original model predicted. LS radial clearances = (0.8, 1.0, 1.2, 2.0)×C_r, P_{in} = 6 ~ 10 MPa, P_{out} = 4 ~ 7 MPa, rotor speed Ω = 5 ~ 15 krpm, inlet swirl velocity ratio α =0 ~ 0.73.

VI. CFD DERIVED FLOW COEFFICIENTS

Note the procedure to calculate the seal mass flow rate as well as the cavity pressures is well documented in a prior (2017) TRC report [60]; henceforth not discussed here.

For a compressible fluid, the density (ρ) is a function of the local pressure, thus varying from cavity to cavity. From the seal inlet plane towards the outlet plane, the circumferential flow velocity develops. Recall, the BFM assumes the cavity pressure (and density), and the circumferential velocity are constant within a cavity. Therefore, all the variables extracted from CFD results in a representative analysis should correspond to an average across the cavity width and radial depth.

Figure 34(a) shows the contours of density along the seal. The density within a cavity (#1-#13) is almost uniform; and so does the tangential velocity in (b). Figure 34 (c) and (d) depict from the seal inlet plane to the outlet plane the cross-film average (normalized) density (ρ/ρ_s) and the cross-film average (normalized) circumferential velocity (U/U_{rotor}, $U_{rotor} = R\Omega$). The cavity density (and pressure) shows a linear drop from the seal inlet plane toward the outlet plane whereas the fluid tangential velocity in a cavity grows towards the seal discharge. Recall a null pre-swirl condition is applied and the seal is short in length ($L/D = 0.3 < 0.5$); hence the fluid mean circumferential velocity in the last cavity is less than $\frac{1}{2}D\Omega$.

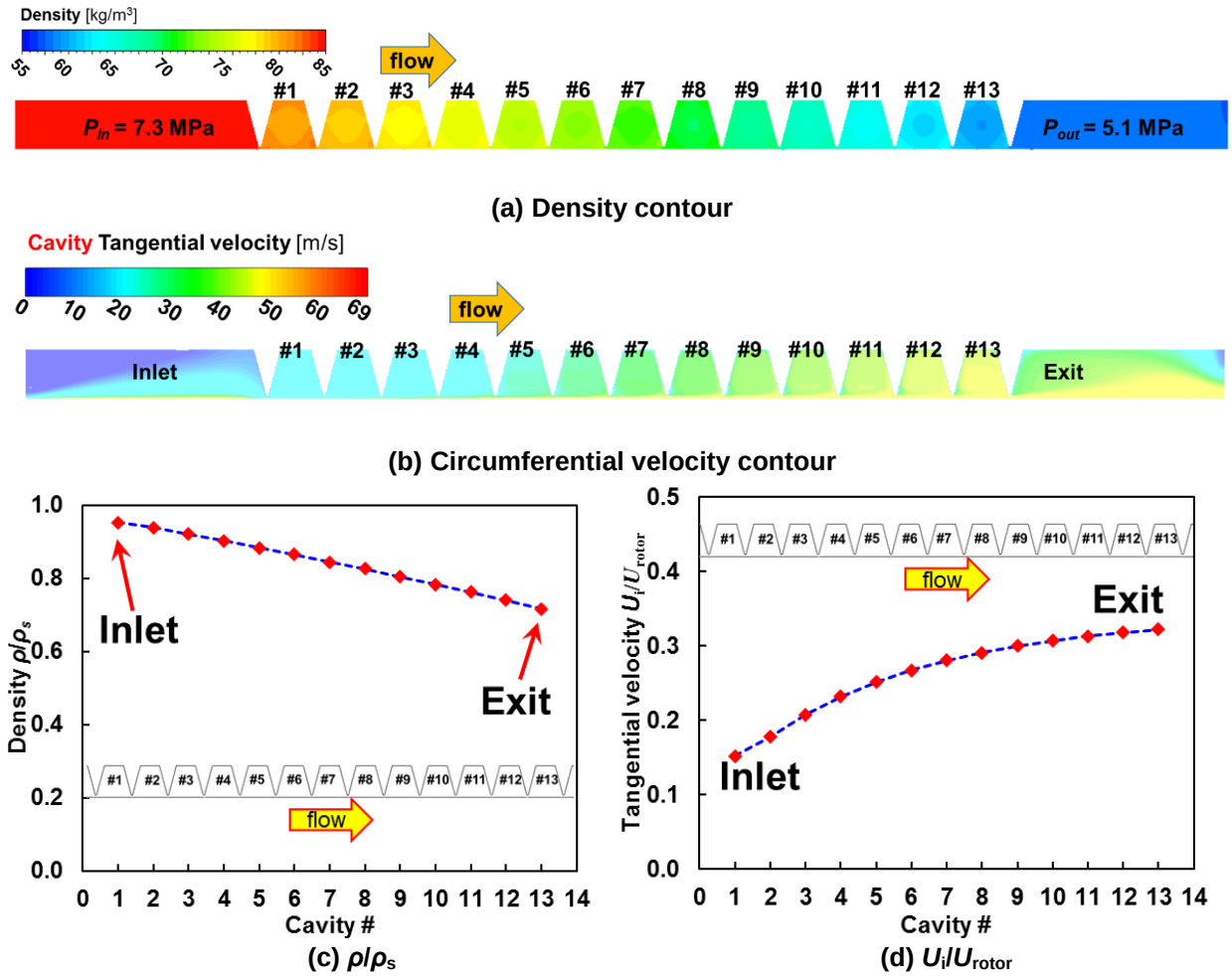

Figure 34. CFD predictions for a TOS LS: (a) density contours; (b) circumferential velocity contours; (c) cross-film averaged cavity density (ρ/ρ_s); (d) cross-film averaged tangential velocity (U_i/U_{rotor}) within a cavity. P_{in} = 7.3 MPa, P_{out} = 5.1 MPa, rotor speed = 12 krpm (138 m/s).

In engineering practice, the seal radial clearance C_r ranges from 3~5‰ of the rotor radius and increases after a period of operation due to the wear. In this study, the seal has a nominal radial clearance C_r = 3‰×R, and cases with up to 2×C_r (6‰×R) are included to account for seal wear conditions. Table 8 lists the TOS labyrinth seal mass flow rate predicted by both the CFD and BFM methods. As the seal radial clearance varies from 80% to 200% of the nominal size (C_r = 0.3mm), the current BFM under-estimates the mass flow rate by 6.9%~18.9%. The supply pressure

P_{in} increases from 60 bar to 100 bar, where the pressure ratio $PR = P_{out}/P_{in}$ = 0.4 ~0.85, and the rotor speed is 12 krpm ($R\Omega$ = 138 m/s).

For all the operating conditions herein considered, the discrepancy between BFM and CFD predictions ranges from 1.5% to 18.9%. The seal with $2\times C_r$ shows the maximum difference (18.9%) between the CFD and BFM predicted mass flow rates. When the supply pressure is fixed, the discrepancy between CFD and BFM predicted mass flow rates increases with respect to the pressure ratio *PR*. On the other hand, for a fixed *PR*, the larger the supply pressure P_{in}, the more different the BFM predicted mass flow rate becomes when compared to the CFD prediction.

Table 8. CFD and BFM predicted mass flow rate of TOS labyrinth seals, seal radial clearance = (0.8, 1.0, 1.2, 2.0) ×C_r, supply pressure increases from 60 to 100 bar, pressure ratio $PR = P_{out}/P_{in}$ = 0.4 ~ 0.85, and rotor speed Ω = 12 krpm ($R\Omega$ = 138 m/s).

Operating Conditions	Prediction Method	Mass Flow Rate [kg/s]			
		0.8 × Cr	**1.0 × Cr**	**1.2 × Cr**	**2.0 × Cr**
P_{in}=60 bar, *PR* = 0.85	CFD	0.495	0.606	0.865	1.868
	BFM	0.460	0.615	0.781	1.515
	Diff.	**-6.9%**	**1.5%**	**-9.7%**	**-18.9%**
P_{in} =72.8 bar, *PR* = 0.7	CFD	0.835	1.123	1.446	3.081
	BFM	0.760	1.017	1.291	2.509
	Diff.	**-8.9%**	**-9.5%**	**-10.7%**	**-18.5%**
P_{in} =100 bar, *PR* = 0.4	CFD	1.465	1.960	2.525	5.181
	BFM	1.355	1.811	2.303	4.485
	Diff.	**-7.5%**	**-7.6%**	**-8.8%**	**-13.4%**
P_{in} =100 bar, *PR* = 0.5	CFD	1.387	1.859	2.397	4.964
	BFM	1.274	1.702	2.163	4.205
	Diff.	**-8.1%**	**-8.4%**	**-9.8%**	**-15.3%**
P_{in} =100 bar, *PR* = 0.7	CFD	1.153	1.550	2.000	4.246
	BFM	1.045	1.397	1.774	3.447
	Diff.	**-9.4%**	**-9.9%**	**-11.3%**	**-18.8%**

Figure 35(a) depicts both the CFD and BFM mass flow rates versus pressure ratio (*PR*). The lows are normalized with respect to the ones obtained for the nominal clearance ($1\times C_r$). For a large C_r (>1), the discrepancy between CFD and BFM predictions grows larger.

The flow factor $\phi = \dot{m}\sqrt{T}/(P_{in}D)$ introduced by Delgado and Proctor [35] serves to quantify the leakage of gas seals in a manner that shows independence of the seal size (diameter *D*) and inlet flow conditions, namely pressure (P_{in}) and temperature (*T*). Figure 35(b) shows the flow factor ($\phi = \dot{m}\sqrt{T}/(D \cdot P_{in})$) versus pressure ratio (*PR*) for both CFD and BFM predictions. The flow factor ϕ decreases with respect to an increase in *PR*, the difference between CFD and BFM predictions increases with an increase in C_r. Therefore, the effects of seal radial clearance C_r and the operating pressure ratio *PR* should be considered in the modification of flow equations.

San Andrés et al. [54]introduce a modified flow factor

$$\bar{\Phi} = \frac{\phi}{\sqrt{1-PR^2}} = \frac{\dot{m}\sqrt{T}}{D\,P_{in}\sqrt{1-PR^2}} \sim \pi\ \ c_d\, C_r \frac{1}{\sqrt{R_g}} \tag{36}$$

which can easily lead to the determination of a seal loss coefficient c_d, or as in some cases, the definition of an effective clearance ($C_{eff} = c_d \times C_r$), both representing the seal effectiveness to reduce leakage. Figure 36 depicts the modified flow factor ($\bar{\Phi}$) versus pressure ratio and the various clearances considered. $\bar{\Phi}$ increases with respect to an increase in seal radial clearance C_r; whereas for a fixed C_r, $\bar{\Phi}$ remains almost constant as *PR* varies from 0.4 to 0.85. On the other hand, the flow coefficient $c_d = C_{eff}/C_r$, the lowest magnitude desired to make more effective the seal resistance to leakage, increases with respect to the physical clearance magnitude.

Figure 37 depicts the CFD predicted cavity pressure (P_i/P_{in}) vs. cavity number for seals under different operating pressures. The flow passes through the upstream cavity and suffers a sudden flow contraction at the first seal tooth. Therefore, the flow velocity increases and so does the kinetic energy. As a result, the first cavity pressure shows a sudden drop.

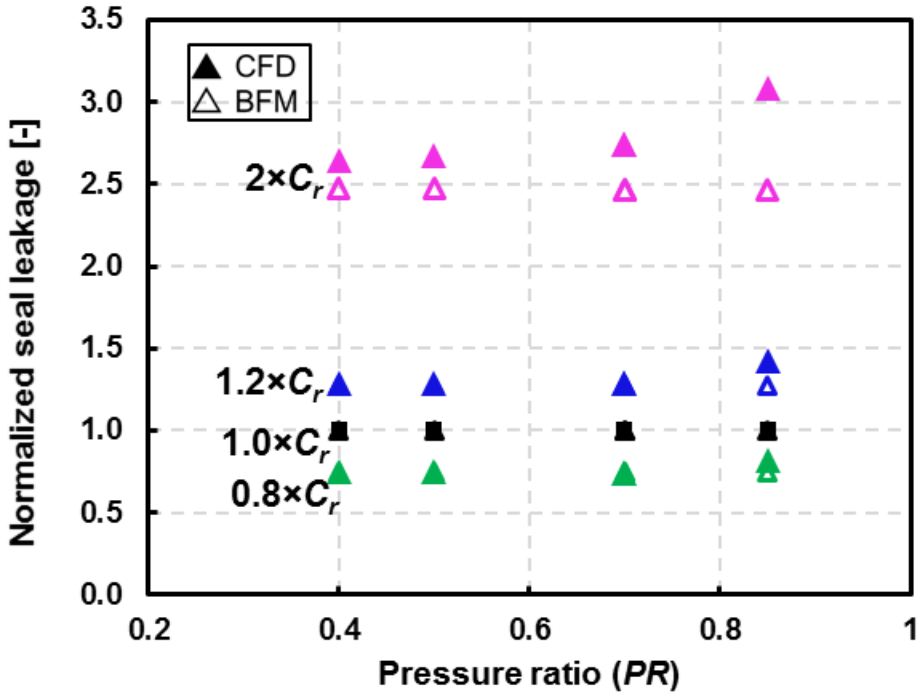

(a)

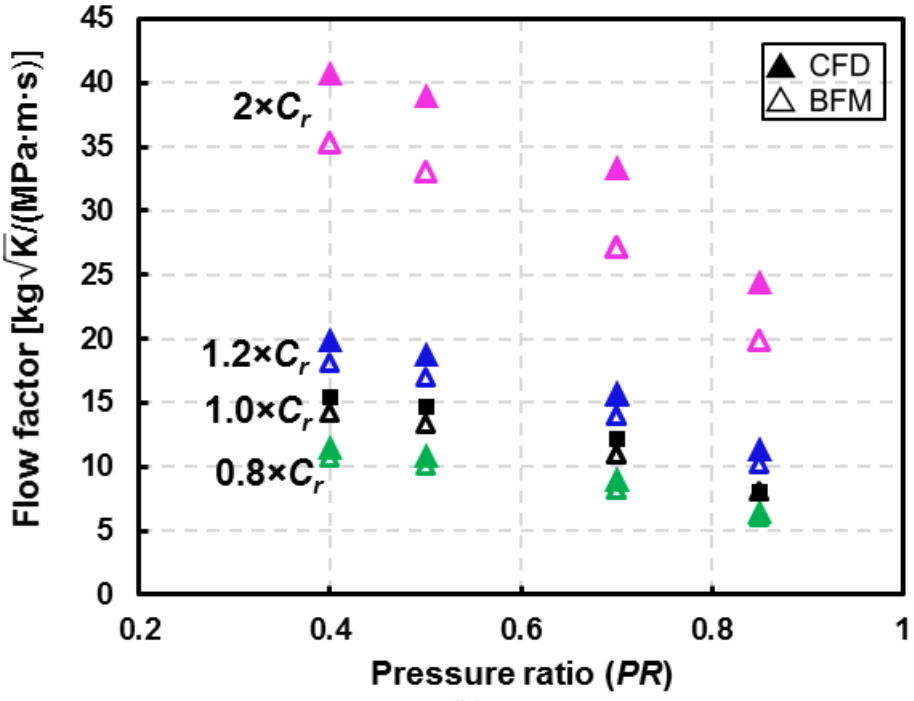

(b)

Figure 35. CFD and BFM predicted (a) normalized mass flow rate vs. *PR*; (b) flow factor vs. *PR*. TOS labyrinth seal, radial clearance = (0.8, 1.0, 1.2, 2.0) ×C_r, supply pressure increases from 60 to 100 bar, pressure ratio *PR*= P_{out}/P_{in} = 0.4 ~ 0.85, and rotor speed Ω = 12 krpm ($R\Omega$ = 138 m/s).

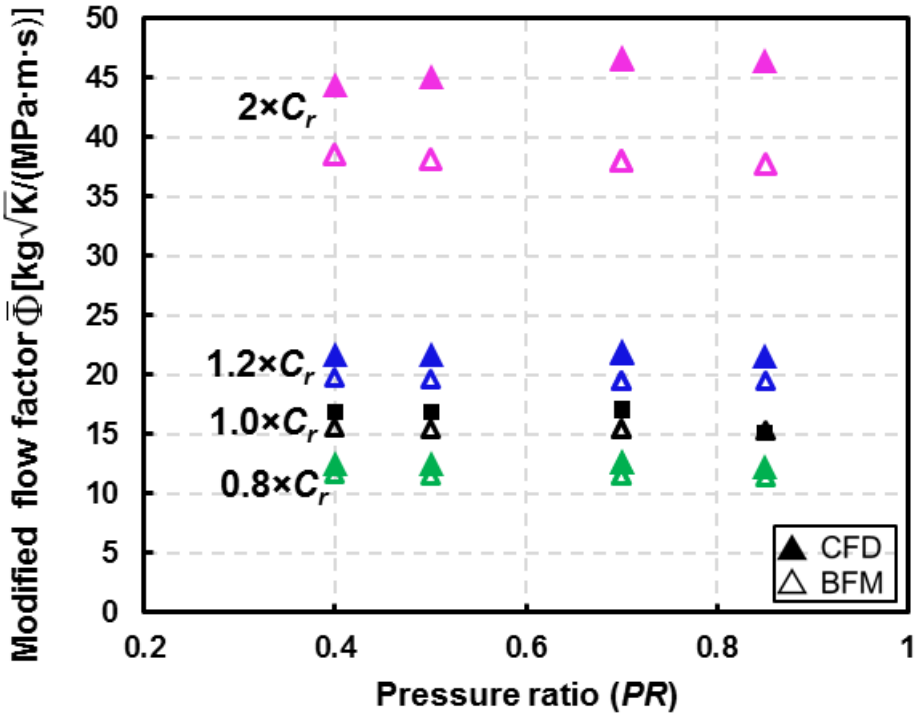

(a)

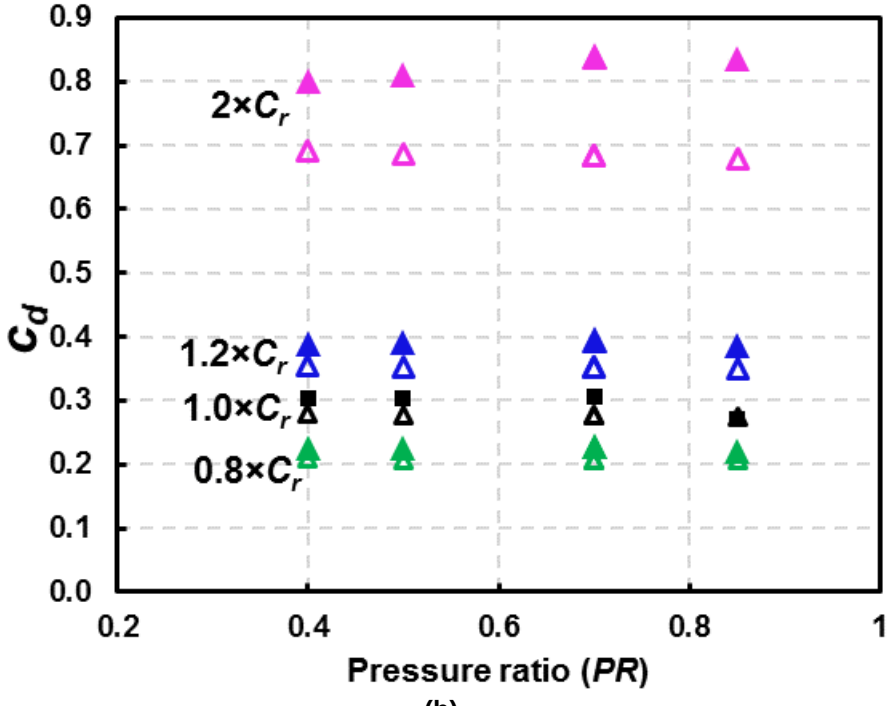

(b)

Figure 36. CFD and BFM predicted modified flow factor ($\bar{\Phi}$) and flow coefficient (c_d) vs. seal *PR*= P_{out}/P_{in}. TOS labyrinth seal, radial clearance = (0.8, 1.0, 1.2, 2.0) ×*C*. Supply pressure varies from 60 to 100 bar and rotor speed Ω = 12 krpm (*R*Ω = 138 m/s).

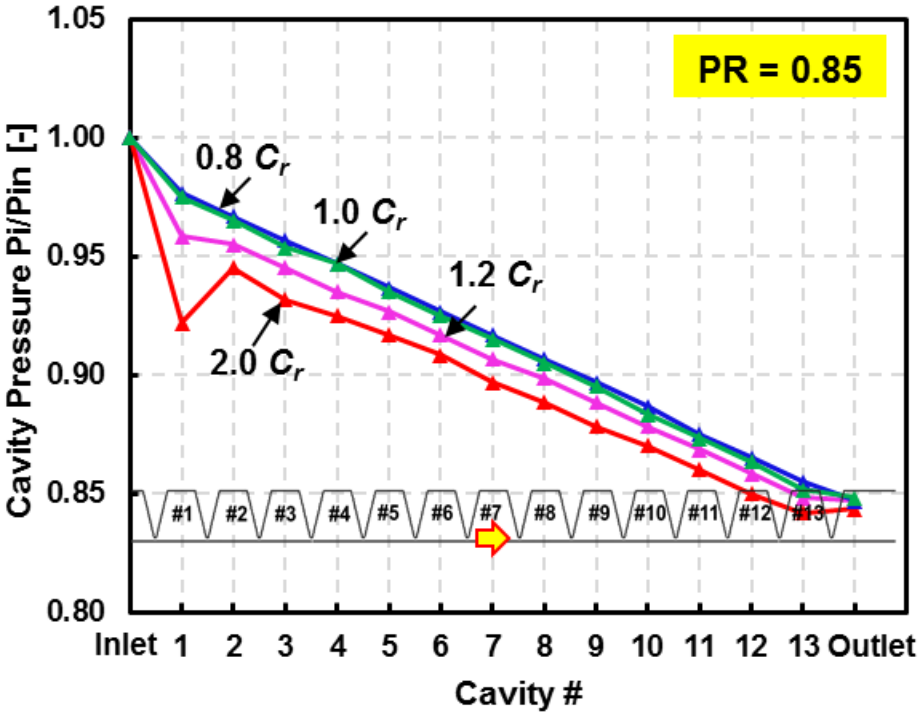

(a) P_{in} = 60 bar, PR = 0.85

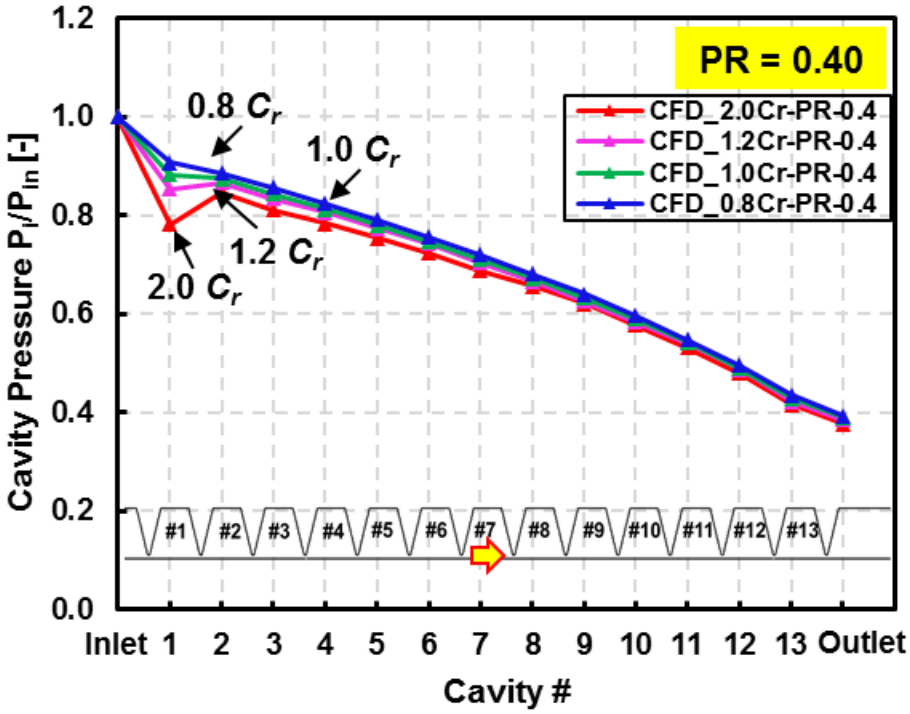

(b) P_{in} = 100 bar, PR = 0.4

Figure 37. CFD predicted cavity pressure (P_i/P_{in}) vs. cavity #. TOS labyrinth seal with radial clearance ranging from 0.8×C_r to 2.0 ×C_r, rotor speed Ω = 12 krpm ($R\Omega$ = 138 m/s). (a) supply pressure P_{in} = 60 bar, pressure ratio PR = 0.85; (b) supply pressure P_{in} = 100 bar, pressure ratio PR = 0.40.

6.1 Modified Leakage Prediction Model

Figure 38(a) depicts the flow velocity contours for the TOS labyrinth seals with $1\times C_r$ and $2\times C_r$. As the flow enters the seal, the larger the radial clearance is, the higher the increase in flow velocity. Therefore, for the seal with a larger radial clearance, the first cavity pressure drops more than that in the TOS labyrinth seal with a smaller clearance. On the other hand, as the seal radial clearance increases, the first cavity develops a stronger vortex with respect to C_r, which later contributes to the static pressure recovery in the second cavity. The flow velocity in the second cavity shows a decrease compared to that in the first cavity. Figure 38(b) depicts the normalized cavity velocity magnitude (cross-film averaged), as referenced to that in the first cavity, i.e. (V_i/V_1). For all operating conditions considered hereby, the velocity in the second cavity decreases, hence explaining the static pressure recovery in the second cavity shown in Figure 37. For a fixed clearance, the percentage of decrease in velocity at the second cavity is a function of the pressure ratio *PR* only; the lowest *PR* produces the maximum velocity decrease in terms of percentage. For a fixed supply pressure P_{in}, the cavity flow velocity develops faster for the case with a low pressure ratio *PR*. For a fixed pressure ratio *PR*, a larger supply pressure leads to a slower cavity velocity development.

Figure 39 depicts the CFD and BFM predicted cavity pressure distribution vs. cavity number. The current BFM model cannot accurately calculate the pressure drop across the first tooth, and which is significantly lower than that from the CFD prediction. The discrepancy increases with an increase in the seal radial clearance.

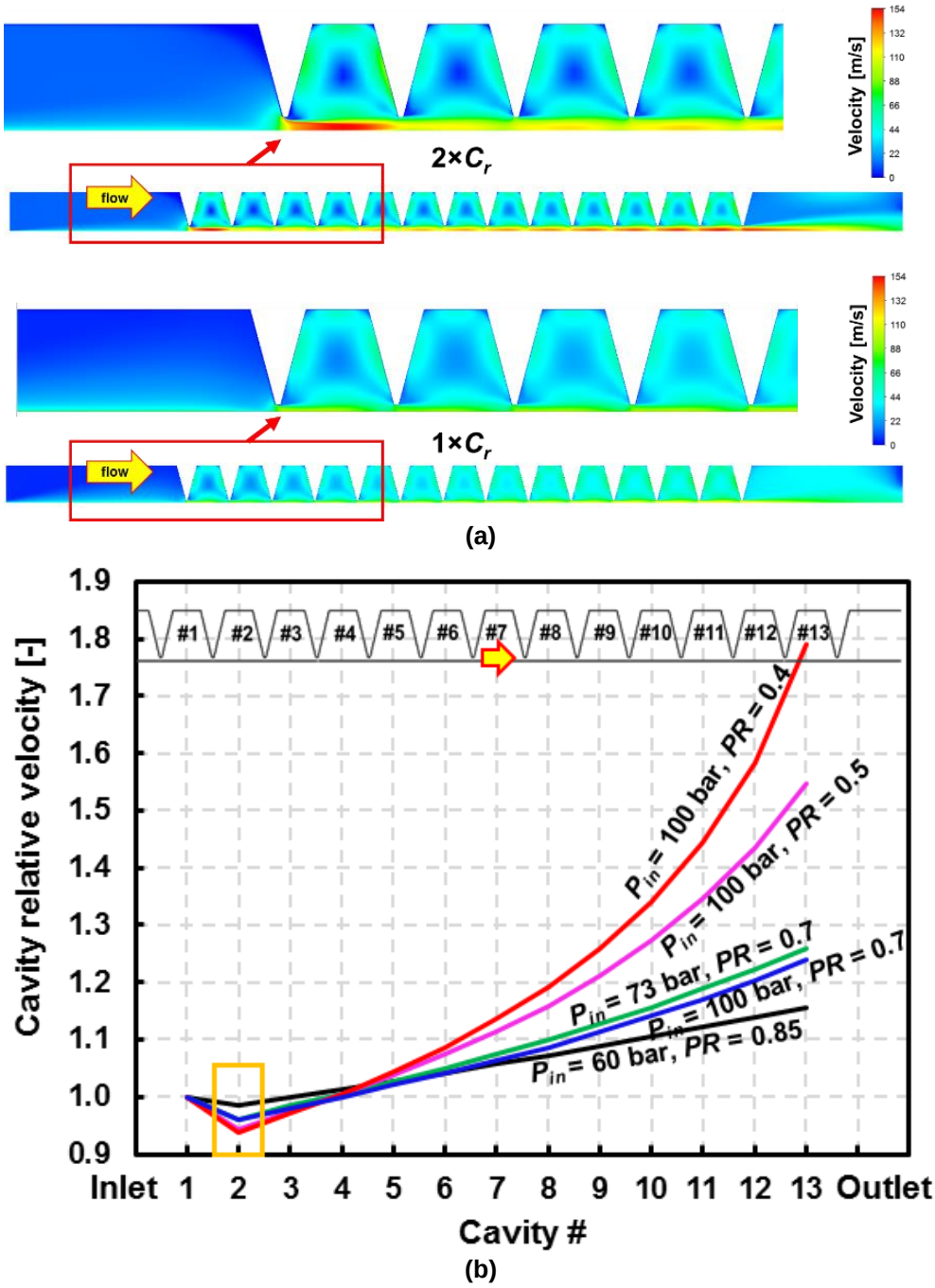

Figure 38. CFD predicted cavity velocity vs. cavity #. TOS labyrinth seal with (a) radial clearance = 1×C_r and 2.0 ×C_r, supply pressure P_{in} = 100 bar, pressure ratio PR = 0.7; (b) radial clearance = 2.0×C_r, supply pressure P_{in} = 60 bar, 73 bar, 100 bar, pressure ratio PR = 0.40, 0.5, 0.7, 0.85. Rotor speed Ω = 12 krpm (RΩ = 138 m/s).

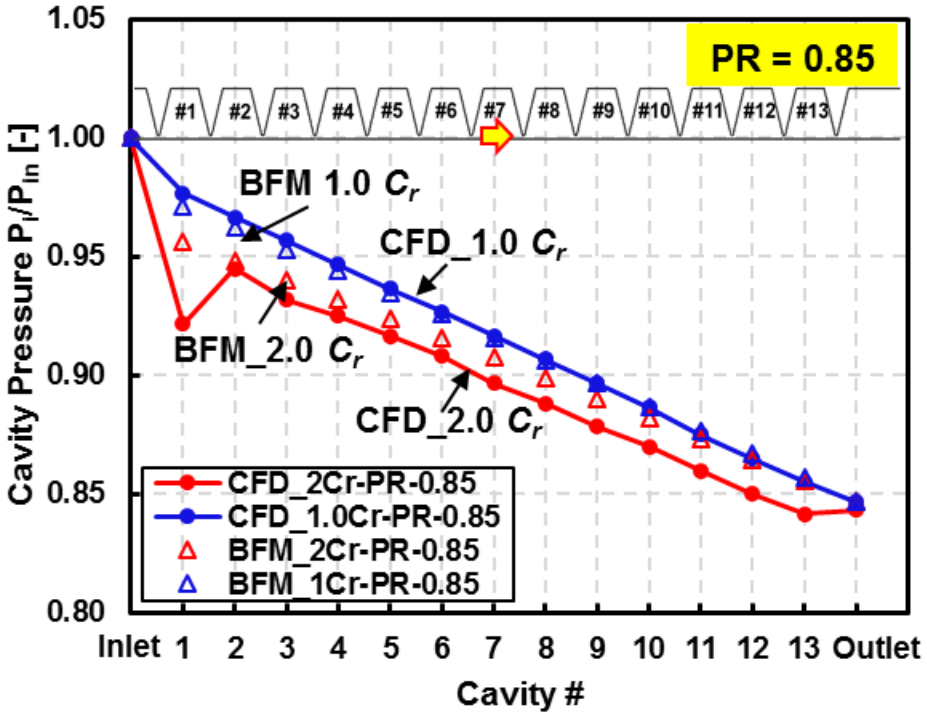

(a) P_{in} = 60 bar, PR = 0.85

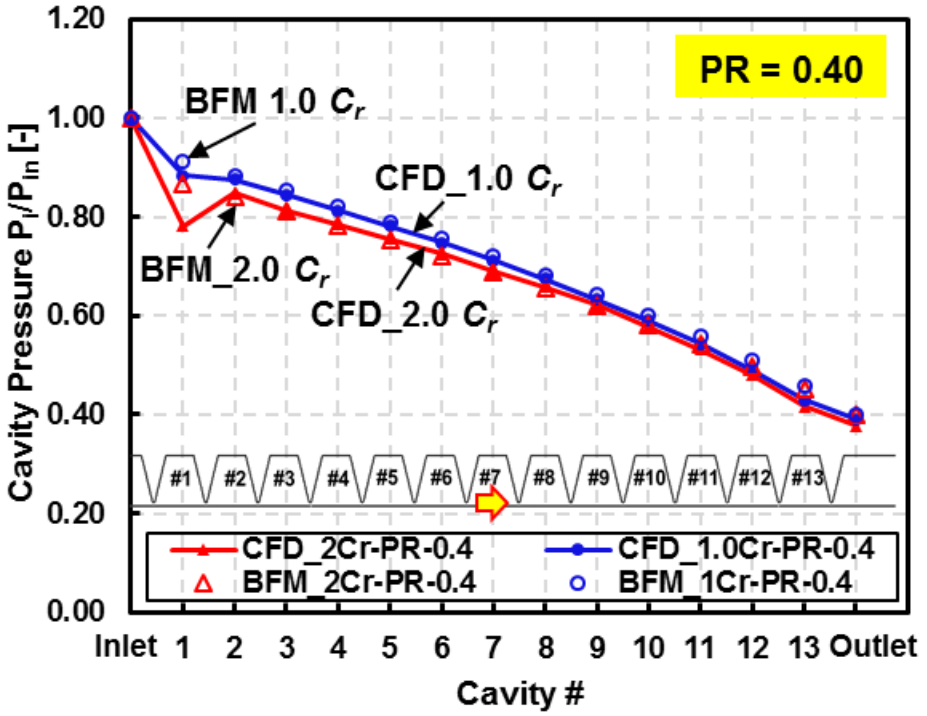

(b) P_{in} = 100 bar, PR = 0.4

Figure 39. CFD and BFM predicted cavity pressure (P_i/P_{in}) vs. cavity #. TOS labyrinth seal with radial clearance = 1.0×C_r and 2.0 ×C_r, rotor speed Ω = 12 krpm. (a) supply pressure P_{in} = 60 bar, pressure ratio PR = 0.85; (b) supply pressure P_{in} = 100 bar, pressure ratio PR = 0.40.

Recall that the BFM utilizes Neumann's Eqn. (3) to calculate the seal leakage as well as the cavity pressure distribution. In Eqn. (3), the flow discharge coefficient μ_{2i} is a function of the cavity pressure distribution, whereas the kinetic energy carry-over coefficient (μ_{1i}) is a function of the seal geometry (radial clearance C_r and tooth pitch L_i). Recall, μ_{1i} for the first tooth of a labyrinth seal is unity. One should note that the current leakage model does not take the effect of pressure ratio (*PR*) into consideration, whereas the above analysis shows the cavity pressure distribution is a function of the pressure ratio, particularly at the first cavity.

With the CFD predicted mass flow rate and cavity pressures, one could calculate the flow discharge coefficient μ_{2i} for each tooth, and therefore derive the corresponding kinetic energy carry-over coefficient μ_{1i}. Table 9 lists the kinetic energy carry-over coefficient μ_{1i} derived from CFD predictions and calculated from

$$\mu_{1i} = \frac{\dot{m}_i}{\left(\mu_{2i} \left(\pi D C_r \right) \sqrt{\dfrac{P_{i-1}^2 - P_i^2}{R_g T}} \right)}, \; i = 1, 2, \cdots, N \tag{37}$$

and the μ_{1i} in the original Neumann equations, i.e. $\mu_{1i} = \sqrt{NT / \left((1-\lambda) NT + \lambda \right)}$ with $\lambda = 1 - \left(1 + 16.6 \, C_r / L_i \right)^{-2}$. One should note that for those cases with a strong first cavity pressure drop and a second cavity pressure recovery, $P_1 < P_2$. Thus, $(P_1^2 - P_2^2) < 0$ and from Eq. (3), $\mu_{12} \sim \dot{m}_2 \Big/ \left(\sqrt{P_1^2 - P_2^2} \right)$ at the second tooth has no meaning as it would be an imaginary number. That is, the CFD predicted kinetic energy carry-over coefficient for the second tooth (μ_{12}) could not be calculated. On the other hand, the pressure drop ($\Delta P_{14} = P_{13} - P_{14}$) across the last tooth is

relatively smaller than that across other teeth; hence giving a lower μ_2 which produces the unusual jump in μ_1, as seen in the last row in Table 9.

Different from the CFD simulations, the BFM cannot capture flow details within a cavity, neither the pressure recovery occurring in the second cavity. The CFD predicted cavity pressure distribution indicates that the pressure drop along the axial direction is not strictly linear. Thus, the CFD derived μ_{1i} varies from cavity to cavity, see Table 9. In order to adequately account the pressure variations as predicted by CFD simulations, μ_{1i} is obtained from an average of the CFD predictions listed in Table 10, though excluding the values obtained at the first (#1) and last (#14) teeth. The original Eqns. (5) and (6) underestimate the kinetic energy carry-over coefficient μ_{1i} by up to 52% when compared to the CFD predictions.

Table 9. Kinetic energy carry-over coefficient μ_{1i} derived from CFD predictions. TOS labyrinth seal with radial clearance = (0.8, 1.0, 1.2, 2.0) ×C_r, supply pressure P_{in} = 100 bar, pressure ratio PR= P_{out}/P_{in} = 0.4, and rotor speed Ω = 12 krpm (RΩ = 138 m/s).

Tooth #	0.8C_r -100bar-PR0.4	1C_r -100bar- PR0.4	1.2C_r -100bar- PR0.4	2C_r -100bar- PR0.4
1	0.98	0.93	0.89	0.89
2	2.16	3.80	**N/A**	**N/A**
3	1.83	1.94	2.02	2.41
4	1.80	1.94	2.24	2.85
5	1.83	1.98	2.10	2.75
6	1.76	1.96	2.21	2.75
7	1.80	1.94	2.01	2.65
8	1.78	1.97	2.15	2.88
9	1.80	1.92	2.07	2.70
10	1.77	1.93	2.11	2.55
11	1.74	1.91	2.16	2.61
12	1.76	1.88	2.00	2.53
13	1.70	1.84	1.91	2.39
14	2.20	2.49	2.73	3.30
Eq. (5)	1.67	1.81	1.95	2.39

Table 10. Updated kinetic energy carry-over coefficient μ_{1i} derived from average CFD predictions (Table 4). TOS labyrinth seal with radial clearance = (0.8, 1.0, 1.2, 2.0) ×C_r, supply pressure P_{in} = 60 ~ 100 bar, pressure ratio $PR = P_{out}/P_{in}$ ranges from 0.4 to 0.85, and rotor speed Ω = 12 krpm ($R\Omega$ = 138 m/s).

Operating Conditions	New μ_{1i} (i = 2, 3, …, NT)			
	0.8 × Cr	**1.0 × Cr**	**1.2 × Cr**	**2.0 × Cr**
P_{in} =60 bar, PR = 0.85	1.80	1.76	2.20	3.11
P_{in} =72.8 bar, PR = 0.7	1.89	2.06	2.28	3.27
P_{in} =100 bar, PR = 0.4	1.84	2.01	2.20	2.96
P_{in} =100 bar, PR = 0.5	1.85	2.03	2.24	3.06
P_{in} =100 bar, PR = 0.7	1.90	2.08	2.30	3.30
Original Eqn. (5)	1.67	1.81	1.95	2.39

Figure 40 illustrates the updated μ_{1i} (listed in Table 10) vs. radial clearance for seals operating with various pressure ratios (PR). In general, the new μ_{1i} increases linearly with respect to the seal radial clearance. On the other hand, the new μ_{1i} shows a non-linear correlation with the pressure ratio PR.

Towards delivering more accurate mass flow rate predictions, a modified kinetic energy carry-over coefficient model considers the effect of pressure ratio PR as

$$\mu_{1i} = \left(\frac{NT}{(1-\lambda)NT + \lambda} \right)^{\frac{1}{2}} \times f_{C_r} \times f_{PR} \tag{18}$$

with

$$\lambda = 1 - \left(1 + 16.6\, C_r / L_i\right)^{-2} \tag{6}$$

and f_{Cr} and f_{PR} obtained from a curve fitting process

$$f_{C_r} = \left(0.1528 \times \frac{C_r/R}{0.00272} + 0.8542 \right) \tag{19}$$

$$f_{PR} = \left(0.0833PR^2 + 0.025PR + 1.087\right) \tag{20}$$

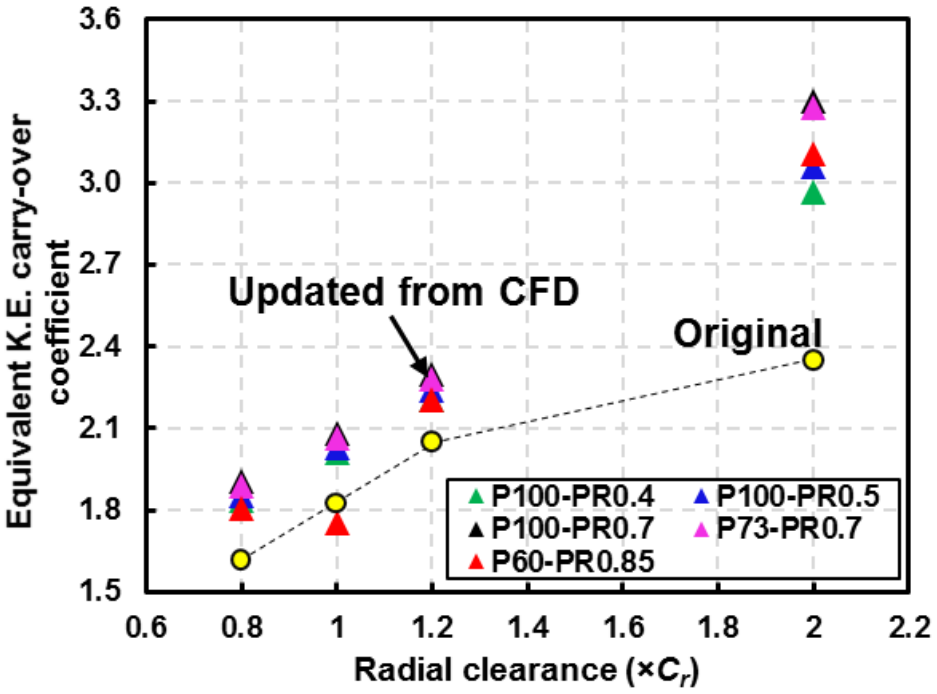

(a) μ_{1i} vs clearance

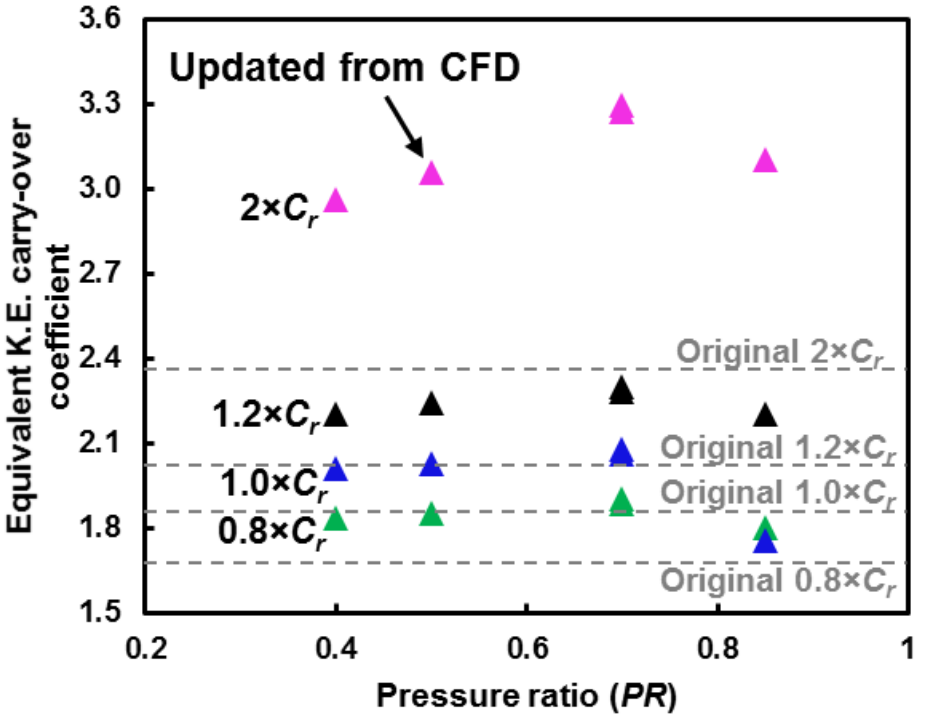

(b) μ_{1i} vs pressure ratio *PR*

Figure 40. CFD derived (averaged) μ_{1i} (a) vs. seal radial clearance; and (b) vs. pressure ratio, *PR*. TOS labyrinth seal with radial clearance = (0.8,1.0,1.2, 2.0)×C_r, supply pressure P_{in} from 60 bar to 100 bar, and pressure ratio *PR* = 0.4 ~ 0.85. Rotor speed Ω = 12 krpm ($R\Omega$ = 138 m/s).

Table 11 lists the mass flow rates predicted by a BFM with the above modified kinetic energy carry-over coefficient model. Figure 41 depicts the CFD and updated BFM predicted mass flow rate and flow factor (ϕ) versus pressure ratio. When compared to the original BFM predictions, the modified model aids to a significant improvement in the mass flow rate predictions, all within 5.4% of the CFD predictions.

Figure 42 shows the updated BFM modified flow factor $\bar{\Phi}$ agrees well with the CFD predictions. Also, the modified model produces an improved accuracy on the prediction of cavity pressures, as shown in Figure 43.

Table 11. Mass flow rate for TOS labyrinth seals: CFD and updated BFM with modified μ_{1i}. Seal radial clearance = (0.8, 1.0, 1.2, 2.0) ×C_r, supply pressure P_{in} = 60 to 100 bar, pressure ratio $PR = P_{out}/P_{in}$ = 0.4 ~ 0.85, and rotor speed Ω = 12 krpm ($R\Omega$ = 138 m/s).

Operating Conditions	Prediction Method	Mass Flow Rate [kg/s]			
		0.8 × Cr	1.0 × Cr	1.2 × Cr	2.0 × Cr
P_{in} =60 bar, PR = 0.85	CFD	0.495	0.606	0.865	1.868
	Modified	0.497	0.609	0.869	1.767
	Diff.	**0.5%**	**0.4%**	**0.5%**	**-5.4%**
P_{in} =72.8 bar, PR = 0.7	CFD	0.835	1.123	1.446	3.081
	Modified	0.839	1.129	1.457	3.083
	Diff.	**0.5%**	**0.5%**	**0.8%**	**0.1%**
P_{in} =100 bar, PR = 0.4	CFD	1.465	1.960	2.525	5.181
	Modified	1.467	1.967	2.532	5.190
	Diff.	**0.1%**	**0.4%**	**0.3%**	**0.2%**
P_{in} =100 bar, PR = 0.5	CFD	1.387	1.859	2.397	4.964
	Modified	1.391	1.868	2.413	4.975
	Diff.	**0.3%**	**0.5%**	**0.7%**	**0.2%**
P_{in} =100 bar, PR = 0.7	CFD	1.153	1.550	2.000	4.246
	Modified	1.163	1.561	2.013	4.252
	Diff.	**0.8%**	**0.7%**	**0.7%**	**0.1%**

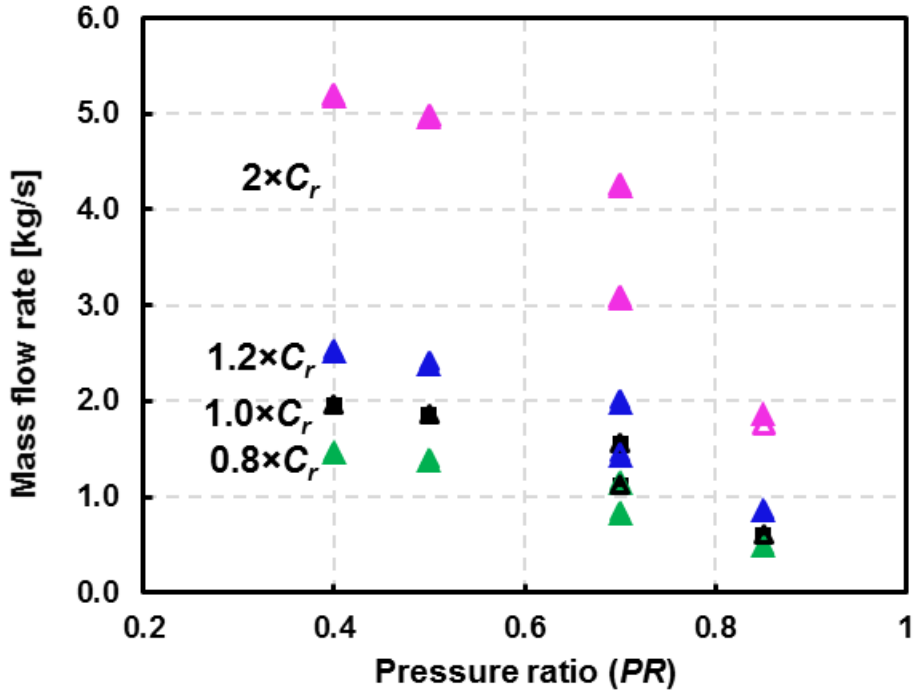

(a) mass flow rate

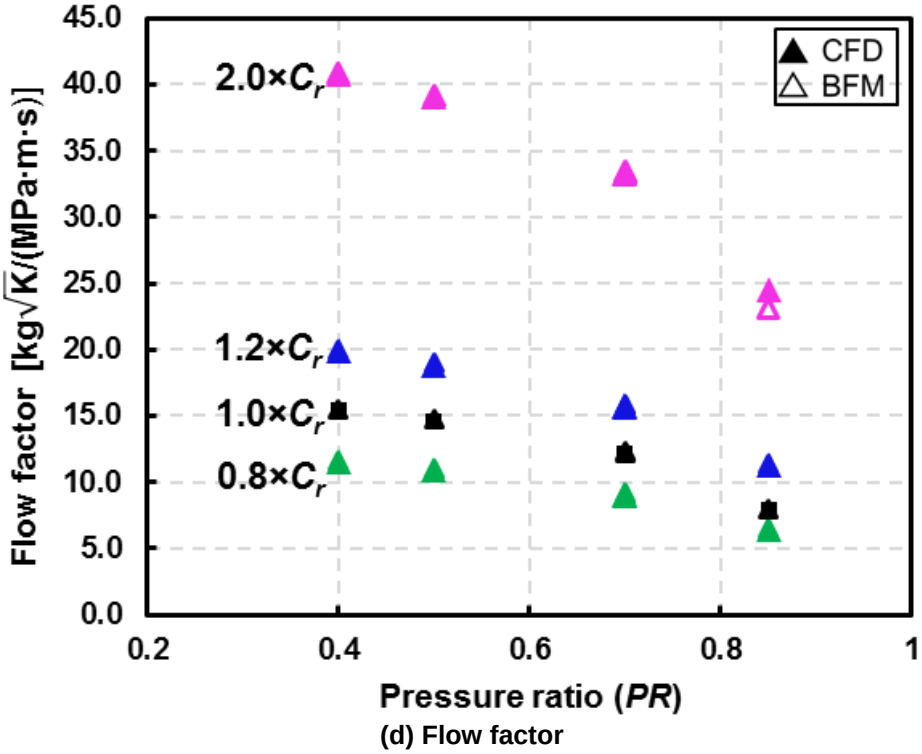

(d) Flow factor

Figure 41. CFD and updated BFM predicted (a) mass flow rate vs. *PR*; (b) flow factor vs. *PR*. TOS labyrinth seal, radial clearance = (0.8, 1.0, 1.2, 2.0) ×C_r, supply pressure increases from 60 to 100 bar, pressure ratio $PR = P_{out}/P_{in}$ = 0.4 ~ 0.85, and rotor speed Ω = 12 krpm ($R\Omega$ = 138 m/s).

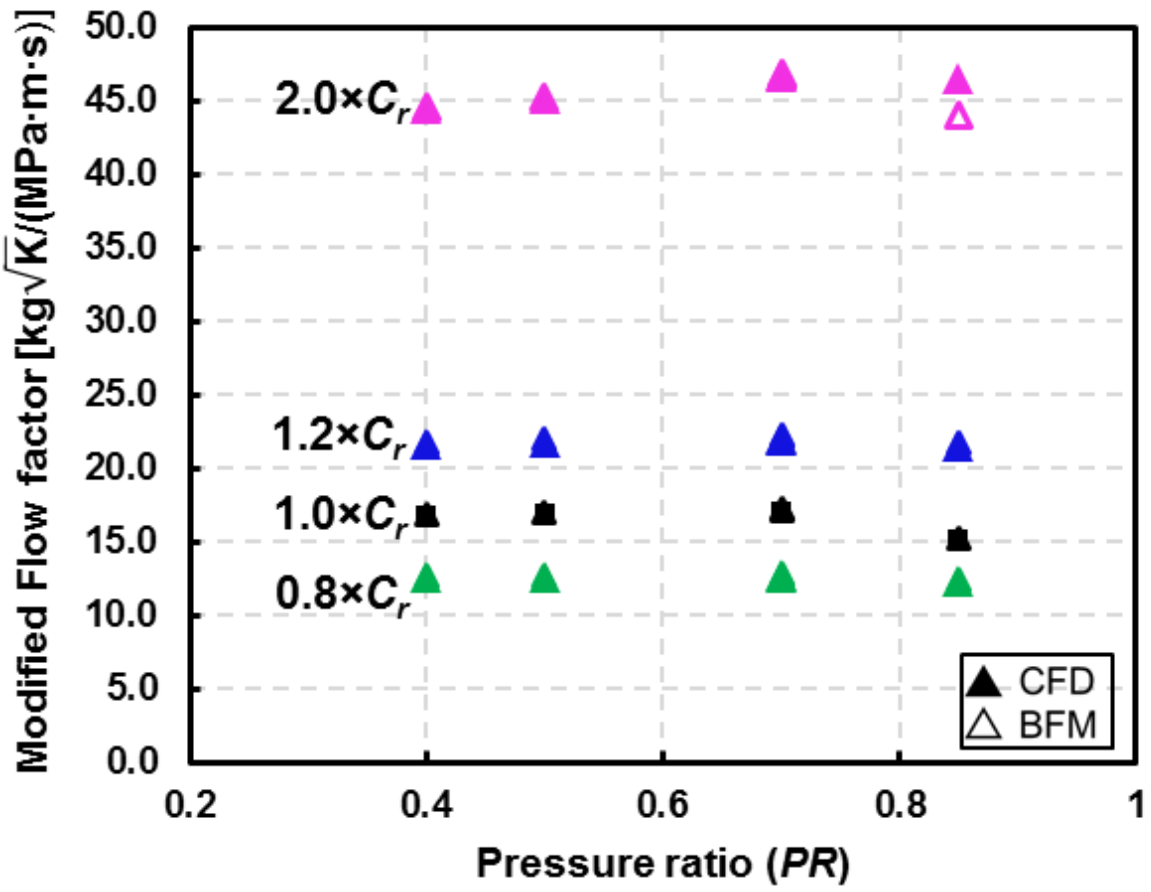

Figure 42. Modified flow factor $\bar{\Phi}$ vs. $PR = P_{out}/P_{in}$ from CFD and updated BFM. TOS labyrinth seal, radial clearance = (0.8, 1.0, 1.2, 2.0) ×C_r, supply pressure increases from 60 to 100 bar, and rotor speed Ω = 12 krpm ($R\Omega$ = 138 m/s).

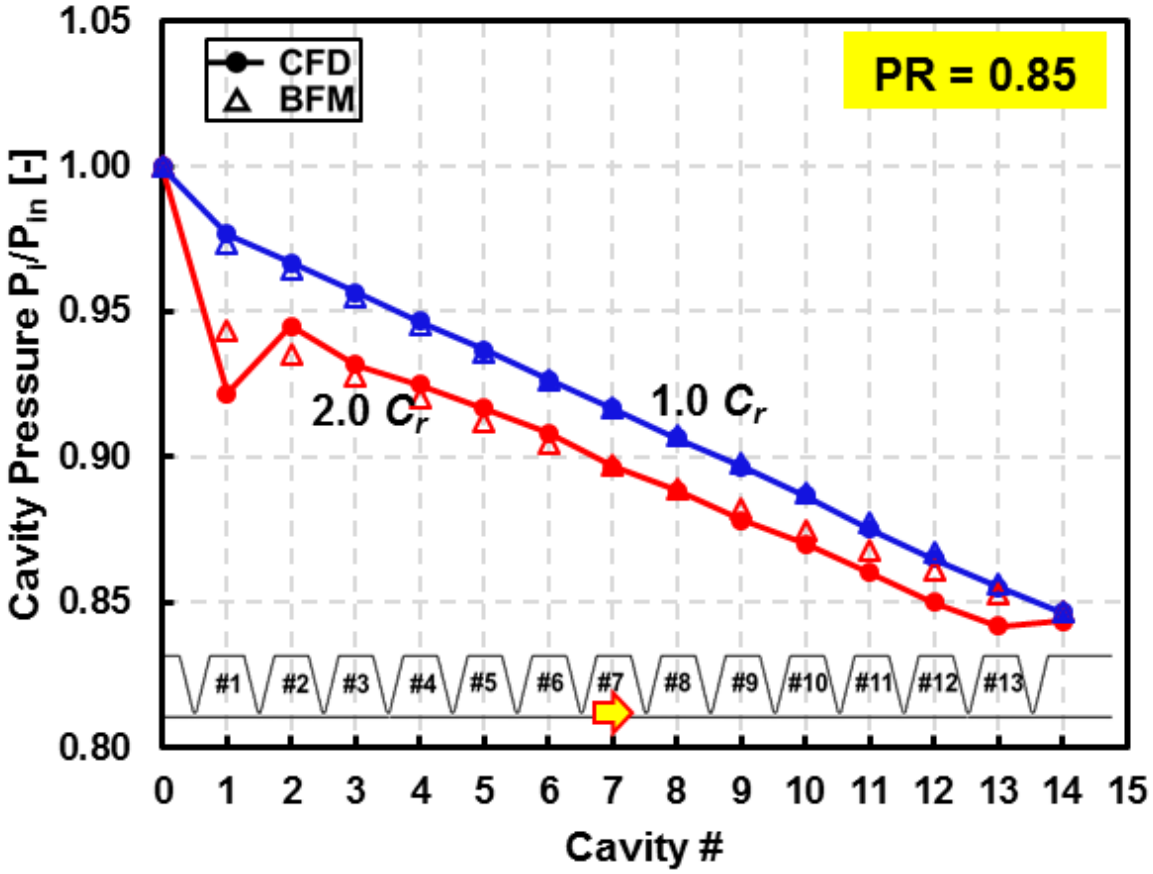

Figure 43. CFD and updated BFM predicted cavity pressure (P_i/P_{in}) vs. cavity #. TOS labyrinth seals with radial clearance = 1.0×C_r and 2.0 ×C_r, rotor speed Ω = 12 krpm, supply pressure P_{in} = 60 bar, pressure ratio PR = 0.85.

VII. AN INDEPENDENT CASE FOR VALIDATION

A 14 teeth TOS labyrinth seal tested by Ertas et al. (2012) [61]with a 0.3 mm clearance serves to further validate the updated BFM. In addition, later Li et al. [62] change the clearance of the LS to 0.1 mm and 0.2 mm to predict changes in mass flow rate. The predictions provide more data to validate the modified seal leakage model. Table 12 lists the TOS LS geometry as well as the operating conditions, Ref. [62]. Note the tooth pitch length L_i = 5 mm. Air enters the seal at a supply pressure P_{in} = 6.9 bar (absolute) and room temperature (300 K), and with a pre-swirl velocity $U_0 = 0.5R\Omega$. The seal outlet discharge pressure is P_{out} = 3.0 bar ($PR = P_{out}/P_{in}$ = 0.43).

Figure 44 depicts the mass flow rate versus seal radial clearance C_r. For the smallest clearance C_r = 0.1 mm configuration, the original BFM predicted mass flow rate agrees with the CFD prediction; however, as C_r increases, the discrepancy between the original BFM prediction and the CFD/test results increases from 7% to 14%. The updated BFM with a modified kinetic energy parameter delivers mass flow rates in agreement with the test result (C_r = 0.3 mm) and also with the CFD predicted ones for clearances C_r = 0.1 mm and 0.2 mm; and the rotor and stator surface Reynolds numbers at the seal exit plane are $Re_{r\theta} \sim 1.06\times10^5$ and $Re_{s\theta} \sim 1.5\times10^4$, respectively.

Figure 45 depicts the rotordynamic force coefficients both predicted by CFD and BFM (original and modified) and measured through test versus the excitation frequency. For C_r = 0.2 mm, the original BFM substantially over-predicts the magnitude of the direct stiffness coefficient K_{XX}; whereas the modified BFM shows a significant improvement in the direct stiffness prediction and agrees well with the CFD predictions in Ref.[62]. On the other hand, both the original and the modified BFM predicted cross-coupled stiffness coefficient (K_{XY}) show good agreement with the CFD predictions. The modified BFM under estimates the direct damping coefficients C_{XX} by 25% when compared to the CFD predictions, but shows a marked improvement when compared to the

one delivered by the original BFM, which over predicts by ~75%. The modified BFM predicted an effective damping $C_{eff} = C_{XX}/(K_{XY} \times \omega)$ shows a better agreement, within 25%, with the CFD derived results.

Similarly, for C_r = 0.3 mm, the modified BFM improves the prediction accuracy in K_{XX}. Both the original and modified BFM show acceptable accuracy in K_{XY} predictions. The modified BFM under estimates C_{XX} by as much as 50% when compared to the test measurements and CFD predictions. On the other hand, when compared to the test results, the original BFM over predicts C_{eff} by ~ 90%, whereas the modified BFM predicted C_{eff} shows a better accuracy, within 50% of the test results.

Recall the Reynolds number ranges ($Re_{r\theta} = 8.2\times10^5 \sim 3.2\times10^6$, $Re_{s\theta} = 7.2\times10^4 \sim 1.1\times10^6$) for the validity of the above friction factor coefficients models. The discrepancy between the CFD derived and the new model predicted friction factor coefficients becomes larger when the Reynolds numbers ($Re_{r\theta}$ and $Re_{s\theta}$) approach the low boundary, see Figures 25 and 27. Note the Reynolds numbers for the seals analyzed (C_r = 0.2 mm and 0.3 mm) are $Re_{r\theta} \sim 1.06\times10^5$ and $Re_{s\theta} \sim 1.5\times10^4$, which are lower than the above friction factor model validity Reynolds number range. Thus, a higher discrepancy with the CFD/test results is expected.

Table 12. Dimensions and operating conditions of a teeth-on-stator (TOS) labyrinth seal in Ref. [62].

Seal Geometry	Seal length, L	65 mm
	Rotor diameter, D	170 mm
	Radial clearance, C_r	0.1 mm, 0.2 mm, 0.3 mm (test in Ref [61])
	Teeth number, NT	14
	Tooth pitch, L_i	5 mm
	Height, B	4 mm
	Width at tip, b_t	0.3 mm
Air Properties (ideal gas)	Density, ρ @1bar	1.28 kg/m^3
	Temperature, T	300 K
	Sound speed, V_s	314 m/s
	Viscosity, ν	1.51×10^{-5} m^2/s
Operating Conditions	Supply pressure, P_{in}	6.9 bar
	Discharge pressure, P_{out}	3.0 bar
	Pressure ratio, $PR = P_{out}/P_{in}$	0.43
	Pre-swirl velocity, U_0	$0.5R\Omega$
	Rotor Speed, Ω ($R\Omega$)	15 krpm (133 m/s)

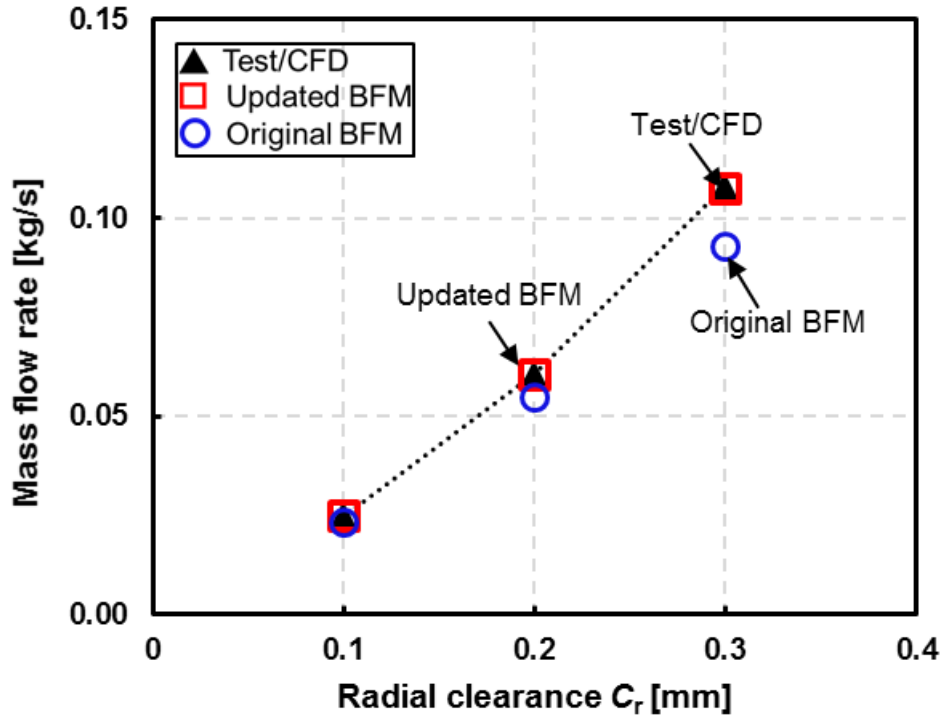

Figure 44. Measured/CFD and BFM (original and updated) predicted mass flow rate vs. radial clearance. TOS labyrinth seal [61, 62]: rotor speed Ω = 15 krpm ($R\Omega$=133 m/s), supply pressure P_{in} = 6.9 bar, pressure ratio PR = 0.43.

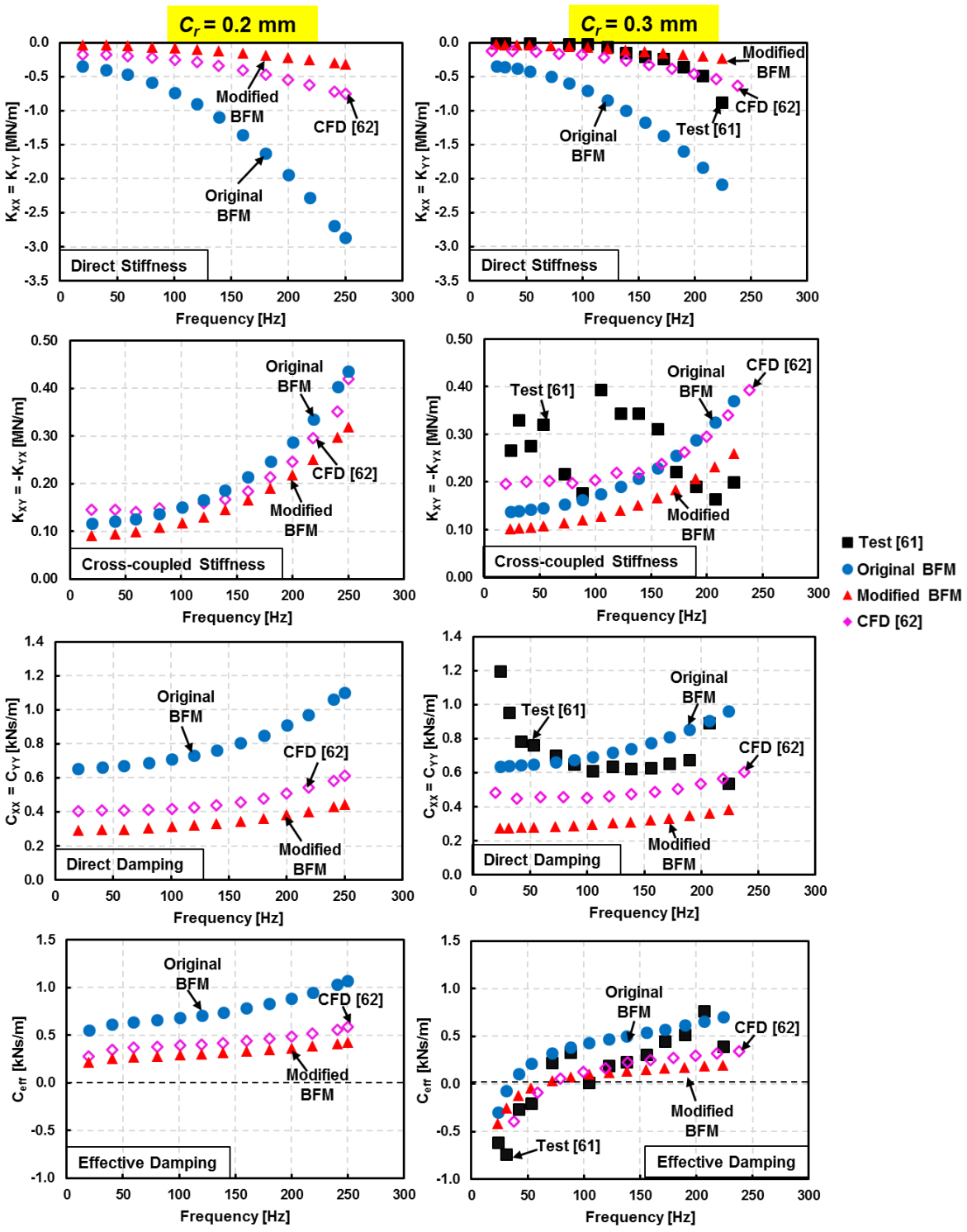

Figure 45. CFD and BFM (original and modified) predicted, and test rotordynamic force coefficients (K_{XX} , K_{XY}, C_{XX}, C_{eff}) vs. excitation frequency. TOS labyrinth seal [61, 62]: C_r = 0.2 (left), 0.3 mm (right), rotor speed Ω = 15 krpm ($R\Omega$=133 m/s), supply pressure P_{in} = 6.9 bar, pressure ratio PR = 0.43.

VIII. CONCLUSION

Widely used in gas process turbomachines, labyrinth seals control the leakage from a high-pressure region to a low-pressure region and affect the rotor-bearing system stability. The ability to accurately predict labyrinth seal performance is critical to the turbomachine industry. The dissertation delivers quantitative and qualitative assessments of the wall friction factors and kinetic energy carry-over coefficient of a typical labyrinth seal as a function of the seal geometry and operating conditions.

This work complements a multiple year research work on labyrinth seals published in Refs. [53, 60, 63, 64]. The dissertation presents a comprehensive CFD analysis quantifying the effects of seal radial clearance C_r, operating pressure ratio $PR = P_{out}/P_{in}$, rotor speed Ω, and the inlet pre-swirl ratio α on the walls (rotor and stator) friction factor and the kinetic energy carry-over coefficient in Neumann's equations for leakage. The CFD derived friction factors and kinetic energy carry-over coefficient lead to an updated friction factor model as well as a modified equation to estimate the labyrinth seal leakage.

Obtained for a single seal example, the major conclusions drawn from this work are:

(i) <u>For the friction factors on the rotor surface ($f_{r\theta}$) and the stator surface ($f_{s\theta}$)</u>

a. Effect of seal radial clearance C_r:

   Varying the seal radial clearance C_r by -20% ~ +100%, the rotor surface friction factor ($f_{r\theta}$) remains constant. On the other hand, the stator surface friction factor ($f_{s\theta}$) linearly increases with an increase in C_r.

b. Effect of rotor speed Ω:

An increase in rotor speed (Ω) promotes both the wall shear stresses ($\tau_{r\theta}$, $\tau_{s\theta}$) and the fluid tangential velocity U, decreases both $f_{r\theta}$ and $f_{s\theta}$ ($f_{r\theta} = 2\tau_{r\theta} / [\rho(U - R\Omega)^2]$, $f_{s\theta} = 2\tau_{s\theta} / [\rho U^2]$).

c. Effect of pressure ratio $PR = P_{out}/P_{in}$:

The pressure ratio ($PR = P_{out}/P_{in}$) varies from 0.4 to 0.9, a function of supply pressure P_{in} and discharge pressure P_{out}. CFD predictions show that $f_{r\theta}$ and $f_{s\theta}$ are only sensitive to the pressure ratio PR, but not to the magnitude of the supply pressure or discharge pressure; both $f_{r\theta}$ and $f_{s\theta}$ decrease with an increase in PR.

d. Effect of pre-swirl ratio $\alpha = U_0/(R\Omega)$:

When the pre-swirl ratio α varies from 0 to 0.72, $f_{r\theta}$ shows negligible changes; while $f_{s\theta}$ decreases with respect to an increase in α.

Through the above analysis, the original Blasius friction factor model is modified for the rotor and the stator surfaces to show a better accuracy compared to the CFD derived results: $f_{r\theta} = (-11.87 \times PR + 18.36)\,\mathrm{Re}_{r\theta}^{-0.54}$ and $f_{s\theta} = (-24.6 \times PR + 30.7)\,\mathrm{Re}_{s\theta}^{-0.57}$; and the modified BFM does show an improved accuracy in the rotordynamic force coefficients prediction, which agree well with both CFD and experimental results.

(ii) <u>For the kinetic energy carry-over coefficient μ_{1i}</u>

a. Effect of seal radial clearance C_r:

Varying the radial clearance by -20% ~ +100%, the μ_{1i} increases linearly with respect to C_r, $\mu_{1i} \sim \left(0.1528 \times \frac{C_r/R}{0.00272} + 0.8542 \right)$.

b. Effect of pressure ratio *PR*:

The μ_{1i} shows a non-linear correlation with the pressure ratio *PR*, $\mu_{1i} \sim \left(0.0833PR^2 + 0.025PR + 1.087 \right)$.

Furthermore, this work quantifies CFD derived correlations for the wall friction factors (f_r and f_s) and the kinetic energy carry-over coefficient (μ_{1i}) versus the seal clearance (C_r), operating conditions: rotor speed (Ω), supply pressure (P_{in}), pressure ratio (*PR*), pre-swirl velocity ratio (α). Integration of the modified models for friction factors (stator and rotor) and kinetic energy carry-over coefficient into a BFM code ultimately assists to deliver more accurate predictions for the evolution of the seal leakage, circumferential flow velocity, and the seal rotordynamic force coefficients.

A teeth-on-stator labyrinth seal (TOS LS) tested by Ertas et al. (2012) serves to validate with modest success the new leakage model as well as the modified friction factor model. Compared to both the test results and the CFD predictions, the modified BFM shows an improved accuracy in the prediction for both rotordynamic force coefficients and mass flow rate. When compared to the CFD/test results, the modified BFM decreases, with respect to the original BFM, the maximum discrepancy in mass flow rate from 14% to 2%, direct stiffness coefficient from 320% to 70%, and direct damping coefficient from 90% to 50%.

In this work, the considered seal geometry and operating conditions only generate a specific range of Reynolds number, where $Re_{r\theta} = 8.2\times10^5 \sim 3.2\times10^6$ and $Re_{s\theta} = 7.2\times10^4 \sim 1.1\times10^6$.

Therefore, the validity range of the modified friction factor coefficients models is limited. Future work considering a broader range of Reynolds numbers is recommended to extend the validity of the modified friction factor models.

NOMENCLATURE

a_r, a_s	Dimensionless length defined in Eqn. (3).
A	Cross-sectional area of the cavity [m^2]
b_t	Tooth width [mm]
B	Height of the labyrinth seal strip [mm]
C_r	Radial clearance [mm]
D	Rotor diameter [mm]
D_h	Hydraulic diameter, $D_{hi} = 2(C_r + B)L_i/(C_r + B + L_i)$ [mm]
f	Friction factor, $f_{r,s} = n_{r,s}Re^{m_{r,s}}$
h	Local radial clearance [mm]
L	Seal length [mm]
L_i	Pitch length [mm]
L_t	Tooth width [mm]
n_r, m_r, n_s, m_s	Empirical coefficients for *Blasius* friction factor
NT	Number of tooth
P_i	i^{th} cavity pressure [Pa]
P_{in}, P_{out}	Supply/discharge pressure [Pa]
PR	Pressure ratio, $PR = P_{in}/P_{out}$
Re	Reynolds number, $Re_{r,s} = U_{r,s}D_h/v$
R_g	Gas constant
R	Rotor radius [mm]
T	Temperature [K]

U	Bulk-flow circumferential velocity in a cavity [m/s]
$U_{r,s}$	Relative bulk-flow velocity, $U_r = \sqrt{W^2 + (U - R\Omega)^2}, U_s = \sqrt{W^2 + U^2}$
U_{rotor}	Rotor surface velocity $U_{rotor} = R\Omega$ [m/s]
U_0	Inlet pre-swirl velocity [m/s]
V_s	Sound speed [m/s]
W	Bulk-flow axial velocity [m/s]
Z_g	Compressibility factor
α	Inlet pre-swirl ratio, $\alpha = U_0/(R\Omega)$
γ	Specific heats ratio
Θ	Circumferential direction
μ_{1i}	Kinetic energy carry-over coefficient
μ_{2i}	Flow discharge coefficient
v	Kinematic viscosity $v = \mu/\rho$ [m^2/s]
ρ	Density [kg/m^3]
ρ_s	Density at supply pressure[kg/m^3]
τ	Shear stress [N]
Ω	Rotor speed [rpm]

Subscripts

i	i^{th} chamber value
r	Rotor surface
s	Stator surface

Abbreviations

BFM	Bulk-flow model
CFD	Computational fluid dynamics
LS	Labyrinth seal
TOS	Tooth on stator labyrinth seal

REFERENCES

[1] Elrod, D. A., Pelletti, J. M., and Childs, D. W., 1995, "Theory versus Experiment for the Rotordynamic Coefficients of an Interlocking Labyrinth Gas Seal," Turbo Expo. 1995, ASME Paper 95-GT-432.

[2] Childs, D. W., Elrod, D. A., and Hale, K., 1988, "Rotordynamic Coefficient and Leakage Test Results for Interlock and Tooth-on-Stator Labyrinth Seals," ASME Paper 88-GT-87.

[3] Zhang, H., Jia, X., Pan, X., Jiang, B., and Zheng, Q., 2016, "Interaction Between Rotor and Annular Seals: Interlaced and Straight-Through Labyrinth Seals," J. Propul. Power, **32**(6), pp. 1483-1493.

[4] Gamal, A. J., and Vance, J. M., 2008, "Labyrinth Seal Leakage Tests: Tooth Profile, Tooth Thickness, and Eccentricity Effects," ASME J Eng Gas Turb Power, **130**(1), pp. 01251001-01251011.

[5] Childs, D. W., 1993, *Turbomachinery Rotordynamics: Phenomena, Modeling, and Analysis*, Chap.5, "Rotordynamic Models for Annular Gas Seals", John Wiley & Sons, pp. 209-306.

[6] Hirs, G. G., 1973, "A Bulk-Flow Theory for Turbulence in Lubricant Films," ASME J Lubric Tech, **95**(2), pp. 137-145.

[7] San Andrés, L., 2009, "Turbulence Flow in Thin Film Bearings: Characteristics and Modeling", Lecture Notes No.08, Open source: http://rotorlab.tamu.edu/me626."

[8] Yamada, Y., 1962, "Resistance of a Flow through an Annulus with an Inner Rotating Cylinder," Bulletin of JSME, **5**(18), pp. 302-310.

[9] Childs, D., and Ha, T., 1992, "Friction Factor Data for Flat-Plate Tests of Smooth and Honeycomb Surfaces," ASME J. Tribol, **114**(4), pp. 722-730.

[10] Al-Qutub, A. M., Elrod, D., and Coleman, H. W., 2000, "A New Friction Factor Model and Entrance Loss Coefficient for Honeycomb Annular Gas Seals," ASME J. Tribol, **122**(3), pp. 622-627.

[11] Benckert, H., and Wachter, J., 1978, "Studies on Vibrations Stimulated by Lateral Forces in Sealing Gaps," AGARD Seal Technology in Gas Turbine Engineering, UK.

[12] Leong, Y., and Brown, R., 1984, "Experimental Investigation of Lateral Forces Induced by Flow through Model Labyrinth Glands," Proceedings of a Workshop on Rotordynamic Instability Problems in High-Performance Turbomachinery,Texas A&M University, College Station, TX, pp. 187-210.

[13] Childs, D. W., and Scharrer, J. K., 1986, "Experimental Rotordynamic Coefficient Results for Teeth-on-Rotor and Teeth-on-Stator Labyrinth Gas Seals," ASME J Eng Gas Turb Power, **108**(4), pp. 599-604.

[14] Thieleke, G., and Stetter, H., 1990, "Experimental Investigations of Exciting Forces Caused by Flow in Labyrinth Seals," Proceeding of a Workshop on Rotordynamic Instability Problems in High-Performance Turbomachinery,Texas A&M University, College Station, TX, pp. 109-134.

[15] Paolillo, R., Moore, S., Cloud, D., and Glahn, J. A., 2007, "Impact of Rotational Speed on the Discharge Characteristic of Stepped Labyrinth Seals," Turbo Expo. 2007, ASME Paper GT2007-28248.

[16] Li, Z., Li, J., Yan, X., and Feng, Z., 2011, "Effects of Pressure Ratio and Rotational Speed on Leakage Flow and Cavity Pressure in the Staggered Labyrinth Seal," ASME J Eng Gas Turb Power, **133**(11), pp. 11450301-11450306.

[17] Hodkinson, B., 1939, "Estimation of The Leakage through a Labyrinth Gland," Proceedings of the Institution of Mechanical Engineers, **141**(1), pp. 283-288.

[18] Zhang, L., Zhu, H., Liu, C., and Tong, F., "Experimental and Numerical Investigation on Leakage Characteristic of Stepped Labyrinth Seal," Proc. Turbo Expo. 2016, ASME Paper GT2016-56743.

[19] Picardo, A., and Childs, D. W., 2005, "Rotordynamic Coefficients for a Tooth-on-Stator Labyrinth Seal at 70 Bar Supply Pressures: Measurements versus Theory and Comparisons to a Hole-Pattern Stator Seal," ASME J Eng Gas Turb Power, **127**(4), pp. 843-855.

[20] Wagner, N. G., Steff, K., Gausmann, R., and Schmidt, M., 2009, "Investigations on the Dynamic Coefficients of Impeller Eye Labyrinth Seals," Proc. of the 38th Turbomachinery Symposium, Houston, TX, September 14-17.

[21] Ertas, B. H., Delgado, A., and Vannini, G., 2012, "Rotordynamic Force Coefficients for Three Types of Annular Gas Seals with Inlet Preswirl and High Differential Pressure Ratio," ASME J Eng Gas Turb Power, **134**(4), pp. 042503-042512.

[22] Vannini, G., Cioncolini, S., Del Vescovo, G., & Rovini, M. , 2014, "Labyrinth Seal and Pocket Damper Seal High Pressure Rotordynamic Test Data," ASME J Eng Gas Turb Power, **136**(2), pp. 022501-022509.

[23] Murphy, B., and Vance, J., 1980, "Labyrinth Seal Effects on Rotor Whirl Instability," Proceedings of the 2nd International Conference on Vibrations in Rotating Machinery,Cambridge, England, September 1-4.

[24] Kostynk, A., 1972, "Theoretical Analysis of the Aerodynamic Forces in the Labyrinth Glands of Turbomaehines," Therm Eng, **19**(11), pp. 29-33.

[25] Iwatsubo, T., 1980, "Evaluation of Instability Forces of Labyrinth Seals in Turbines or Compressors," Proceedings of a Workshop on Rotordynamic Instability Problems in High-Performance Turbomachinery,Texas A&M University, College Station, TX, pp. 139-167.

[26] Iwatsubo, T., Motooka, N., and Kawai, R., 1982, "Flow Induced Force of Labyrinth Seal," Proceedings of a Workshop on Rotordynamic Instability Problems in High-Performance Turbomachinery,Texas A&M University, College Station, TX, pp. 205-222.

[27] Childs, D. W., and Scharrer, J. K., 1986, "An Iwatsubo-Based Solution for Labyrinth Seals: Comparison to Experimental Results," ASME J Eng Gas Turb Power, **108**(2), pp. 325-331.

[28] Martin, H., 1908, "Labyrinth Packings," Engineering, **85**(10), pp. 35-38.

[29] Egli, A., 1935, "The Leakage of Steam through Labyrinth Seals," Trans. Asme, **57**(3), pp. 115-122.

[30] Neumann, K., 1964, "Zur Frage der Verwendung von Durchblickdichtungen im Dampfturbinenbau," Maschinenbautechnik, **13**(4), pp. 188-195.

[31] Villasmil Urdaneta, L., 2002, "Understanding The Friction Factor Behavior in Liquid Annular Seals with Deliberately Roughened Surfaces, A CFD Approach," M.S Thesis, Texas A&M University, College Station, USA.

[32] Villasmil Urdaneta, L., 2006, "Parameters Defining Flow Resistance and The Friction Factor Behavior in Liquid Annular Seals With Deliberately Roughened Surfaces," Ph.D Thesis, Texas A&M University, College Station, USA.

[33] D'Souza, R., and Childs, D. W., 2002, "A Comparison of Rotordynamic-Coefficient Predictions for Annular Honeycomb Gas Seals Using Three Different Friction-Factor Models," ASME J. Tribol, **124**(3), pp. 524-529.

[34] Moore, J. J., 2003, "Three-Dimensional CFD Rotordynamic Analysis of Gas Labyrinth Seals," ASME J Vib Acoust, **125**(4), pp. 427-433.

[35] Kwanka, K., 2001, Der Einfluss von Labyrithdichtungen auf die Dynamik von Turbomaschinen, Fortschritt-Bericht VDI-Verlag.

[36] Wagner, N. G., 1999, "Reliable Rotor Dynamic Design of High-Pressure Compressors Based on Test Rig Data," ASME Paper 99-GT-150.

[37] Schettel, J., Deckner, M., Kwanka, K., Lüneburg, B., and Nordmann, R., 2005, "Rotordynamic Coefficients of Labseals for Turbines: Comparing CFD Results With Experimental Data on a Comb-Grooved Labyrinth," Turbo Expo. 2005, ASME Paper GT2005-68732.

[38] Kim, T. S., and Cha, K. S., 2009, "Comparative Analysis of The Influence of Labyrinth Seal Configuration on Leakage Behavior," J Mech Sci Technol, **23**(10), pp. 2830-2838.

[39] Kim, T. S., and Kang, S. Y., 2010, "Investigation of Leakage Characteristics of Straight and Stepped Labyrinth Seals," International Journal of Fluid Machinery and Systems, **3**(3), pp. 253-259.

[40] Kang, Y., Kim, T. S., Kang, S. Y., and Moon, H. K., 2010, "Aerodynamic Performance of Stepped Labyrinth Seals for Gas Turbine Applications," Turbo Expo. 2010, ASME Paper GT2010-23256.

[41] Pugachev, A. O., and Deckner, M., 2010, "Analysis of the Experimental and CFD-Based Theoretical Methods for Studying Rotordynamic Characteristics of Labyrinth Gas Seals," Turbo Expo. 2010, ASME Paper GT2010-22058.

[42] Pugachev, A. O., Kleinhans, U., and Gaszner, M., 2012, "Prediction of Rotordynamic Coefficients for Short Labyrinth Gas Seals Using Computational Fluid Dynamics," ASME J Eng Gas Turb Power, **134**(6), pp. 06250101-06250110.

[43] Pugachev, A. O., and Degen, H., 2012, "CFD-Predicted Rotordynamic Coefficients for a 20-Teeth-on-Stator Labyrinth Seal at High Supply Pressure Conditions," Turbo Expo. 2012, ASME Paper GT2012-68381.

[44] Gao, R., and Kirk, G., 2013, "CFD Study on Stepped and Drum Balance Labyrinth Seal," Tribol T, **56**(4), pp. 663-671.

[45] Dai, Y., Tyacke, J., and Tucker, P., 2016, "Effect of Labyrinth Seal Configurations on Leakage Performance using LES," 54th AIAA Aerospace Sciences Meeting, San Diego, California, USA.

[46] Rai, A. C., Prabhudharwadkar, D., Murthy, S., Giametta, A., and Johns, D., 2016, "Effect of Air-Curtains on Labyrinth Seal Performance," Turbo Expo. 2016, ASME Paper GT2016-57188.

[47] Migliorini, P. J., Untaroiu, A., Wood, H. G., and Allaire, P. E., 2012, "A Computational Fluid Dynamics/Bulk-Flow Hybrid Method for Determining Rotordynamic Coefficients of Annular Gas Seals," ASME J Tribol, **134**(2), pp. 0222021-0222029.

[48] Migliorini, P. J., Untaroiu, A., Witt, W. C., Morgan, N. R., and Wood, H. G., 2014, "Hybrid Analysis of Gas Annular Seals with Energy Equation," ASME J Tribol, **136**(3), pp. 0317041-0317049.

[49] Childs, D. W., and Wade, J., 2004, "Rotordynamic Coefficient and Leakage Characteristics for Hole-Pattern-Stator Annular Gas Seals-Measurements versus Predictions," ASME J Tribol, **126**(2), pp. 326-333.

[50] San Andrés, L., Wu, T., Maeda, H., and Ono, T., 2018, "A Computational Fluid Dynamics Modified Bulk-Flow Analysis for Circumferentially Shallow Grooved Liquid Seals," ASME J Eng Gas Turb Power, **140**, pp. 0125041- 0125049.

[51] Nordmann, R., Dietzen, F. J., Janson, W., Frei, A., Florjancic, S., 1986, "Rotordynamic Coefficients and Leakage Flow of Parallel Grooved Seals and Smooth Seals,"Texas A&M University, College Station, TX, NASA Assession No. 87N22206, pp. 129-153. URL https://ntrs.nasa.gov/search.jsp?R=19870012773.

[52] Cangioli, F., Vannini, G., Pennacchi, P., Ciuchicchi, L., Nettis, L., and Chatterton, S., 2018, "Rotordynamic Characterization of a Staggered Labyrinth Seal: Experimental Test Data and Comparison with Predictions," ASME J Eng Gas Turb Power, **141**(1), pp. 01100901-01100912.

[53] Wu, T., and San Andrés, L., 2019, "Gas Labyrinth Seals: on the Effect of Clearance and Operating Conditions on Wall Friction Factors – a CFD Investigation," Tribol Int, **131**, pp. 363-376.

[54] San Andrés, L., Wu, T., Barajas-Rivera, J., Zhang, J., and Kawashita, R., 2019, "Leakage and Cavity Pressures in an Interlocking Labyrinth Gas Seal: Measurements vs. Predictions," ASME paper GT2019-91507.

[55] Childs, D. W., 1993, *Turbomachinery Rotordynamics: Phenomena, Modeling, and Analysis*, Chap.4, "Rotordynamic Models for Annular Gas Seals", John Wiley & Sons.

[56] Yèucel, U., 1996, "Leakage and Swirl Velocities in Labyrinth Seals," M.S. Thesis, Department of Applied Mathematics, Lehigh University.

[57] Gurevich, M. I., 1966, *The Theory of Jets in an Ideal Fluid*, Pergamon Press, Oxford, pp. 235-256.

[58] San Andrés, L., 1991, "Analysis of Variable Fluid Properties, Turbulent Annular Seals," ASME J Tribol, **113**(4), pp. 694-702.

[59] Vannini, G., Cioncolini, S., Del Vescovo, G., and Rovini, M., 2014, "Labyrinth Seal and Pocket Damper Seal High Pressure Rotordynamic Test Data," ASME J Eng Gas Turb Power, **136**(2), pp. 022501-022509.

[60] San Andrés, L., and Wu, T., 2017, "An Improved Bulk-Flow Analysis for Interlocking Labyrinth Gas Seals: Leakage and Force Coefficients," A Technical Report to Turbomachinery Research Consortium (TRC), June 2017, Report No. TRC-Seal-02-17.

[61] Ertas, B. H., Delgado, A., and Vannini, G., 2012, "Rotordynamic Force Coefficients for Three Types of Annular Gas Seals with Inlet Preswirl and High Differential Pressure Ratio," ASME J Eng Gas Turb Power, **134**(4), pp. 04250301-04250312.

[62] Li, Z., Li, J., and Feng, Z., 2016, "Labyrinth Seal Rotordynamic Characteristics Part II: Geometrical Parameter Effects," J. Propul Power, **32**(5), pp. 1281-1291.

[63] San Andrés, L., and Wu, T., 2018, "Gas Labyrinth Seals: on the Effect of Clearance and Operating Conditions on Wall Friction Factors – a CFD Investigation," A Technical Report to Turbomachinery Research Consortium (TRC), June 2018, Report No. TRC-Seal-02-18.

[64] Wu, T., and San Andrés, L., 2018, "Leakage and Dynamic Force Coefficients for Two Labyrinth Gas Seals: Teeth-on-Stator and Interlocking Teeth Configurations. A CFD Approach to Their Performance," ASME J Eng Gas Turb Power, **141**(4), pp. 04250101-04250112.